Magnetic dynamics and spin currents
in quantum spin systems strongly coupled to environment

Dissertation

zur Erlangung des Doktorgrades der Naturwissenschaften
(Dr. rer. nat.)

der

Naturwissenschaftlichen Fakultät II
Chemie, Physik und Mathematik

der Martin-Luther-Universität
Halle-Wittenberg

vorgelegt von

Herrn Stagraczyński, Stefan Piotr
geb. am 02.08.1987 in Kolbuszowa

Contents

List of Figures

Abstract

We investigate ways of controlling the magnetic dynamic, spin currents and other materials properties in topological insulators interfaces with non-collinear magnetic structure, and also in dilute magnetic semiconductors. A fundamental analysis of the electronic structure including spin-orbit coupling is relevant for engineering interesting spin related phenomena at the interfaces. The effect of strain on magnetic anisotropy in dilute magnetic semiconductors was classified. Moreover, the magnetic dynamic of adatoms deposited on the substrate was used to moderate the electronic structure of the sublayer. An appropriate time-dependent driving mechanism was identified that allows for an improved communication protocol of the quantum state transfer. The many-body localization phase for a spin-frustrated chain was confirmed, and a new method for estimating the critical disorder for its appearance has been inferred.

Wir untersuchen verschiedene Möglichkeiten der Steuerung der magnetischen Dynamik, des Spinstroms sowie von weiteren Materialeigenschaften in Heterostrukturen von topologische Isolatoren und darauf deponierten magnetischen Atomen, sowie in verdünnte en magnetische en Halbleitern. Eine fundamentale Analyse der elektronischen Struktur einschließlich der Spin-Orbit-Kopplung ist für die Entwicklung von interessanten spinbezogenen Phänomenen an den Grenzflächen wichtig. Der Einfluß von Verzerrung auf die magnetischen Anisotropien in verdünnten magnetischen Halbleitern wurde klassifiziert. Darüber hinaus wurde die magnetische Dynamik der auf dem Substrat abgeschiedenen Adatome verwendet, um die elektro-

nische Struktur der Unterschicht zu kontrollieren. Ein zeitabhängiger Antriebsmechanismus wurde identifiziert Kommunikationsprotokoll der Quantenzustandsübertragung beinhaltet. Die Vielteilchen-Lokalisierungsphase für eine Spin-frustrierte Kette wurde bestätigt sowie eine neue Methode zum Finden der kritischen Unordungsstärke für das Auftreten der Vielteilchenlokalisierung vorgeschlagen.

Introduction

This dissertation builds on knowledge from solid state physics, material physics, and statistical physics to address aspects pertinent to the field of spintronics [1]. Spintronics and pseudospintronics [2] exploit the spin degree of freedom and its coupling to the orbital motion to store, and process information as well as to operate "spin-electronic" devices [3]. Spin-charge coupled systems are interesting for electronic applications insofar as they offer new efficient ways for handling information [4]. For instance, magnetic information can be addressed via electric fields, strain or heat currents instead of the conventional way of using magnetic fields. This entails thus less energy consumption while generating dissipative charge currents to produce the needed magnetic fields. A number of these issues are addressed theoretically in this thesis with a focus on low-dimensional systems allowing more reliable theoretical predictions but are also of interest for practical purposes in view of the current drive towards ever higher packing density of information and smaller devices [5]. A special attention is devoted to the influence of external (environmental) perturbations on the spin dynamics with an eye to possibly exploiting these perturbations for new functionalities.

This thesis addresses a few questions related possible ways of spin control and to the influence of spin-orbital coupling on the surface and bulk spin-resolved electronic structure. In this dissertation, we would like to address a few questions.

We start with the magnetic dynamics of the spin-1/2 system where we study **quantum state transfer**(QST). Transfer of a quantum state from a node of the spin chain to another [6]. Can we improve the transmission time of the QST protocol? Then we study

strongly disordered spin-1/2 systems for which all of the eigenstates violate the eigenstate thermalization hypothesis leading to **many-body localization**(MBL) phase. Is it possible to drive the spin-frustrated chain to the MBL phase? Then we study **topological insulator**(TI) which in bulk is an insulator or semiconductor but at the surface has conducting states [7]. Can the non-collinear spin structure open the band gap of the topological insulator surface states? What are the spin dynamics equations in the case of the localized spins and conductance surface states carriers? Then we study the **dilute magnetic semiconductor**(DMS) systems [8]. Those semiconductors gain magnetic properties when doped with magnetic impurities. How does a strain affect magnetic anisotropy of DMS? Then we study the Rashba component of the spin-orbit coupling [9]. Is the Rashba spin-orbit coupling powerful enough to change the spin holes polarization in the DMS thin layers?

The localized spin dynamics[10, 11] was investigated with our generalized Heisenberg model. From there we have learned that the antisymmetric terms of exchange couplings like **Dzyaloshinskii-Moriya interaction**(DMI) are important for magnetic dynamics.

The QST for the spin-1/2 ferromagnetic chain was discussed by S. Bose [6]. The multiferroic spin chain with a static external electric field was studied by M. Azimi et al. [12]. As a new improvement, a time-dependent driving mechanism inserted to the polarization term was considered. Depending on the driving mechanism it is possible to achieve faster QST protocol.

Another aspect of the spin structures examined in spin-1/2 systems was MBL [13]. The currently established method for estimating the strength of the site-dependent magnetic disorder that leads to MBL phase was studied by Luitz et al. [14]. That was related to the ferromagnetic spin chains. We analyzed the possibility of transition to the MBL phase in the spin-frustrated models also including DMI. We recommend a new method for the classification of the MBL phase in a highly disordered system.

Further, we want to have a closer look at surface states of topological insulator [7]. Due to the breaking of the time-reversal symmetry, the band gap of the surface states can be lifted [15]. We investigate the influence of the non-collinear magnetization on the surface state of the topological insulator. The surface state band gap is not opened at the Dirac point but as we observed at the edge of the Brillouin Zone. The spin density dynamics was derived

for the unperturbed Dirac Hamiltonian and for the interaction with magnetic adatoms which enter to the spin-relaxation/pumping mechanism. At last, the force induced by spin-torque form surface state charge carriers is described [16, 17].

Chapter 3 is entirely devoted to the DMS physics where the control of the spin structure with its origin from magnetic impurities is discussed [8]. The used material is of great interest for the spintronic application [4, 18, 19]. We have investigated in details the strain effect and the Rashba spin-orbit coupling on the magnetization anisotropy of the DMS top valence bands.

Structure of the dissertation   This work is structured as follows. Possibility to control spin structure is the main topic of Chapter 1, while the aspects related to the **spin-orbit coupling**(SOC) are discussed in Chapters 2 and 3. Chapter 1 begins with a generalized form of Heisenberg model which is used for magnetic dynamics of the localized spins, quantum state transfer simulation, followed by a fresh view on Many-body localization phase in a highly disordered system. In chapter 2, perturbation theory is used to Dirac point for modeling surface states of a topological insulator with magnetic adatoms which then is followed by spin density dynamics within continuity equation. At last, a computing force induced by spin-torque is described. Chapter 3 is entirely devoted to dilute magnetic semiconductors physics where the control of the spin structure with its origin from magnetic impurities and Rashba spin-orbit field is discussed. The magnetization anisotropy and Rashba spin-orbit field are of our interest as they can influence other materials which are in contact with the semiconductor.

Spin dynamics in finite size structures with localized spins coupled to the local magnetic field

In this chapter, the generalized form of Heisenberg model is introduced enabling the treatment of spin chains as well as coupled clusters or three-dimensional molecules. In this form, the Hamiltonian can be easily used to study systems with various symmetries, spatially depending exchange couplings and systems where the different type of anisotropies can be easily introduced. Thereafter, as an application of this model, the **quantum state transfer**(QST) is considered in a ferromagnetic and non-collinear spin chains. This is followed by an analysis of the electric field influence in time-dependent Hamiltonian on the quantum state transfer fidelity. At the end of this chapter, the transition to **many-body localization**(MBL) phase is investigated in highly disordered magnetic fields.

1.1 Quantum Heisenberg model

The ferromagnetic interactions of localized spins were successfully interpreted in 1929 by Werner Heisenberg [20]. In particular, the generalized Heisenberg model can be used to study ferromagnetic and anti-ferromagnetic, non-collinear or multiferroic spin systems. On the other hand, the influence of electric fields, polarization, and magnetic fields can be included giving many ways to induce spin currents, quantum state transfer, and many-body localization in highly disordered systems.

Let us first consider the quantum spin chain with the exchange interactions between the localized spins in a system with an effective magnetic field that acts on each localized spin. In this way, we are modeling the influence of environment on which the strength of the exchange interactions depends. We assume that the effective field is mostly related to the environment, but it also includes an external magnetic field. Thus, that model allows us to take into account the possibility to control the spin density by an external field. We adopted the quantum Heisenberg model to the standard form [21]

$$\mathcal{H} = \sum_{i,j,\alpha,\beta} \mathcal{J}_{ij}^{\alpha\beta} S_i^{\alpha} S_j^{\beta} + \sum_{i,\alpha} \mathcal{B}_i^{\alpha} S_i^{\alpha}, \tag{1.1}$$

where α and β are three-dimensional spin components that can be $\{x, y, z\}$ and the indices of the localized spins $i, j = 1, \ldots, N$ denote all basis set of the chain, and $\mathcal{B}_i^{\alpha}$ are components of the site-dependent magnetic field. In the following chapters, the used Hamiltonian is always written in the S^z basis. Because of that, the only $\mathcal{B}^z$ component is taken into account. The exchange coupling $\mathcal{J}_{ij}^{\alpha\beta}$ stands for isotropic and anisotropic terms, such as nearest-neighbors, next-nearest-neighbors or Dzyaloshinskii-Moriya interaction and the effect of polarization.

An explanation of the $\mathcal{J}$-coupling tensor   Let us consider an example which can be important for practical application presented in Fig. 1.1. The concept of $\mathcal{J}$-coupling tensor is associated with the geometry formed by the localized spins. Starting from the left side of the figure which presents a 1D chain with open boundary conditions and the coupling matrix for the nearest-neighbor interaction only. In a usual case, the non-zero interactions form a symmetric coupling matrix($\mathcal{J}_{ij} = \mathcal{J}_{ji}$). Thus, with an additional factor of 2, the lower or upper triangle matrix can be used instead of the full matrix. It is worth to note that the sites coordinate in coupling tensor do not reflect the coordinates of elements in real space. Thus, the chain may look as in Fig. 1.1, but for example, it may also be a chain made out of different species where not only the coupling strength can vary or as it is shown in the case of a ring or a cluster of spins.

Therefore, as it is shown the $\mathcal{J}$ tensor is unique for a given geometry of the system. It can describe all interactions between all of the sites. That could be isotropic(nearest-neighbor, next-nearest-neighbor interactions or each site with any other site) as well as anisotropic in
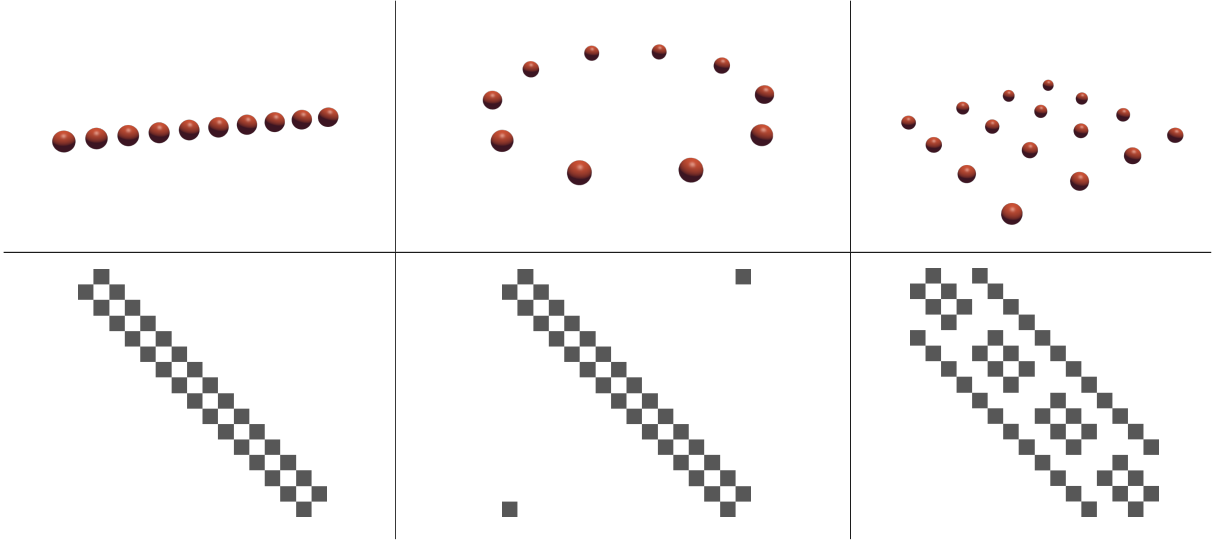
Figure 1.1: Examples of geometries for generalized Heisenberg model in a first row and the corresponding non-zero elements of $\mathcal{J}$ tensor for the nearest-neighbor coupling only(second row).

the case of DMI. Each type of those effective interactions can be understood as the influence of the environment on localized spins. The origin of the interactions can be diverse from coupling to the surrounding electrons, effective polarization, photon fields(e. g. optical lattice), phonos, etc. However, the main feature of this description is that changing properties of the environment permit to manipulate exchange interactions between localized spins.

1.2 Non-collinear magnetization

Now, we consider the case when the Hamiltonian (1.1) describes a system with no total effective magnetic moment such as a non-collinear spin structure which appears from a competition between the symmetric coupling constants $\mathcal{J}_{ij}^{\alpha\alpha}$, namely between the nearest-neighbor interactions and the next-nearest-neighbor interactions. Assuming that a linear 1D chain is considered with $\mathcal{J}_1$ and $\mathcal{J}_2$ exchange interaction for respectively the nearest-neighbor and next-nearest-neighbor coupling constants, where $\mathcal{J}_1 < 0$ denotes ferromagnetic and $\mathcal{J}_2 \geq -\mathcal{J}_1/4$ denotes antiferromagnetic coupling. The factor $1/4$ comes from minimizing the energy. Such case can be easily solved leading to the energy of the ground state depending

on the exchange constants[20]

$$\varepsilon = -4\mathcal{J}_1 S^2 \cos\theta - 4\mathcal{J}_2 S^2 \cos 2\theta, \tag{1.2}$$

where $\cos\theta = -\mathcal{J}_1/4\mathcal{J}_2$, for which the helical spin structure can exist. It should be noted, that even in this very simplified case it is a difficult task to find all of the excited states. Any additional disorder in the coupling constants or the magnetic field typically has to be treated numerically.

Dzyaloshinskii-Moriya interaction (DMI)   Weak ferromagnetism due to the Dzyaloshinskii-Moriya interaction arises by introducing a spin-orbit coupling into the Anderson theory of superexchange interaction. The Dzyaloshinskii term [22] of antisymmetric spin coupling

$$\vec{\mathcal{D}} \cdot (\vec{S}_i \times \vec{S}_j), \tag{1.3}$$

where $\vec{\mathcal{D}}\hat{e}_z = \mathcal{D}$ is a constant, was postulated phenomenologically. The typical values of DMI are of the order of $\left|\frac{\mathcal{D}}{\mathcal{J}}\right| \approx 10^{-2}$ [20]. Later, the theory was completed by Moriya, who incorporated the rules due to the crystal symmetry [23]. Let us consider two interacting localized spins, one at point A and one at point B, see Fig. 1.2. First of all, the DMI is
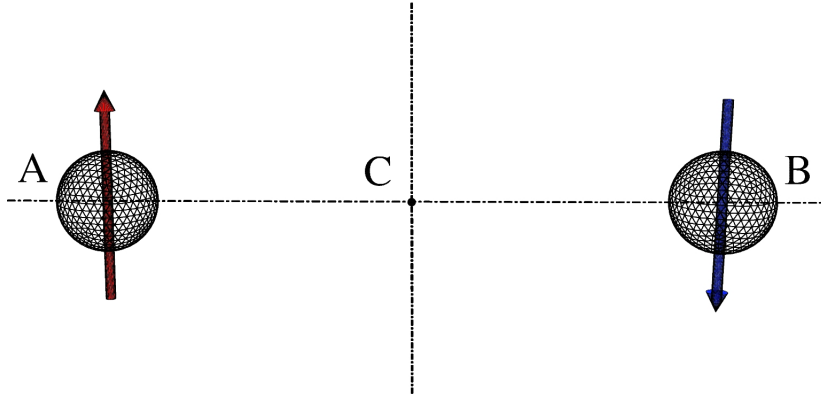
Figure 1.2: Schematic representation of two interacting localized spins.

compensated($\mathcal{D} = 0$) when a center of inversion is situated at point C. That is exactly at the center of the AB segment. Whereas when the mirror plane contains C and is perpendicular to AB segment, the DMI vector is parallel to the mirror plane or perpendicular to the AB segment($\vec{\mathcal{D}} \parallel$ mirror plane or $\vec{\mathcal{D}} \perp$ AB). When the mirror plane contains A and B, the

DMI vector is perpendicular to that plane($\vec{\mathcal{D}} \perp \text{mirror plane}$). If the system has a two-fold rotation symmetry around the axis containing the point C and is perpendicular to the AB segment, the DMI vector is perpendicular to that axis($\vec{\mathcal{D}} \perp \text{two} - \text{fold axis}$). In case of n-fold symmetry axis, where $n \geq 2$ containing AB segment, the DMI vector is parallel to this axis($\vec{\mathcal{D}} \parallel n-\text{fold axis}$). The key types of considered symmetries are a) time-reversal symmetry, b) spatial inversion. These rules aid in a conclusion that the Dzyaloshinskii-Moriya interaction exists only due to the spin-orbit coupling when the inversion symmetry is broken. The bottom line is that a breaking of the inversion symmetry of the surrounding generates a spin torque acting on the localized spins by hopping electrons between neighboring states and induces the spin current.

Spin current induced by exchange interactions in the spin chain

A possibility to temporarily generate a spin current is an important feature for quantum communication protocol. Therefore, it is of interest to enable breaking of the inversion symmetry in a reversible way. Almost half a century after Moriya, a new mechanism of the magneto-electric coupling was considered in the work of Katsura et. al.[10] wherein a system with an inversion symmetry(no DMI) the applied external electric field induces spin-current leading to steady state electric polarization

$$\vec{P} \sim \vec{e}_{i,i+1} \times \left(\vec{S}_i \times \vec{S}_{i+1} \right), \tag{1.4}$$

that is directly related to DMI, and the vector $\vec{e}_{i,i+1}$ points between two neighboring localized spins. The similar derivation for the generalized Heisenberg Hamiltonian (1.1) is as follows. The first derivative of spin operator is given by this equation

$$\frac{\partial S_n^\alpha}{\partial t} = \frac{1}{i\hbar} \left[S_n^\alpha, \mathcal{H} \right], \tag{1.5}$$

with the form $\mathcal{H}$ (1.1) give

$$\frac{\partial S_n^\alpha}{\partial t} = \frac{1}{i\hbar} \left\{ \sum_{i,\beta} B_i^\beta \left[S_n^\alpha, S_i^\beta \right] + \sum_{\substack{i,j \\ \beta,\gamma}} \mathcal{J}_{ij}^{\beta\gamma} \left(\left[S_n^\alpha, S_i^\beta \right] S_j^\gamma + S_i^\beta \left[S_n^\alpha, S_j^\gamma \right] \right) \right\}, \tag{1.6}$$

where the sub-indices i, j, n denotes the index of the localized spin. After using the commutator relations $\left[S_n^\alpha, S_i^\beta \right] = 2\mathrm{i} \sum_\gamma \varepsilon^{\alpha\beta\gamma} S_n^\gamma \delta_{ni}$, we obtain

$$
\frac{\partial S_n^\alpha}{\partial t} = \frac{1}{\mathrm{i}\hbar} \left\{ \sum_\beta B_n^\beta (2\mathrm{i} \sum_\gamma \varepsilon^{\alpha\beta\gamma} S_n^\gamma) \right.
$$
$$
\left. + \sum_{\substack{i,j \\ \beta,\gamma}} \mathcal{J}_{ij}^{\beta\gamma} \left(2\mathrm{i} \sum_{\gamma'} \varepsilon^{\alpha\beta\gamma'} S_n^{\gamma'} \delta_{ni} S_j^\gamma + S_i^\beta 2\mathrm{i} \sum_{\beta'} \varepsilon^{\alpha\gamma\beta'} S_n^{\beta'} \delta_{nj} \right) \right\}, \tag{1.7}
$$

After simplification this leads to the important equation describing the spin dynamics in a generalized Heisenberg model

$$
\frac{\hbar}{2} \frac{\partial S_n^\alpha}{\partial t} = \sum_{\beta\gamma} \left(\varepsilon^{\alpha\beta\gamma} B_n^\beta S_n^\gamma + \overbrace{\sum_{j,\mu} \left(\varepsilon^{\alpha\beta\mu} J_{nj}^{\beta\gamma} S_n^\mu S_j^\gamma + \varepsilon^{\alpha\gamma\mu} J_{jn}^{\beta\gamma} S_j^\beta S_n^\mu \right)}^{\text{spin current}} + \text{h.c.} \right), \tag{1.8}
$$

where α, β, γ, μ are spin components that can be $\{x, y, z\}$ and $\varepsilon^{\alpha\beta\gamma}$ is the Levi-Civita symbol. In Eq. (1.8) two parts can be distinguished, one that depends on the effective magnetic field and the second that depends on the exchange interactions and is related to the spin current [10, 11]. Thereafter, the symmetry break is affecting the coupling constants and induces a spin current. Therefore, it can be concluded that a spin state can be affected by a local magnetic field causing precession or by the spin current term.

1.3   Quantum-state transfer in a frustrated spin chain

The quantum simulations of the correlated spin dynamics are usually limited to small systems. Within some approximations, it is often possible to obtain a ground state. In many cases, a ground state and excited states are needed where one resorts to the **density matrix renormalization group**(DMRG) that uses the decomposition of the system to smaller blocks. On the other hand, for classical simulations, one may employ the **Landau-Lifshitz-Gilbert**(LLG) equation for which solution computer modeling codes are well developed. Tools like **Object Oriented MicroMagnetic Framework**(OOMMF) [24] and **muMax** [25] are examples of this type of calculation. However, for finite systems and low dimension of

the order parameter the quantum fluctuation and the versatility of a quantum trends can not be neglected.

The discussed examples for the quantum Heisenberg model are important for studying the transfer of the quantum state between different parts of a spin chain. The exchange interactions are important and without them there is no spin current and a transfer of the quantum state is not possible. The external fields can induce a spin current and possibly moderate effectiveness of quantum communication. In the end, all of the effective fields and interactions can be manipulated by changes in the environment properties.

As of key importance for a quantum state transfer are fast and secure communication channels. In currently used transport protocols even the encrypted data could be potentially imperceptibly caught by man-in-the-middle attack (eavesdropped). The communication protocol based on entangled particles can not be intercepted without any notice. We will transfer a single qubit with reasonable fidelity within a finite time t_s. Where the transfer fidelity is the transition amplitude between initial and final states [12].

A small disturbance of the communication channel which is quantum, might influence the specific time or even destroy the original message. A proper selection of the quantum channel is therefore crucial for stability and roughness of the protocol. Another criterion is the distance between the ends of the communication channel. A prominent example is an optical channel used for long and short distances. The point of interest is to study quantum channels in the nanoscale regime. Therefore, due to long decoherence time and the possibility of controlling the transfer fidelity, an appropriate candidate is the quantum channel based on a solid-state spin chain.

The communication protocol: Alice $\rightarrow$ Bob example   A theoretical study of the quantum channel for the unmodulated ferromagnetic spin chain was put forward by S. Bose [6]. The state is transmitted from one localized spin of the chain and received in another with desirable fidelity after specific transmission time. The state which Alice want to send is not fixed and can evolve during the transmission time, as it is shown in Fig. 1.3. Due to the presence of magnetic field the received state might be not even close to the state which Alice wants to send. In order to achieve the highest averaged fidelity transfer, Bob has to wait for a specific
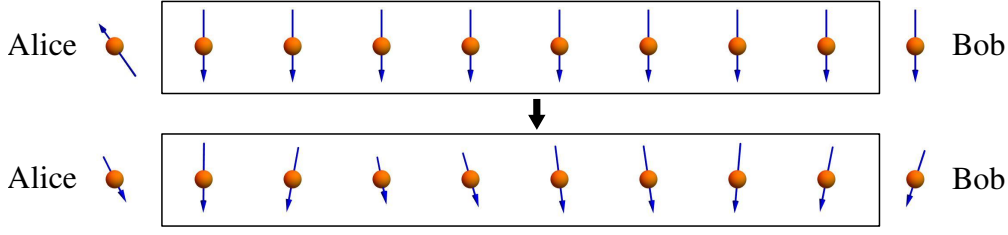
Figure 1.3: The quantum-state transfer in an Alice $\rightarrow$ Bob example of the communication protocol. The state which Alice sends to Bob is not fixed and evolve in time.

time which is sufficiently long and the magnitude of the external magnetic field could be properly adjusted as it was considered by Bose [6].

Spin-1/2 frustrated chain Let us consider another example with a rewritten Hamiltonian (1.1) for the nearest(i, $i + 1$) and next-nearest(i, $i + 2$) neighbor interactions only, including contribution of the polarization and the magnetic field.

$$\hat{\mathcal{H}}(t) = -\mathcal{J}_1 \sum_{i=1}^{N-1} \vec{S}_i \cdot \vec{S}_{i+1} - \mathcal{J}_2 \sum_{i=1}^{N-2} \vec{S}_i \cdot \vec{S}_{i+2} - \gamma_e \hbar \mathcal{B}^z \cdot \sum_{i=1}^{N} S_i^z - g_{ME} \vec{E} \cdot (\vec{P}_0 + \vec{P}(t)) \quad (1.9)$$

where the polarization [10] is the last term and it reads $\vec{P}_0 \sim \vec{r}_{i,i+1} \times \left(\vec{S}_i \times \vec{S}_{i+1} \right)$, whose origin was mention in the context of spin-current. Its time-dependency will be considered in this section. The spin chain is along the x-axis, thus the vector $\vec{r}_{i,i+1}$ pointing between neighboring localized spins has only x-component, whereas the constant external magnetic field is in the z-axis and the considered polarization is written with the y-axis component of the electric field allowing to keep the block diagonal structure of the Heisenberg Hamiltonian written in S^z basis. As it is shown in Fig. 1.3, the system is initially at $t = 0$ in its ground state, where one of the states was manipulated by the sender(Alice flipped the spin or in general set an unknown state). Thus the deviation from the ground state will result in a spin precession, where a finite-time τ named later as the specific time needed for the receiver to get as close as possible to the sender state at $t = 0$. The Hamiltonian (1.9) describes now the spin chain which can be different from the ferromagnetic ground state.

Fidelity of localized spins As the first step of investigation for QST, the time-dependent polarization term is temporarily neglected in the Hamiltonian (1.9). It should be noticed, that for the communication protocol the shared collective many-particle entanglement should

be supported. This is the case for the influence of the electric field on the chiral state in a frustrated spin system[12]. The averaged fidelity F_{js} of the quantum state transfer from state $|j\rangle$ to state $|s\rangle$ has been defined by Bose [6]

$$F_{js}(E, B, t) = \frac{1}{2} + \frac{|f_{js}(E, B, t)| \cos \gamma}{3} + \frac{|f_{js}(E, B, t)|^2}{6}, \tag{1.10}$$

where $\gamma = \arg \{f_{js}(E, B, t)\}$. Starting from the initial wave function in the one-excitation basis

$$|\psi(t_0)\rangle = a |0\rangle + b |s\rangle, \tag{1.11}$$

where a single qubit state $|a|^2 + |b|^2 = 1$ is normalized

$$|\psi(t)\rangle = a |0\rangle + b \sum_{j=1}^{N} f_{js}(E, B, t) |j\rangle, \tag{1.12}$$

and $f_{js}(E, B, t)$ is the transition probability

$$f_{js}(E, B, t) = \langle j| \exp(-i\hat{\mathcal{H}}t) |s\rangle. \tag{1.13}$$

As a result, the transfer fidelity with the static external electric field can be calculated. Figs. 1.4, 1.5 show results for a chain with $L = 10$ from which it can be concluded that high electric field has a negative influence on the transfer fidelity. Indeed, higher-fidelity
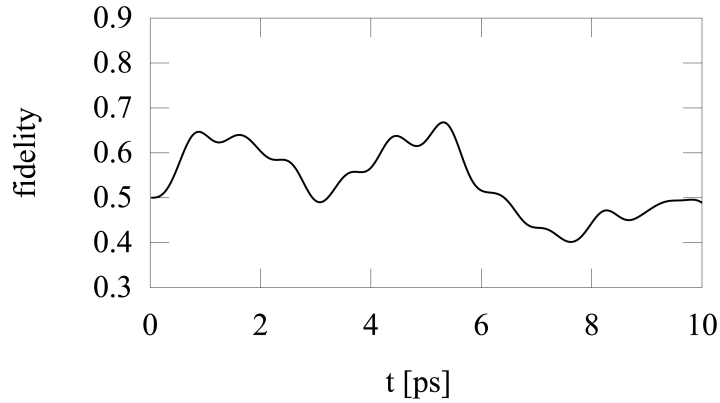
Figure 1.4: Fidelity of the quantum state transfer, low electric field

can be achieved in the presence of an external electric field, but since the specific time is narrowed, there is less time for the sender to set up the initial state and for the receiver to accomplish the reading procedure. It was assumed that all of the atoms were fixed and under the influence of external fields, it would not change.
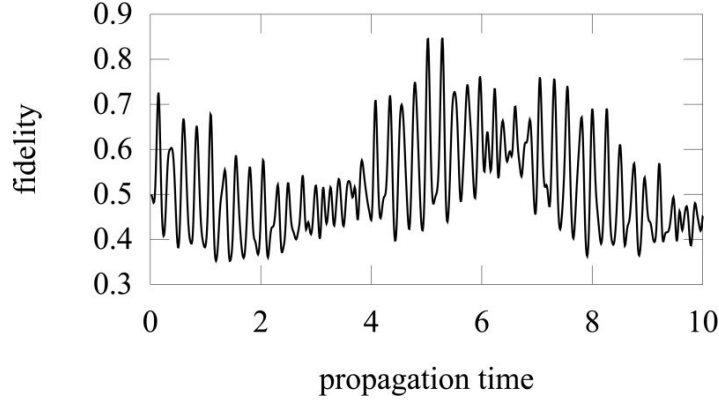
Figure 1.5: Fidelity of the quantum state transfer, high electric field

Fidelity with time dependent coordinates   Let us allow for the localized spin to change its position. From the inverse piezoelectric effect in the environment, one can expect small dislocation of atoms under an applied external electric field. Therefore, the influence of lattice vibrations on the quantum state transfer is treated semi-classically by propagating the wave function in time

$$|\psi(t)\rangle = \hat{U}(t, t_0) |\psi(t_0)\rangle, \tag{1.14}$$

where $\hat{U}(t, t_0)$ is the evolution operator

$$\hat{U}(t, t_0) = \hat{\mathcal{T}}\left(\exp\left[-\mathrm{i}\int_{t_0}^{t} d\tau \hat{H}(\tau)\right]\right). \tag{1.15}$$

$\hat{\mathcal{T}}$ is the time-ordering operator and τ is the classical time in which movement happens. To compute the fidelity with time-dependent coordinates the following transition probabilities is used in Eq. (1.10)

$$f_{js}(E, B, t) = \langle j| \hat{U}(t, t_0) |s\rangle. \tag{1.16}$$

In time-dependent Hamiltonian (1.9) the polarization vector has to indicate the fact of changing distances between sites and will take the following form

$$\vec{P}(t) \sim [x_{i+1}(t) - x_i(t)]\hat{e}_x \times \left(\vec{S}_i \times \vec{S}_{i+1}\right)_z, \tag{1.17}$$

where the z-component is taken to indicate that the external electric field is in y-axis and $x_i(t)$ is the i-th time-dependent position of the site. The influence of different dynamics on the quantum state transfer is shown in comparison at the end of this section.

1. Rocking Newton's Cradle   We will simulate the time-dependent coordinates of the spin chain sites in a way similar to Newton's Cradle. This simulation is for a granular crystal chain [26, 27] while assuming all material properties of steel. The underlying mechanism mimics connections of all spins with their neighbors by Hertzian contact. The equation of motion [28] is written in the following form

$$\ddot{x}_i = k\xi_{i-1,i}^{\alpha} - k\xi_{i,i+1}^{\alpha} + k_G\left(x_i^{(0)} - x_i\right), \tag{1.18}$$

where $\xi_{i,i+1}$ denotes an overlap between the two neighboring grains, with $\alpha = \frac{3}{2}$ (Hertz law), $k_G = \frac{mg}{L} = 9.33 \times 10^9$ kg s^{-2} is the gravitational spring constant where L is the length of the inelastic string, m is the mass of the Cradle ball, and g is the gravity acceleration, $k = 3.18$ N m$^{-3/2}$ is the spring constant[1], $x_i^{(0)}$ is the equilibrium position of i-th site and x_i is the displacement from equilibrium. The Fig. 1.6 shows in a schematic way the system of
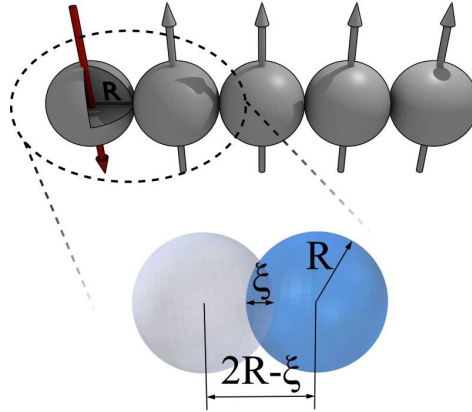
Figure 1.6: Schematic representation of the Cradle system.

interest, $\xi_{m,n} = (2R - (x_m - x_n))_+$, where $+$ means $\xi_{m,n} = 0$ for $2R - (x_m - x_n) < 0$. From the numerical simulation for the equation of motion Eq. (1.18), as shown in Fig. 1.7 it can be noted that the main exchange of the kinetic energy occurs between the ends of the system, while the transfer between neighboring sites happens nearly instantly. The amount of energy redistributed between the rest of the system could be neglected.

2. Morse potential   Yet, more realistic modeling of the sites motion can be realized within Morse potential. This is an adequate approach for molecular dynamics. The Hamiltonian [29,

---

[1]Hertzian spring $F = k(x_n - x_{n+1})^{\alpha}$
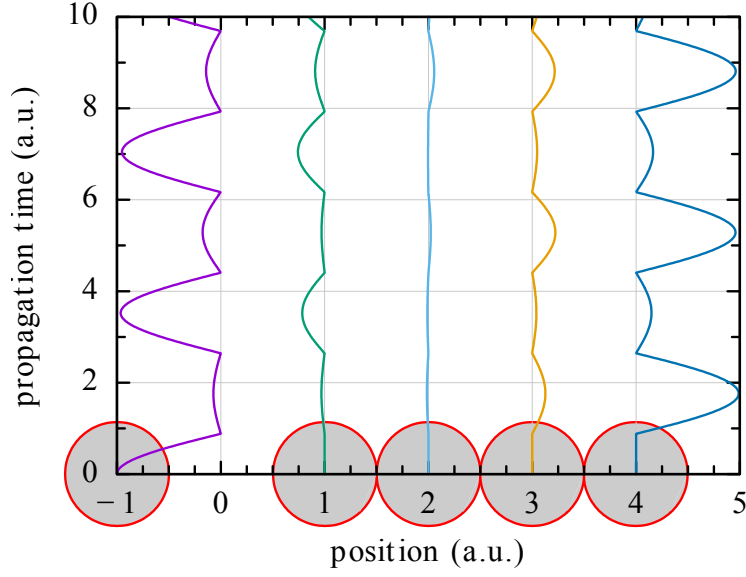
Figure 1.7: The Cradle effect for radius $R = 0.5$

30], without tension $f(x_i - x_i^{(0)})$ has the following form

$$H(x_i, p) = \sum_i \frac{p_i^2}{2m} + V_M(x_i),$$
(1.19)

where Morse potential V_{M_i} is

$$V_M(x_i) = D_0 \left[1 - e^{-\beta(x_i - x_i^{(0)})}\right]^2,$$
(1.20)

or equivalently can be written as

$$V_M(x_i) = D_0 \left[e^{-2\beta(x_i - x_i^{(0)})} - 2e^{-\beta(x_i - x_i^{(0)})}\right]^2,$$
(1.21)

where for numerical simulations the following set of parameters were taken [30]; $D_0 = 2.0$eV is Morse dissociation energy, $\beta = 1.95$Å^{-1} is the Morse parameter, $x_i^{(0)} = 2.28$Å i is the lattice constant times i-th site index. Figs. 1.8, 1.9 shows the displacements for different boundary conditions, where one can notice the difference to the Newton's Cradle results, mainly fast thermalization and the necessity to introduce additional potential preventing system fragmentation. Furthermore, the transfer of the kinetic energy requires some time.

Fidelity comparison

The following Fig. 1.10 shows the transfer fidelity under an external electric field and the different mechanisms for the dynamics. It should be noted that the effect of the time-dependent
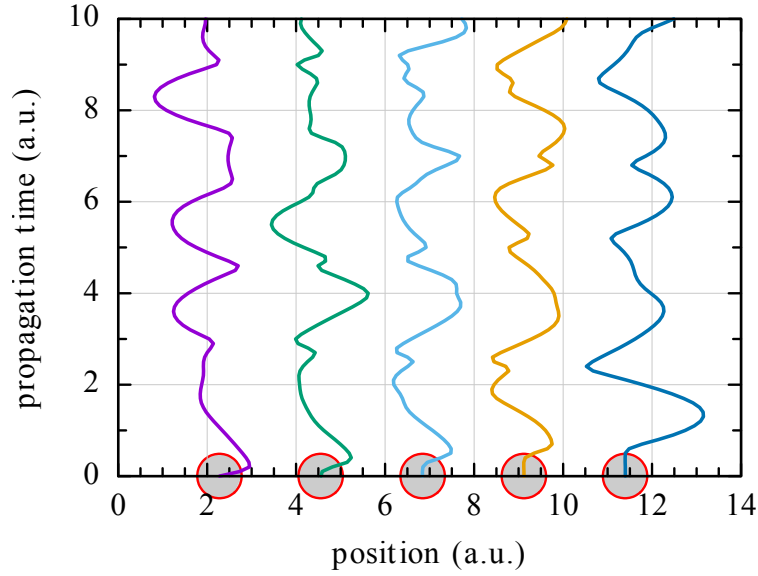
Figure 1.8: The dynamic motion in Morse potential with confinement potential $V = 2x^2$ as boundaries.
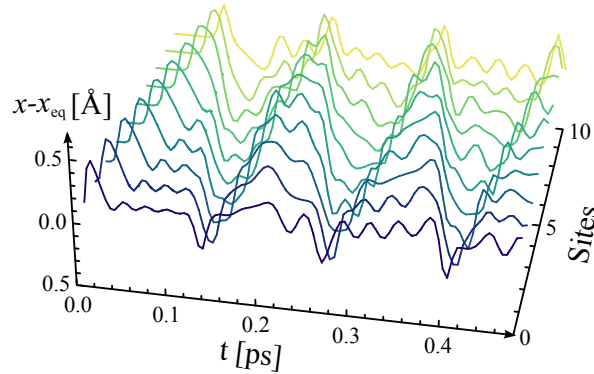
Figure 1.9: The dynamic motion in Morse potential with the reflections that take place due to the hard core potential at the system boundaries.

polarization vector can have an influence on the quantum state transfer only if the system is not in the ferromagnetic phase. It was already shown Fig. 1.5, that high-electric field can have an influence on the transfer fidelity making it difficult to define the specific time t_s. On the another hand, for the Cradle or Morse(molecular) types of motions the average distance between the sites is larger, therefore the expected communication time is longer.

3. Double Morse potential Symmetrizing the Morse potential creates two separate 'pockets' around any nuclei where the electrons can stay. A similar picture is a chain of MnO_2
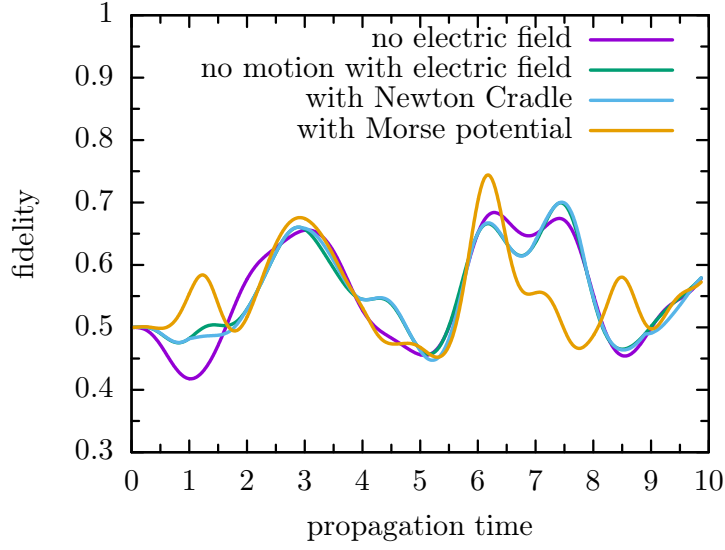
Figure 1.10: Time dependence for fidelity of the quantum state transfer through the chain of $L = 10$ spins. Values of the parameters: $\frac{\gamma_e \hbar}{2\pi} B = -0.38$meV, $g_{ME} E = 31.2 \frac{\text{keV}}{\text{Cm}}$, $J_1 = 7$meV, $J_2 = -7$meV and for classical Newton's Cradle, $\alpha = 3/2$, $k_G = 9.33 \times 10^9$kg s^{-2}, $k = 3.18$N m$^{-3/2}$. The time scale is $\hbar/J_1$.

where the oxides could be pushed out from one atom of Mn to another. The following mechanism is used together with an additional electric field pulse or another type of pulses such as a phonon pulse, to achieve a temporal communication or a quantum state transfer blockade. The Hamiltonian in comparison with (1.19) has a different potential

$$H(x,p) = \frac{p^2}{2m} + V_{DM}, \tag{1.22}$$

where V_{DM} is a double potential constructed from two Morse potentials that reads

$$V_{DM}(i,x) = D_0 \left[1 - \exp\left(-\beta(x - (2i-1)x^{(0)}) \right) \right]^2 \left[1 - \exp\left(-\beta(x - 2ix^{(0)}) \right) \right]^2, \tag{1.23}$$

where i is the index of the double potential between the two localized spins $\vec{S}_i$ and $\vec{S}_{i+1}$. It should be noted that each of the localized spins in this toy model has two Morse potentials. The particle can stay in one of the valleys, see Fig. (1.11) which is related to the Morse potential from left or right nuclei. If those nuclei are too close to each other, there might be only one minimum of the common potential. The charges hop between the nucleus and interact with each other

$$H(x,p) = \sum_{i=1}^{n} \frac{p_i^2}{2m_i} + V_{int}^B + V_{DM} + V_{int}^F, \tag{1.24}$$
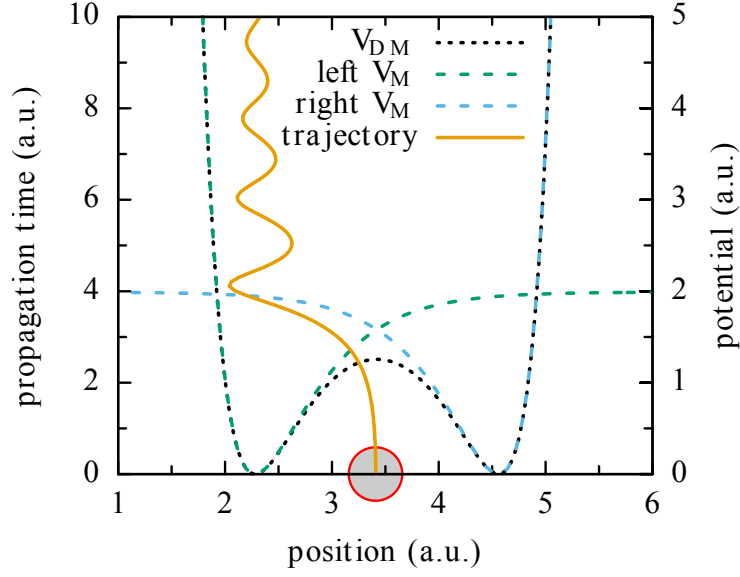
Figure 1.11: Construction of the double Morse potential V_{DM} from two separate Morse potentials with dissociation energy $D_0 = 1.99$eV and $\beta = 1.94$Å^{-1} from left and right nucleus. The solid line show an example of trajectory for charged particle with damping.

where V_{int}^B and V_{int}^F are repulsive interaction potentials between the nearby charged particles

$$V_{int}^B = -\frac{\exp(-a(x_i - x_{i-1})^2)}{b(x_i - x_{i-1})}, \quad i > 1, \tag{1.25}$$

$$V_{int}^F = -\frac{\exp(-a(x_{i+1} - x_i)^2)}{b(x_{i+1} - x_i)}, \quad i < N. \tag{1.26}$$

where $a = 0.45$Å^{-1}, $b = 0.01$eV^{-1}Å^{-1}. The excitation is done by hand, by setting up the velocity of the selected particle. The main advantage of this mechanism is that the atoms in the spin chain are still localized. Fig. 1.12 presents with thick lines the trajectories of charges and all double Morse potentials for a spin chain with $N = 5$ sites and the maximum interaction potentials between the neighboring charges. The parameters of the Morse potential are based on the Br$_2$ molecule [30]. Figs. 1.13 show the transfer of the kinetic energy and the same trajectories with exchanged axis without potentials. The small applied damping makes it easier to achieve a Cradle effect or a motion in Morse potential. As it is shown in Fig. 1.14 without damping, the result is more similar to the dynamic within a single Morse potential, but there is no fast thermalization. The kinetic energy is mainly transferred between the charges at the end of the 'chain'.

This toy model is only to represent the schematic charge mediated the spin current which
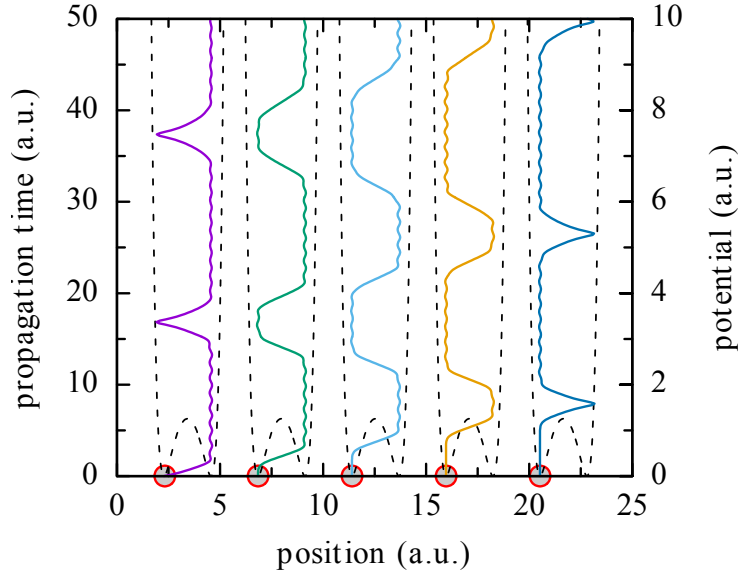
Figure 1.12: The trajectories of charged particles (solid lines) in double Morse potentials (dashed line) with damping $d = 0.01$, initial velocity $v_1 = 2.2$, $D_0 = 1.99$eV, $r_0 = 2.28$Å, $\beta = 4.432/r_0$. For interaction potential parameters $a = 0.45$Å^{-1}, $b = 0.01$eV^{-1}Å^{-1}.
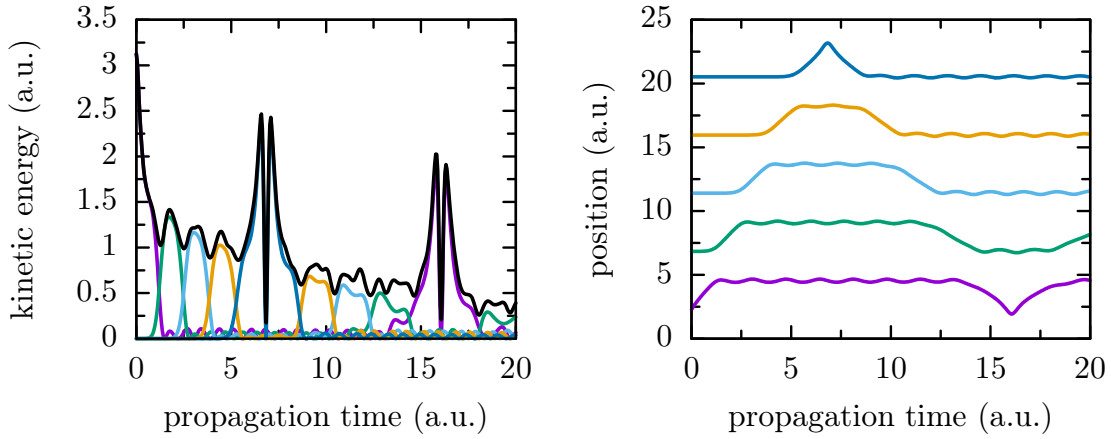
Figure 1.13: Damping $d = 0.03$, initial velocity $v_1 = 2.5$, $D_0 = 1.99$eV, $r_0 = 2.28$Å, $\beta = 4.432/r_0$. For interaction potential $a = 0.45$, $b = 0.01$.

possibly can happen within the environment. There are only electrons/oxides in motion which belong to different atoms and therefore it can not be compared to previously mentioned mechanisms because the polarization vector is no longer time-dependent, but it has an influence on the effective spin-interaction strength. Also, to see significant changes it has to be mediated by collective excitations of many charges. This mechanism can inherit a sim-
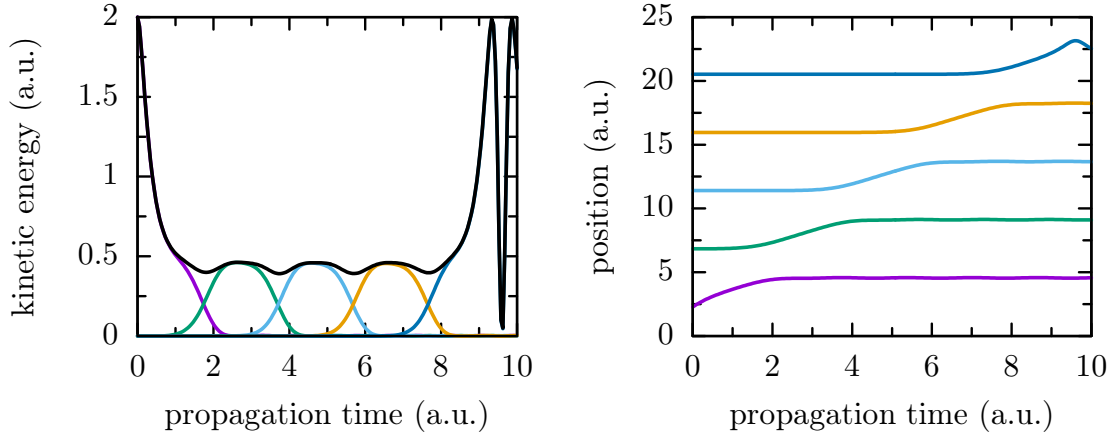
Figure 1.14: Without damping $d = 0.0$, initial velocity $v_1 = 2.0$, $D_0 = 1.99$eV, $r_0 = 2.28$Å, $\beta = 4.432/r_0$. For interaction potential $a = 0.45$, $b = 0.01$.

ilar polarization scheme to the one occurring in a GaAs doped with Mn magnetic impurities where the magnetization happens due to charges neighboring to the Mn atoms, which is explained in section 3.5. In modern research, a similar mechanism is observed for pyrocarbon chain where the carbon dioxides are shared[31] or transfer the proton in another system[32].

1.4 Many-body localization

Nowadays, the fast and reliable quantum communication channel with high fidelity transfer described in the previous section is only one of the most demanded features. Another one is a device for storing quantum information. One can imagine that due to changes in the properties of the environment, the localized spin-exchange interactions are reduced, so part of the spin chains are separated and less interacting with the environment and therefore could store information such as the states are magnetized in particular direction or not. However, a difficulty for the applications is the demagnetization of those states [33].

We focus on localization in strongly interacting many-body systems with the short-range interactions. A part of the system may act as own bath [13]. The statistical distribution of the level spacings can be used to properly characterize if the system is in a localized phase. Let us first consider several characteristic equalities with respect to the eigenvalues level spacings in Hamiltonian (1.9) without time-dependent polarization term. It is important to note that

the change of a uniform magnetic field B^z applied to all states, causes only a linear shift of all eigenvalues in the same direction and does not affect the level spacings. A change of the sign in nearest-neighbor $\mathcal{J}_1$ coupling is not important. Thus, level spacings are the same for the ferromagnetic chain as for the antiferromagnetic chain in the case of Heisenberg Hamiltonian. For a chosen direction of the electric field, a change of sign also is not relevant, because the eigenvalues depend on $\mathcal{D}^2$. Therefore, it can be safely assumed that the change of J_1 sign leads from $\mathcal{H}$ to $-\mathcal{H}$, with no influence on the level spacings unless the next-nearest neighbor coupling is finite. Following the work of Lutiz et. al. [14], and other cited papers
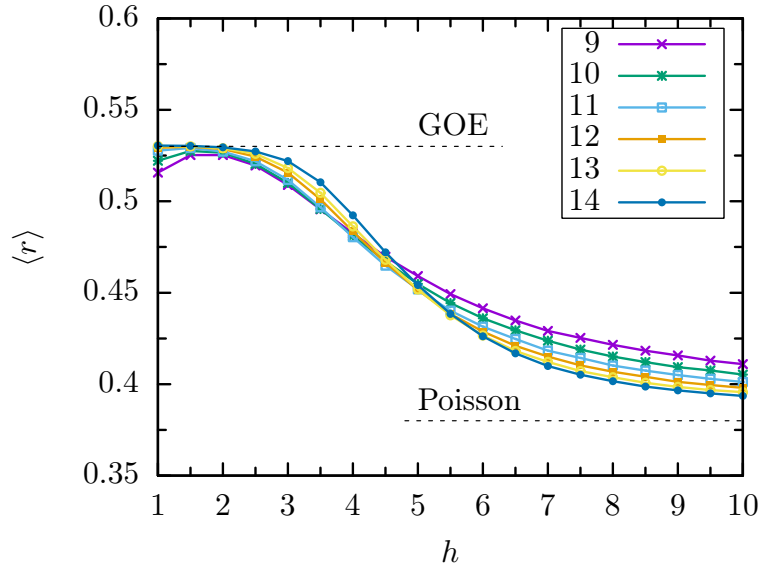
Figure 1.15: Averaged level spacings $\langle r \rangle$ as a function of disorder h for $L = \{9, 10, 11, 12, 13, 14\}$.

therein, the ratio of consecutive level spacings r_n will be used instead of the traditional level spacing δ_n

$$r_n = \frac{\min\left(\delta_n, \delta_{n+1}\right)}{\max\left(\delta_n, \delta_{n+1}\right)}, \tag{1.27}$$

where δ_n is the level spacing between E_n and E_{n+1}. The consecutive level spacing r for one disorder realization is found as an average $\langle r_n \rangle$. The disorder is introduced in z-component of magnetic field B_i^z which can be different on each site of the system

$$B_i^z \in \langle -h, h \rangle, \tag{1.28}$$
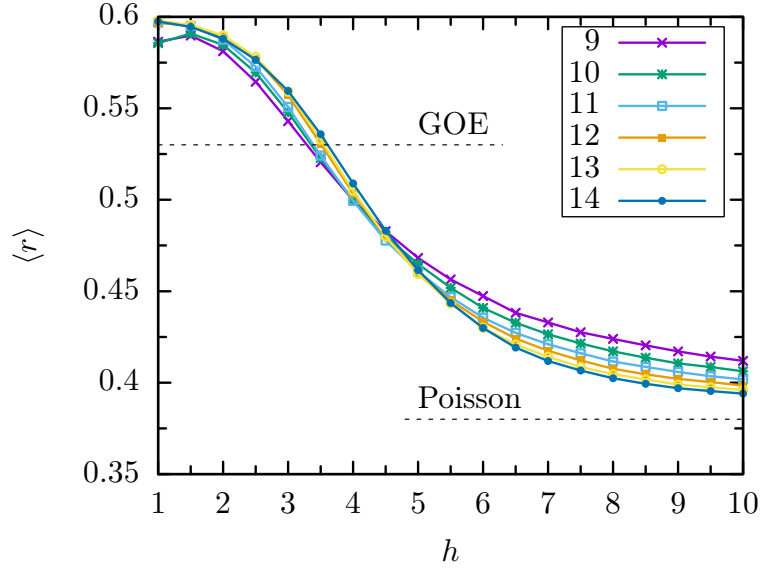
Figure 1.16: Influence of DMI, $\mathcal{D} = 0.2$ is a shift from GOE to GUE statistics.

where each point of the curves from Figs. 1.15, 1.16 requires at least 4000 realizations at fixed a disorder strength h.

The critical disorder h_c above which a transition to MBL phase occurs can be estimated in different ways. Since a numerical exact diagonalization is available only for a limited size of the system (large Hilbert space 2^L) and the system of interest are non-integrable, a finite size scaling is needed.

For finding the level spacings only the biggest block of the Hamiltonian is taken into account where $S^z = 0$ for even L or $S^z = \pm 1$ for odd. Where L is the number of sites in the system. Recall that the generalized Hamiltonian (1.1) can be used for considering 1D spin chain as well as 2D clusters or 3D structures also with periodic boundary conditions. Currently, the only limitation for numerics is the number of atoms which can be taken into the account. Still, for many-body localized phase, probably 1D chains are useful candidates. Fig. (1.15) shows one of the easiest possibilities to identify the critical disorder. Increasing the system size L the curves become steeper and crossings appear closer to one point which can be taken as the critical disorder h_c. In the ergodic phase, the statistical distribution of level spacings should follow the Gaussian Orthogonal Ensemble(GOE; Wigner) $\langle r_n \rangle \approx 0.53$

which is the case shown in Fig. (1.15). The statistical distribution of the level spacings in the non-ergodic localized phase follows a Poisson distribution[14]. Introducing DMI into the system can change the statistics to that following the Gaussian Unitary Ensemble(GUE) $\langle r_n \rangle \approx 0.59$ [34], but only for periodic spin chain [35] and with relatively large DMI $\mathcal{D} = 0.2$ shown in Fig. (1.16), which is roughly ten times larger than normal. What comes out, the non-periodic/open system had GOE type statistics. The system without next-nearest neighbor interaction can be mapped to the Affleck Hamiltonian [35] by a rotation and the imaginary part disappears while still keeping the same eigenvalues of the Hamiltonian. Following this
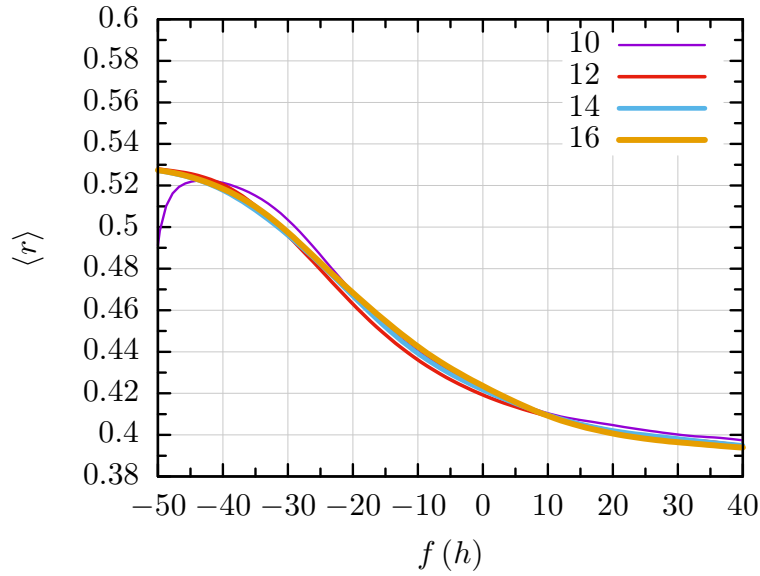
Figure 1.17: The result of scaling procedure for the system with $\mathcal{J}_1$ interaction only.

way of finding the quantum phase transition, the range for critical disorder h_c is too much blurred. In work done by Luitz et. al. [14] uses the scaling procedure

$$f(h) = g \left[L^{1/\nu} (h - h_c) \right], \tag{1.29}$$

allowing for the curves to coincide. The ν is a fitting parameter. It seems, that there might be no global minimum while changing ν, although using similar parameters to those mentioned in Luitz's paper, the g polynomial function can be chosen differently with no unique results. This scaling procedure can be used to minimize the total overlap of data sets which works quite well for the system without DMI and $\mathcal{J}_2$ interactions, Fig. 1.17. When that is not the case, a better way is to find the first derivative of $\langle r \rangle$ and to minimize the distances of their

maxima. In fact for each point on Figs. 1.15, 1.16 about 10000 exact diagonalizations were
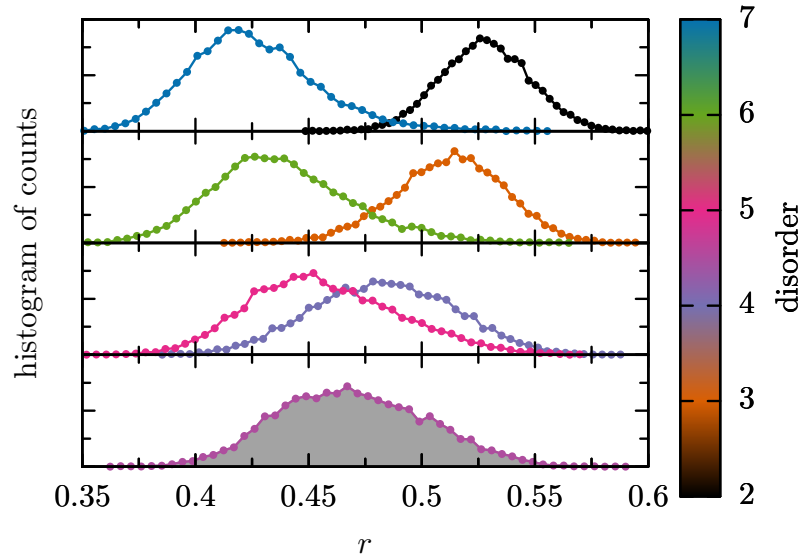
Figure 1.18: Histogram of counts for disorder realizations for a system's size of $L = 10$.

performed for obtaining a proper statistics, that allows to accurately estimate the averaged r over many realizations at a fixed strength of the disorder h. The computational cost can be reduced after the analysis of the histogram of counts for the distributions of r at a fixed h, Figs. 1.18, 1.19. The transition point to the many-body localization phase can be distin-
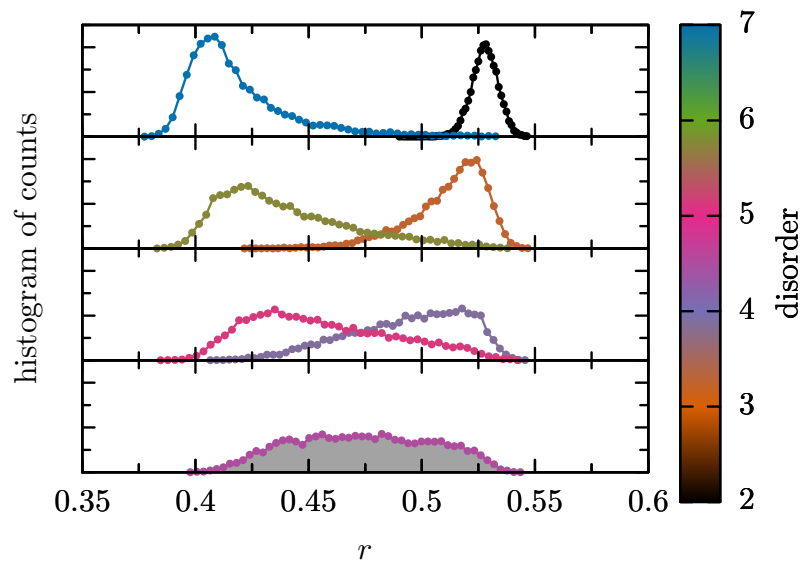
Figure 1.19: Histogram of counts for disorder realizations for a system's size of $L = 14$.

guished by a broadening of the histogram for a critical disorder. That is the new prospective way of identifying the critical disorder h_c for the transition to many-body localization phase in a finite-size system.

A further example of the fitted statistical distributions at different disorders is presented in Fig. 1.20. Numerical estimation of the full width at half height σ of each histogram of
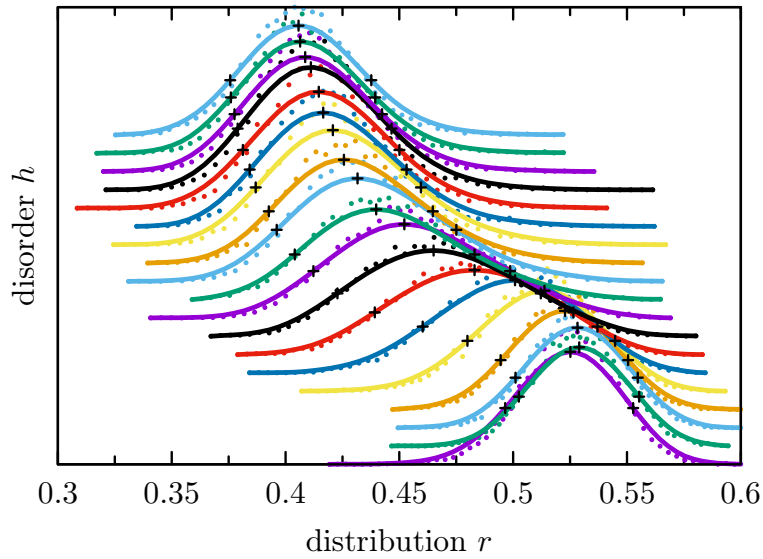
Figure 1.20: The probability distribution of r at different fixed h. The cross symbols marks the maxima and half heights of the distributions.

counts distributions was performed for different sizes of the system up to $L = 14$ with and without DMI, Fig. 1.21. The width of the histogram of counts is broader in the close vicinity of the critical disorder and $\sigma(h)$ with increasing L is more narrow which means that for the longer chains the critical MBL phase transition disorder is better defined. We see that the fluctuations have the similar peaks positions where in a close vicinity to the critical disorder the computed magnitudes are the largest but their calculation does not require any fitting function to the histogram. The smoothness depends on the number of realizations. Also, the quantum fluctuations decrease for a larger system size, which intuitively leads to the conclusion that the MBL phase is a quantum effect and is important for small ($L \simeq 12$) spin-1/2 systems. The strong disorder is important in a quantum device that could store qubit. The quantum state cannot be transferred when a system is in Many-body localized phase and
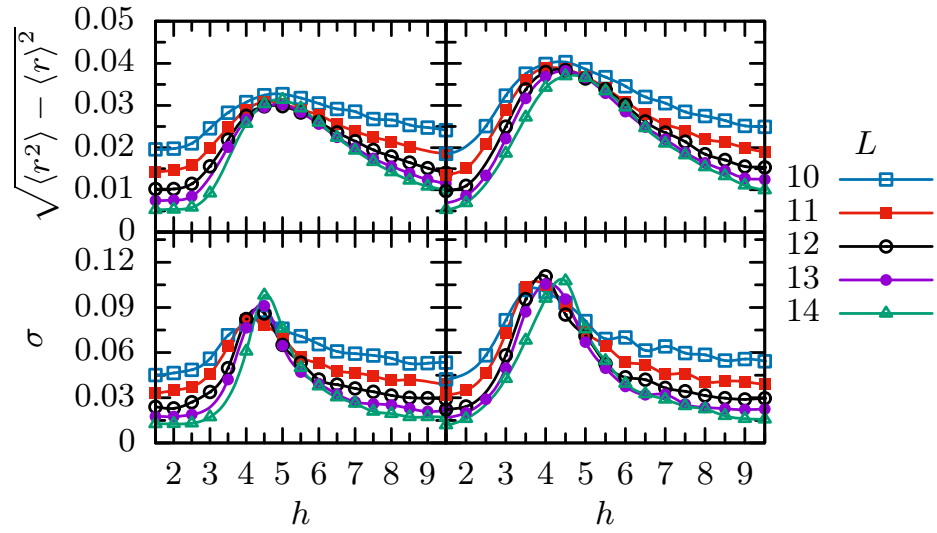
Figure 1.21: The enhanced broadening and quantum fluctuations as a function of disorder strength. The graphs on the left are without DMI and on the right for $\mathcal{D} = 0.2$.

thus it seems to be like without interactions.

Summary

The generalized form of the quantum Heisenberg Hamiltonian for representing the exchange coupling was defined. By using the continuity equation the precession and spin-current terms were revealed. As an example, the quantum Heisenberg model was used in studying the quantum state transfer. The extended calculation was done for frustrated spin-chain with DMI-aka spin polarization. As the main result, the impact of the external static and time-dependent electric field on the fidelity transfer was analyzed. Also, simplified classical toy model was proposed for studying the charge mediated spin-torque on localized spins. Afterward, the strong site-dependent disorder in the magnetic field was used to study the many-body localization phase transition. A new way of estimating the critical disorder through analyzing the quantum fluctuations was proposed and it shows the general validity also with frustrated systems.

The coupling of magnetic adatoms with the surface states of the topological insulator

In the previous chapter 1, mainly chains of atoms were discussed. In each case, the spin $S = \frac{1}{2}$ was the property of interest. Using Heisenberg model (1.1), it was possible to get a ground state of the system, its spin structure, precession of the spins in a chain with an initially flipped state (one excitation), a transfer of the quantum state between two sites of the chain and Many-body localization phase for highly excited states with a strong disorder in magnetic field.

In this chapter, the main focus is concentrated on the surface states of a topological insulator in the proximity of magnetic adatoms or multiferroic systems. The spin dynamics of deposited multiferroic materials or spin chains can be influenced by the substrate properties. As a result of this interplay, the interaction to the surface states of the topological insulator has an additional coupling to the electric field. An applied external magnetic field perpendicular to the surface of the topological insulator can open a band gap in the surface states. However, the influence of the internal magnetic effects can have different consequences on the electronic structure of the substrate. Perturbation theory provides an explanation of the influence of adatoms (or multiferroic chain) on the energy dispersion. Also, the spin dynamics is considered within the continuity equation. The mechanical force of the electron current acting on the spin chain is derived.

2.1   Insulating state

We distinguish two different origins of the spin current. The first one is related to the spin po-larized charge-current. The second to the collective excitation of the localized spins (magnonic spin current). The spin insulator means no charge-current but the spin-current [36] is finite. In semi-conducting or insulating states the conductivity tends to zero at temperature $T \to 0$K. The strong compression may lead to the metallic state [37] and sufficiently diluted materials may become insulating [38]. In a typical insulator material the energy bands namely the con-duction and the valence bands are split by about ~ 9eV band gap. For topological insulator, in bulk behaves as an insulator or semiconductor with its band gap. Due to spin-orbit inter-action, the surface states are not gapped and has a linear energy dispersion in the vicinity of the Dirac point.

2.2   The massless Dirac point model

Let us first consider the model of surface states in the topological insulator. The two-dimensional massless Dirac Hamiltonian [39] can be used as the simplest model for the surface states [40] when the inversion and the time-reversal symmetry are preserved

$$\hat{H}_0 = \sum_{k,\alpha,\beta} \psi_{\vec{k}\alpha}^{\dagger} h_{\alpha,\beta}(\vec{k}) \psi_{\vec{k}\beta}, \tag{2.1}$$

where $h_{\alpha,\beta}(\vec{k})$ is the local Hamiltonian with α, β spin up or down states

$$h_{\alpha,\beta}(\vec{k}) = \hbar v_F \left(k_x \sigma_x + k_y \sigma_y \right), \tag{2.2}$$

where $v_F \sim c/300$ is the Fermi velocity, $\hbar = 1$. The linear energy dispersion in vicinity of the Dirac point read $\varepsilon(\vec{k}) = \pm v_F |k|$. We will explore the role of the protection of the surface states in topological insulator when brought into contact with the chiral multiferroic chain.

2.3   The perturbation theory

The interaction of the surface electrons with magnetic moments of adatoms can be consid-ered in a perturbative way. The spin structure of the one-dimensional chain deposited on
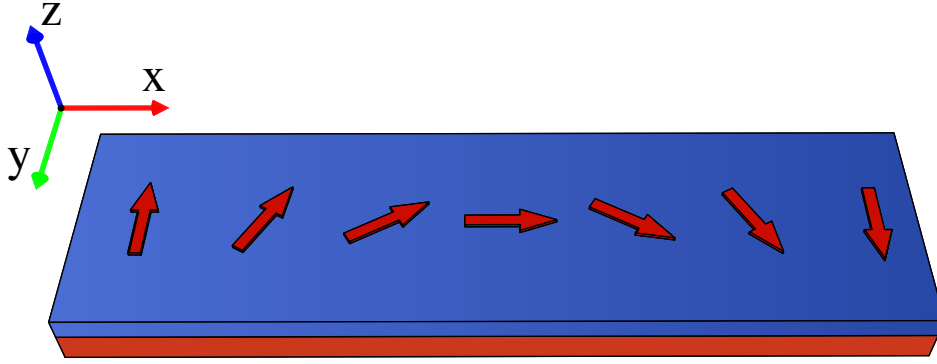
Figure 2.1: Schematic alignment of the spin texture along x-axis, while the external-electric field applied along y-axis modifies the helicoid period and z-axis is perpendicular to the surface of topological insulator.

the surface can be estimated by classical Monte Carlo simulation[41, 42] of the Heisenberg Hamiltonian(1.1). The magnetization field originating from the multiferroic chain Fig. 2.1 with an applied external electric field along the y-axis has nearly zero z-component, and therefore can be described by $\vec{M}(\vec{r}) = M_0 \left(\cos(\vec{Q} \cdot \vec{r}), \sin(\vec{Q} \cdot \vec{r}), 0 \right)$. In term of the effective Hamiltonian

$$\hat{H} = \hat{H}_0 + \hat{V}, \tag{2.3}$$

where $\hat{H}_0$ is a 2D massless Dirac Hamiltonian(2.2) which describes the energy dispersion of the surface electrons and the perturbation is caused by a multiferroic chain

$$\hat{V} = g \sum_n \left(\sigma_x \cos\varphi_n + \sigma_y \sin\varphi_n \right), \tag{2.4}$$

where g is the coupling constant of the surface electron to the adatoms effective helicoidal magnetization field. To reduce the number of parameters, the system is scaled by v_F, thus the constant coupling parameter reads $g \to g/v_F$. The eigenfunctions of $\hat{H}_0$ take the following form

$$\left| \psi_{\vec{k}}^j \right\rangle = \frac{e^{\mathrm{i}(k_x x + k_y y)}}{\sqrt{2\Omega}} \begin{pmatrix} 1 \\ z_j \frac{|\vec{k}|}{k^{-z_j}} \end{pmatrix}, \tag{2.5}$$

where $k^{\pm} = k_x \pm \mathrm{i}k_y$, $\sqrt{2\Omega}$ is a normalization factor and $z_j = \begin{cases} 1, & j = \uparrow \\ -1, & j = \downarrow \end{cases}$, corresponds

to the components of the spinor. To indicate the periodicity of the magnetization field the $\vec{k}$ states are coupled with $\vec{k} \pm \vec{Q}$ states leading to six eigenfunctions

$$|\Phi_1\rangle = \left|\psi_{\vec{k}}^{\uparrow}\right\rangle , |\Phi_2\rangle = \left|\psi_{\vec{k}+\vec{Q}}^{\uparrow}\right\rangle , |\Phi_3\rangle = \left|\psi_{\vec{k}-\vec{Q}}^{\uparrow}\right\rangle ,$$
$$|\Phi_4\rangle = \left|\psi_{\vec{k}}^{\downarrow}\right\rangle , |\Phi_5\rangle = \left|\psi_{\vec{k}+\vec{Q}}^{\downarrow}\right\rangle , |\Phi_6\rangle = \left|\psi_{\vec{k}-\vec{Q}}^{\downarrow}\right\rangle . \tag{2.6}$$

In this basis the matrix elements are

$$\left\langle \psi_{\vec{\eta}}^{m} \left| \hat{H} \right| \psi_{\vec{\xi}}^{n} \right\rangle = z_m |\vec{\eta}| \, \delta_{z_m z_n} \delta\left(\vec{\eta} - \vec{\xi}\right)$$
$$+ g \left[z_n \frac{|\vec{\eta}|}{\eta^-} \delta(\eta_x - \xi_x - Q_x) + z_m \frac{|\vec{\xi}|}{\xi^-} \delta(\eta_x - \xi_x + Q_x) \right], \tag{2.7}$$

with the following matrix representation

$$\hat{H} = \begin{pmatrix} |\vec{k}| & A^* & B & 0 & -A^* & B \\[2mm] A & |\vec{k}+\vec{Q}| & 0 & A & 0 & 0 \\[2mm] B^* & 0 & |\vec{k}-\vec{Q}| & -B^* & 0 & 0 \\[2mm] 0 & A^* & -B & -|\vec{k}| & -A^* & -B \\[2mm] -A & 0 & 0 & -A & -|\vec{k}+\vec{Q}| & 0 \\[2mm] B^* & 0 & 0 & -B^* & 0 & -|\vec{k}-\vec{Q}| \end{pmatrix}, \tag{2.8}$$

where

$$A = g\frac{|\vec{k}+\vec{Q}|}{k^+ + Q_x}, B = g\frac{|\vec{k}|}{k^+}. \tag{2.9}$$

The eigensystem of the total Hamiltonian 2.3, 2.8 can be solved numerically.

$$|\chi_n\rangle = \sum_{p=1}^{6} \alpha_{np} |\Phi_p\rangle, \quad n = 1, ..., 6. \tag{2.10}$$

The obtained energy spectrum presented on Figs. (2.2, 2.3) has a zero energy gap at $\vec{k} = 0$ characteristic for topological insulators with linear dispersion even with a non-zero g coupling constant. When it comes to $g = 0$ the bands labeled with 3 and 4 are equivalent to linear dispersion $\varepsilon_{\pm}(\vec{k}) = \pm v_F |\vec{k}|$ for the Hamiltonian(2.2) H_0. The periodicity of the system in the direction of the helicoid depend on Q and defines the edge of the Brillouin zone at $k_x = Q/2$.
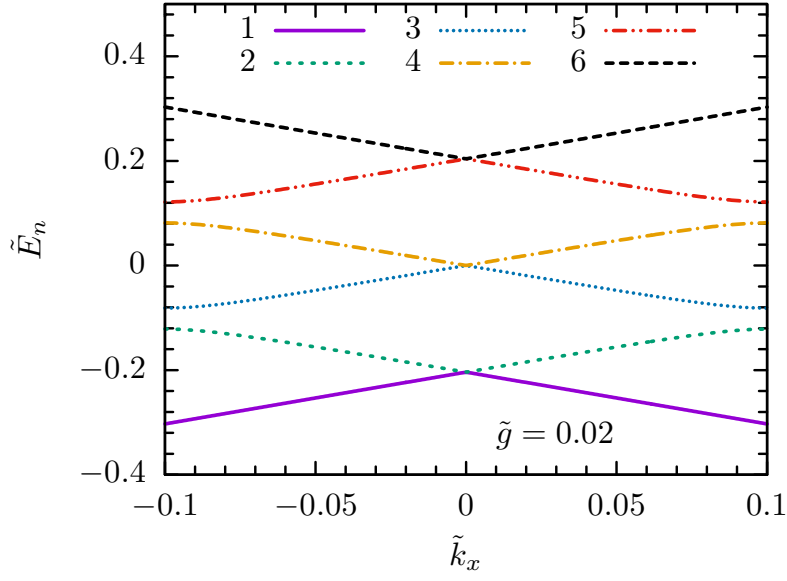
Figure 2.2: The energy dispersion E_n as a function of k_x with set of parameters $Q = 0.2$ and $k_y = 0$, $g = 0.02$.

The coupling of the surface states to the spiral magnetization field is mainly pronounced at this edge.

In the same basis(2.6) the components of electrons spin polarization are obtained in the following form for the x-component of the spin $1/2$ operator

$$s_x = \left\langle \psi_{\vec{\eta}}^m \left| \sigma_x \right| \psi_{\vec{\xi}}^n \right\rangle = \delta\left(\vec{\eta} - \vec{\xi}\right) \left[z_n \frac{\xi_x}{|\vec{\xi}|} \delta_{z_m z_n} + z_n \frac{i\xi_y}{|\vec{\xi}|}(1 - \delta_{z_m z_n}) \right],$$ (2.11)

and the matrix representation for x-component of the spin operator is

$$s_x = \begin{pmatrix} \frac{k_x}{|\vec{k}|} & 0 & 0 & -\frac{ik_y}{|\vec{k}|} & 0 & 0 \\ 0 & \frac{k_x + Q_x}{|\vec{k}+\vec{Q}|} & 0 & 0 & -\frac{ik_y}{|\vec{k}+\vec{Q}|} & 0 \\ 0 & 0 & \frac{k_x - Q_x}{|\vec{k}-\vec{Q}|} & 0 & 0 & -\frac{ik_y}{|\vec{k}-\vec{Q}|} \\ \frac{ik_y}{|\vec{k}|} & 0 & 0 & -\frac{k_x}{|\vec{k}|} & 0 & 0 \\ 0 & \frac{ik_y}{|\vec{k}+\vec{Q}|} & 0 & 0 & -\frac{k_x + Q_x}{|\vec{k}+\vec{Q}|} & 0 \\ 0 & 0 & \frac{ik_y}{|\vec{k}-\vec{Q}|} & 0 & 0 & -\frac{k_x - Q_x}{|\vec{k}-\vec{Q}|} \end{pmatrix}.$$ (2.12)
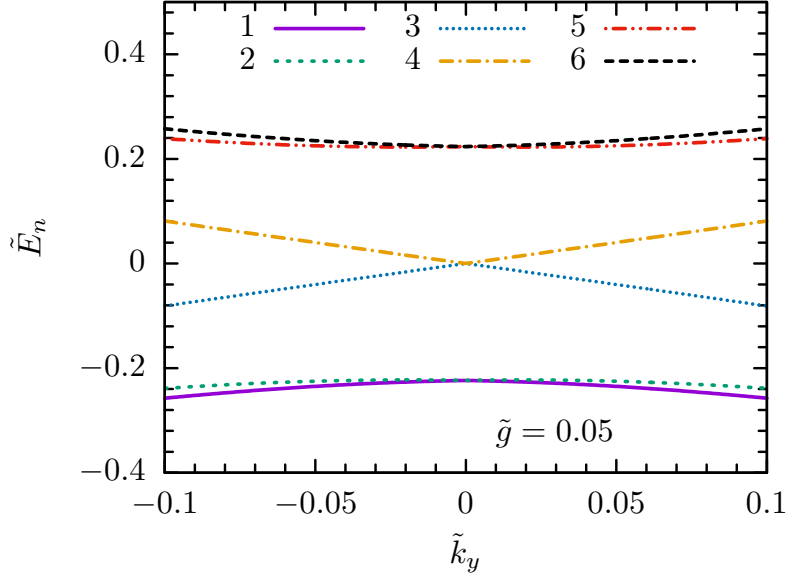
Figure 2.3: The energy dispersion E_n as a function of k_y with the set of parameters $Q = 0.2$ and $k_x = 0$, $g = 0.05$.

For the y-component of the spin operator

$$s_y = \left\langle \psi_{\vec{\eta}}^m \left| \sigma_y \right| \psi_{\vec{\xi}}^n \right\rangle = \delta\left(\vec{\eta} - \vec{\xi}\right) \left[z_m \frac{\xi_y}{|\vec{\xi}|} \delta_{z_m z_n} + z_m \frac{\mathrm{i}\xi_x}{|\vec{\xi}|}\left(1 - \delta_{z_m z_n}\right) \right], \tag{2.13}$$

and the corresponding matrix representation reads

$$s_y = \begin{pmatrix} \frac{k_y}{|\vec{k}|} & 0 & 0 & \frac{\mathrm{i}k_x}{|\vec{k}|} & 0 & 0 \\[2mm] 0 & \frac{k_y}{|\vec{k}+\vec{Q}|} & 0 & 0 & \frac{\mathrm{i}(k_x+Q_x)}{|\vec{k}+\vec{Q}|} & 0 \\[2mm] 0 & 0 & \frac{k_y}{|\vec{k}-\vec{Q}|} & 0 & 0 & \frac{\mathrm{i}(k_x-Q_x)}{|\vec{k}-\vec{Q}|} \\[2mm] -\frac{\mathrm{i}k_x}{|\vec{k}|} & 0 & 0 & -\frac{k_y}{|\vec{k}|} & 0 & 0 \\[2mm] 0 & -\frac{\mathrm{i}(k_x+Q_x)}{|\vec{k}+\vec{Q}|} & 0 & 0 & -\frac{k_y}{|\vec{k}+\vec{Q}|} & 0 \\[2mm] 0 & 0 & -\frac{\mathrm{i}(k_x-Q_x)}{|\vec{k}-\vec{Q}|} & 0 & 0 & -\frac{k_y}{|\vec{k}-\vec{Q}|} \end{pmatrix}. \tag{2.14}$$

The simplest z-components

$$s_z = \left\langle \psi_{\vec{\eta}}^m \left| \sigma_z \right| \psi_{\vec{\xi}}^n \right\rangle = \delta\left(\vec{\eta} - \vec{\xi}\right)\left(1 - \delta_{z_m z_n}\right), \tag{2.15}$$
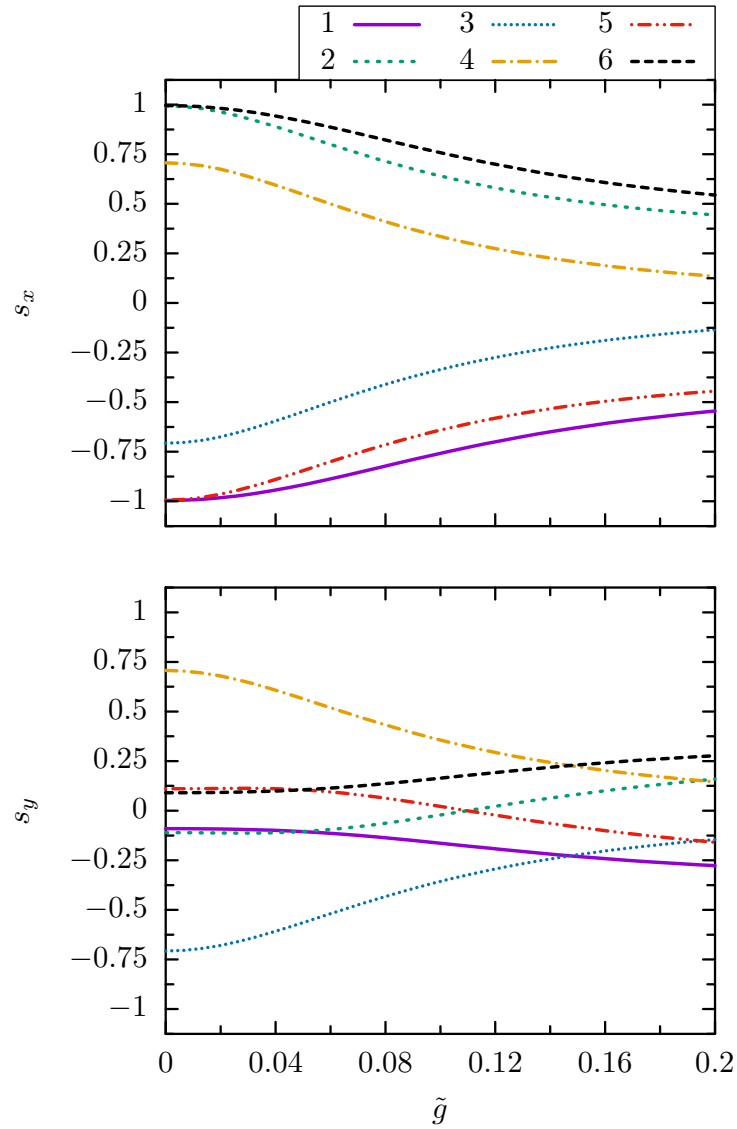
Figure 2.4: The averaged value of spin polarization $\vec{s}$ as a function of coupling constant g at $k_x = k_y = 0.02$ and $Q_x = 0.2$. The z-component of spin polarization s_z has zero mean value.

with its matrix form

$$
s_z = \begin{pmatrix}
0 & 0 & 0 & 1 & 0 & 0 \\
0 & 0 & 0 & 0 & 1 & 0 \\
0 & 0 & 0 & 0 & 0 & 1 \\
1 & 0 & 0 & 0 & 0 & 0 \\
0 & 1 & 0 & 0 & 0 & 0 \\
0 & 0 & 1 & 0 & 0 & 0
\end{pmatrix}.
\tag{2.16}
$$

The averaged values of spin polarization $\vec{s}$ are present in Fig. 2.4. Each of the lines corresponds to different eigenstates of the Hamiltonian(2.8) marked by the same colors and ordering like in Figs. (2.2,2.3). The spin polarization depends on n and k and is scaled linearly with the period of helicoid Q_h. Raising the strength of the coupling g to the magnetization field decreases the average spin polarization of the x and y components, while along z-axis it does not depend on g.

2.4 Spin density dynamics

Let us consider the spin dynamics of the substrate conductance electrons with the coupling to the magnetic adatoms. The macroscopic variation of the spin density of charges reads

$$\frac{\partial}{\partial t}\psi^{\dagger}\sigma_{\alpha}\psi \;\; = \;\; \frac{\mathrm{i}}{\hbar}\psi^{\dagger}\left[\hat{H},\sigma_{\alpha}\right]\psi, \tag{2.17}$$

where σ_{α} are Pauli matrices and further α,β,γ indicate spin component. After inserting into Eq. (2.17) the unperturbed Hamiltonian $\hat{H}_0$(2.2) for the two-dimensional system we integrate over the small area Ω

$$\frac{\partial}{\partial t}\int\limits_{\Omega} d^2\vec{r}\,\psi^{\dagger}\sigma_{\alpha}\psi \;\; = \;\; \int\limits_{\Omega} d^2\vec{r}\left(\frac{\partial\psi^{\dagger}}{\partial t}\sigma_{\alpha}\psi + \psi^{\dagger}\sigma_{\alpha}\frac{\partial\psi}{\partial t}\right), \tag{2.18}$$

and differentiate with respect to time t. Therefore, let consider separately the differentials over the time for the wave function ($\mathrm{i}\hbar\frac{\partial\psi}{\partial t} = \hat{H}_0\psi$) and its hermitian conjugation terms with unperturbed Hamiltonian $\hat{H}_0 = -\mathrm{i}v_F\sigma_{\beta}\nabla_{\beta}$, allowing to write

$$
\begin{aligned}
\mathrm{i}\hbar\frac{\partial\psi}{\partial t} &= -\mathrm{i}v_F\sigma_{\beta}\left(\nabla_{\beta}\psi\right) &\implies& \quad \frac{\partial\psi}{\partial t} &= -\frac{v_F}{\hbar}\sigma_{\beta}(\nabla_{\beta}\psi), \\
-\mathrm{i}\hbar\frac{\partial\psi^{\dagger}}{\partial t} &= \mathrm{i}v_F\left(\nabla_{\beta}\psi^{\dagger}\right)\sigma_{\beta} &\implies& \quad \frac{\partial\psi^{\dagger}}{\partial t} &= -\frac{v_F}{\hbar}(\nabla_{\beta}\psi^{\dagger})\sigma_{\beta}.
\end{aligned}
\tag{2.19}
$$

Eq. (2.18) thus reads

$$\frac{\partial}{\partial t}\int\limits_{\Omega} d^2\vec{r}\,\psi^{\dagger}\sigma_{\alpha}\psi \;\; = \;\; -\frac{v_F}{\hbar}\int\limits_{\Omega} d^2\vec{r}\left[\left(\nabla_{\beta}\psi^{\dagger}\right)\sigma_{\beta}\sigma_{\alpha} + \psi^{\dagger}\sigma_{\alpha}\sigma_{\beta}\left(\nabla_{\beta}\psi\right)\right], \tag{2.20}$$

leading to spin density dynamic equation

$$\frac{\partial s_{\alpha}}{\partial t} + \nabla_{\beta}\cdot j_{\beta}^{\alpha} = -\tau_{\alpha}, \tag{2.21}$$

where the spin density is $s_\alpha = \psi^\dagger \sigma_\alpha \psi$ and j is spin current

$$j^\alpha_\beta \;=\; \delta_{\alpha\beta} \frac{v_F}{2\hbar} \psi^\dagger \psi, \tag{2.22}$$

in the topological insulator associated with the free carriers angular momentum along the wave vector $\vec{k}$. Finally, τ is the relaxation term

$$\tau_\alpha = \frac{\mathrm{i}v_F}{2\hbar} \epsilon_{\alpha\beta\gamma} \left[\left(\nabla_\beta \psi^\dagger \right) \sigma_\gamma \psi - \psi^\dagger \sigma_\gamma \left(\nabla_\beta \psi \right) \right] + \frac{gM_\beta}{\hbar} \epsilon_{\alpha\beta\gamma} \psi^\dagger \sigma_\gamma \psi, \tag{2.23}$$

where the last term in Eq. (2.23) is due to the $\hat{V}$ (2.4) interaction with the magnetic adatoms that control the relaxation rate. The physical meaning of the relaxation term can be easily interpreted for an isolated system, where the coupling $g = 0$ is neglected. In this case, the relaxation term describes the decay rate of states that are forbidden due to the properties of the Hamiltonian (2.1). The opposite sign indicates that it can also act as a pumping mechanism.

2.5 Spin-current induced force

Let us inspect different cases of the spin current for the conduction electrons in the topological insulator. Firstly, in the case of partly or completely polarized charge-current, the spin current is non-zero. Secondly, the spin-current is finite in a case of the charge currents that compensate in the average, but with an imbalance in the spin-polarization left. Another situation when the charge current is unpolarized, and in average the spin current is zero. In the last scenario, that holds unless the properties of the material changes. The possible mechanisms are to control material anisotropies by strain, affect by local or external fields, or in general by any of the properties of the environment that would lead in average to electrons spin imbalance. Finally, generating spin inequality is possible by breaking of the symmetry or via different types of junctions [43]. For example, one way is to inject spin-polarized current through the junction with a metal [44]. An alternative way is to thermally induce spin-current as reported for multilayer ferro/non-magnetic system[45].

In the studied case, the coupling of the electrons to the localized spins forming the helicoidal spin texture can substantially influence the surface states of the topological insulator.

On the other hand, the spin torque exerted by the charge carriers acts on the spin structure of the multiferroic chain

$$F_x = -\psi^\dagger \, \frac{d\hat{V}}{dx} \, \psi. \tag{2.24}$$

Under the influence of weak electric field $\vec{\varepsilon}$ in a linear response approximation[16, 17] the total force reads

$$F_x^{tot} = -\frac{ev\mathcal{E}}{2\pi} \, \mathrm{Tr} \left(\hat{F}_x \, \hat{G}^R \, \sigma_x \, \hat{G}^A \right), \tag{2.25}$$

where $\hat{F}_x = gM_0Q \left[\sigma_x \sin(Qx) - \sigma_y \cos(Qx) \right]$ is the force operator and $\hat{G}^{R,A}$ are respectively
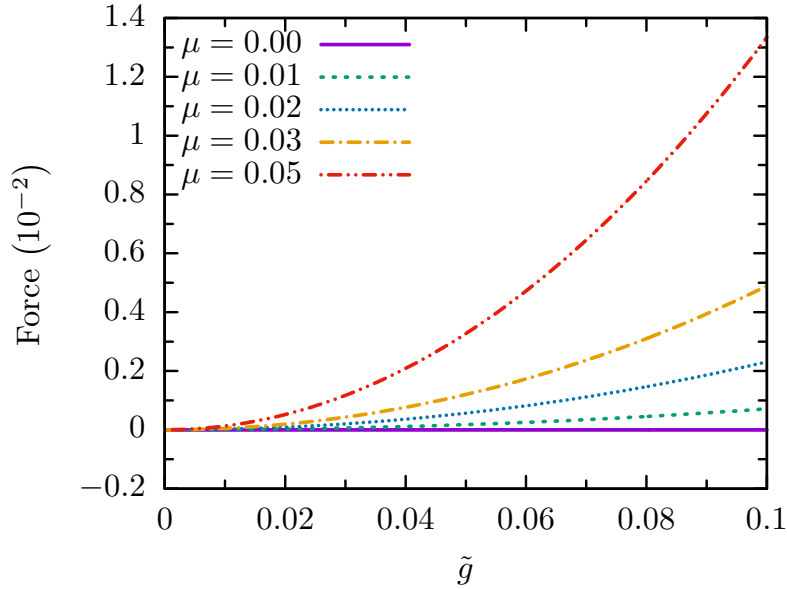
Figure 2.5: Total force as a function of the coupling g for $Q = 0.5$ and $\Gamma = 0.002$.

the retarded and the advanced Green's functions

$$\hat{G}^{R,A} = \left(\mu - \hat{H} \pm i\Gamma \right)^{-1}, \tag{2.26}$$

where Γ is the relaxation decay rate and μ is the chemical potential. The non-zero chemical potential corresponds to an applied bias or any sources of charge density imbalance. Fig. (2.5) shows for $\mu \neq 0$ the total mechanical force on the localized spins texture. For $\mu = 0$ there is no force because in the studied example the generation of the spin torque is due to free carriers that can transfer an angular momentum by the spin-orbit coupling. The strength of the total force also depends on the decay rate.

Summary

The massless Dirac point model was used to calculate the energy dispersion for the surface states of the topological insulator. The symmetry of such system is protecting the Dirac point and thus can resist small perturbations. The weakly interacting magnetic impurities deposited on the surface of the topological insulator might not have an influence on the electronic structure. It is more probable that the spin texture of those impurities is resolved by the properties of the substrate. On another hand, strongly interacting ferromagnetic dopants may open a band gap. In the case of a non-collinear magnetic structure formed on the surface, such as $LiCu_2O_2$ which is a chiral multiferroic system, it acts as a perturbation introducing a small interaction of the conductance electrons with the effective spiral in-plane magnetization field. Therefore, it required an analysis of the spin density dynamics including the interaction with the magnetic impurities which joins the relaxation/pumping term. It was checked that the spin torque generated by the free carriers interacting with magnetic impurities exerts a mechanical force on the localized moments, allowing to control the spin-spin interactions. A non-collinear spin texture deposited on the topological insulator surface does not lift the Dirac point.

Low-dimensional III-V dilute magnetic semiconductors

In the chapter 1, different possibilities for spin dynamics were considered in finite-size structures. The main goal was to analyze possible scenarios to control the specific time of the quantum state transfer between two nodes of the system. In semiconductor physics, a similar behavior is achieved by controlling the spin degree of freedom [46]. The magnetic moments of the carriers in semiconductor system can control the magnetic dynamics of the localized spins, similarly as discussed in the previous chapter.

The primary tool for controlling the magnetic properties is doping with magnetic impurities. Insertion of dopants into pure semiconductors is not of the main interest since they turn back to the undoped pure semiconductors for high enough temperatures. Another class of semiconductors consists of elements which belong to different groups of the periodic table(II-VI, III-V), e.g. Arsenic(As) is an element of Group V and has one extra electron that can be freed and lead to conduction. Gallium(Ga) is an element of Group III and lacks one electron. The GaAs doped with Mn atoms belongs to the class of dilute magnetic semiconductors. The GaAs without Mn does not exhibit ferromagnetism. However, they can be heavily doped with magnetic impurities(mostly Mn) resulting in the most relevant group of dilute magnetic semiconductors, also called semimagnetic semiconductors. Moreover, the Mn atom introduces a hole to the system that acts as a carrier.

This chapter elaborates on the fundaments to the spin-based transport in semiconductors.

As a starting point, a detailed bulk analysis of GaAs is provided, this choice was made due to a strong intrinsic spin-orbit coupling. The origin and the influence of the magnetization field, as well as the strain and the Rashba spin-orbit interaction, are briefly discussed. It is followed by studies towards spintronic devices of magnetically doped low-dimensional GaAs layers, in which at least one of the dimensions leads to a classification between the macroscopic and microscopic system, where the mean free path is comparable to the system's size. In low-dimensional zinc-blende structures, the strengths of the spin-orbit coupling of Dresselhaus and Rashba terms could be comparable. This is important to establish the persistent spin helix state[1]. Therefore, the possibility of engineering one of the couplings strengths is an important task for an ongoing research with applications in spintronic devices(spin-orbitronics).

3.1   Different components of spin-orbit interactions

The spin-orbit coupling originates from the breaking of the symmetry and the influence of the effective field. Under this circumstances the spin has different g-factor than free electron spin.

A magnetic field $\vec{B}$ acts with the Lorentz force $\vec{F} = -e\vec{p} \times \vec{B}/m$ on a charged particle with momentum $\vec{p}$ in addition to the Zeeman energy $\mu_B \vec{\sigma} \cdot \vec{B}$. In following subsections, we will consider a variety of spin, orbital phenomena controlled by a magnetic field.

Origin of spin-orbit coupling Hamiltonian   In an atomic system, the spin-orbit term from a non-relativistic approximation to the Dirac equation [47, 48] reads

$$H_{so} = -\frac{\hbar}{4m_0^2 c^2} \vec{\sigma} \cdot \vec{p} \times (\nabla V_0),$$

(3.1)

where V_0 is the effective Coulomb potential, m_0 is the free electron mass, c is the speed of light. For nearly free electrons the energy gap $2m_0 c^2$ dominate the effect of spin-orbit coupling.

Dresselhaus spin-orbit coupling   In solids, the charge carrier motion is characterized by energy bands $E_{n\vec{k}}$, where n is the band index, and $\vec{k}$ is the wave vector. The spin-orbital

---

[1]The electron spin undergoes a controlled rotation as a function of position [4]

coupling is associated with the lack of space inversion symmetry causing $E_{k\uparrow} \neq E_{k\downarrow}$. The Hamiltonian with the Dresselhaus spin-orbit coupling [49] for a bulk system reveals the lack of inversion symmetry reads

$$H_e = \frac{\hbar^2 k^2}{2m_e} + \frac{1}{2}\Omega_D^\alpha \cdot \sigma, \tag{3.2}$$

where α is $\{x, y, z\}$ component of the cubit term [48]

$$\Omega_D^x = 2\gamma_D k_x(k_y^2 - k_z^2), \quad \gamma_D = 2\eta / \left(3m_{cv}\sqrt{2m_e E_g(1 - \eta/3)}\right), \tag{3.3}$$

and the z-component of the linear Dresselhaus term [4]

$$H_D^z = \beta\left(k_y\sigma^y - k_x\sigma^x\right). \tag{3.4}$$

An important consequence of the Dresselhaus spin-orbital coupling is the anisotropy of the energy bands.

Strain-induced spin-orbit coupling[48] In a semiconductor, such as for instance GaAs, where the lack of inversion symmetry is present, the stress allows controlling the strength of the bulk Dresselhaus coupling and the Rashba spin-orbit coupling in thin layers. Uniform stress causes the same deformation of each unit cell of the crystal. As a result, the crystal will change its shape. Under particular circumstances, the strain tensor can be used to describe the influence of a uniform hydrostatic pressure, deformation caused by temperature or piezoelectric effect. All of those can lead to different phase transitions, and in principle, it is a great tool to adjust the interplay between the effective Dresselhaus and Rashba spin-orbit couplings with significant physical consequences. The spin-helix occur for the comparable strength of the Dresselhaus and Rashba spin-orbit couplings [4].

Rashba spin-orbit coupling Seemingly, the influence of an electric field $\vec{E}$ can be mapped [9] to an effective magnetic field $\vec{B}_{eff} \sim \vec{E} \times \vec{p}/mc^2$, where c is speed of light. Thus, the Zeeman energy with the dependence on the momentum reads $\mu_B\left(\vec{E} \times \vec{p}\right) \cdot \vec{\sigma}/mc^2$.

The Rashba spin-orbit coupling is present in materials with structural inversion asymmetry (e.g. in close vicinity to the interfaces). When the symmetry is broken along z-axis, the effective Bychkov-Rashba spin-orbit coupling reads [50]

$$H_R = \frac{\alpha_R}{\hbar}\left(\vec{z} \times \vec{p}\right) \cdot \vec{\sigma}, \tag{3.5}$$

where α_R is the strength of the coupling and $\vec{\sigma}$ are Pauli matrices for the real spin. The additional pseudospin operators can be introduced that acts on lattice sites. That is relevant for the structure induce spin-orbit coupling [51]. As an example, in a graphene single-layer structure the extrinsic spin-orbit coupling emerge from the interface with the substrate. That allows to affect the spin dynamic, but even the perfect substrate can be a source of disorder in spin-orbit coupling [52].

3.2   Energy bands in pseudopotential framework

The semiconductors have very complicated non-parabolic top valence bands and the simple electron gas models can not be used because of the strong inter-subband coupling. Another way is to assume that the core electrons are tightly-bond that allows for simplified analysis of the core orbitals [53]. In this approach, the valence and conduction electrons are influenced by the effective potential. It can account for the local effects of the exchange and correlations potentials, and it leads to the empirical pseudopotential method which was developed by Phillips et. al. [54, 55, 56]. The pseudopotential Hamiltonian for a crystal has the following form in wave vector space representation [57]

$$\hat{\mathcal{H}} = V_{ij} + \delta_{ij} \frac{\hbar^2}{2m_0} \left| \vec{k} + \vec{K}_i \right|^2 \left(\frac{2\pi}{a_0 \times 10^{-10}} \right)^2, \tag{3.6}$$

where $\vec{K}$ is the reciprocal vector and V_{ij} are offdiagonal elements. After Cohen et. al. [58] the pseudopotential form factors for GaAs in rydbergs unit ($1\ Ry \approx 13.6059$ eV) are
a) symmetric

$$V_3^S = -0.23, \quad V_8^S = 0.01, \quad V_{11}^S = 0.06, \tag{3.7}$$

b) antisymmetric

$$V_3^A = 0.07, \quad V_4^A = 0.05, \quad V_{11}^A = 0.01, \tag{3.8}$$

the coefficients can be found empirically, where S and A are components of the $V_{ij} \to V_{\vec{K}_m}$, that has the following form

$$V_{\vec{K}_m} = V_{\vec{K}_m}^S \cos\left(2\pi \vec{K}_m \cdot \vec{R} \right) + i V_{\vec{K}_m}^A \sin\left(2\pi \vec{K}_m \cdot \vec{R} \right), \tag{3.9}$$

where $\vec{K}_m$ is the integer number, $\vec{R} = a_0\{1/8, 1/8, 1/8\}$, is the vector between Ga and As

Table 3.1: High symmetry points(HSP) for fcc

HSP	in Cartesian Coordinates
Γ	$(0, 0, 0)$
X	$\left(0, \frac{2\pi}{a_0}, 0\right)$
L	$\left(\frac{\pi}{a_0}, \frac{\pi}{a_0}, \frac{\pi}{a_0}\right)$
K=U	$\left(\frac{3\pi}{2a_0}, \frac{3\pi}{2a_0}, 0\right)$
W	$\left(\frac{\pi}{a_0}, \frac{2\pi}{a_0}, 0\right)$

atoms in fcc unit cell of GaAs and a_0 is the corresponding lattice constant. The antisymmetric term enters Eq. (3.9), because of the two different atoms in the unit cell [57].

In this work, the pseudopotential framework is used only as a reference for band structure calculation since it consist of non-unique coefficients V_{ij}. It is difficult to introduce the external fields to the system, strain or spin-orbit interactions and find their influence on the potential V_{ij} without experimental data.
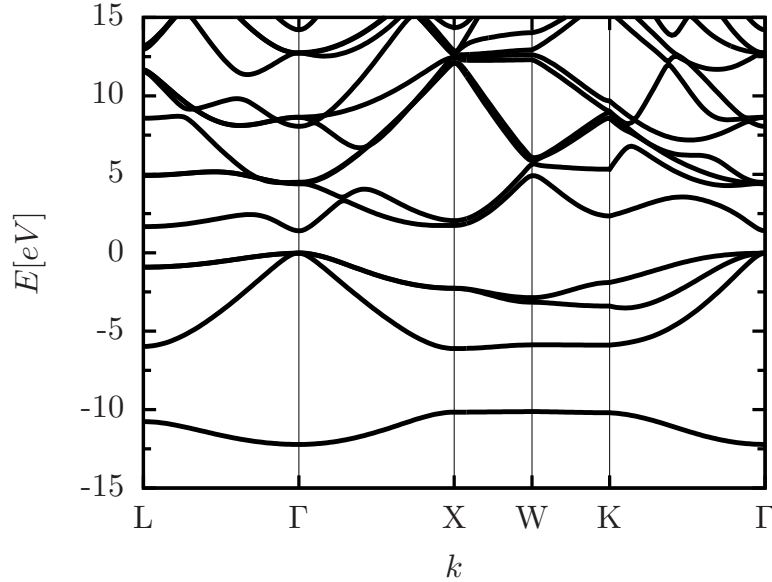
Figure 3.1: The calculated electronic band structure for GaAs is obtained from solving eigenvalue problem of pseudopotential Hamiltonian without spin-orbit interaction. The high symmetry points are explained in the Table 3.1.

3.3   Kane model for top valence bands

Let us consider another method that allows to introduce strain and averaged magnetization to the system. The k·p method similarly like as the pseudopotential method does not require many parameters [47, 60, 61, 62]. We are mainly interested in the top valence band structure in close vicinity to the Γ-point, Table. 3.1. It was shown by Dietl, et. al. [59] that the 6-bands Hamiltonian is the smallest model which describes accurately top valence bands of III-V semiconductor materials.

$$\hat{\mathcal{H}}_{Kane} = \begin{pmatrix} \hat{\mathcal{H}}_v & \hat{\mathcal{H}}_{v,sv} \\ \hat{\mathcal{H}}_{v,sv}^\dagger & \hat{\mathcal{H}}_{sv} \end{pmatrix}, \tag{3.10}$$

where $\hat{\mathcal{H}}_v$ is the Luttinger-Kohn Hamiltonian [63] for Γ_8-valence bands, four-fold states, $\psi_1 = |3/2, 3/2\rangle$, $\psi_4 = |3/2, -3/2\rangle$ heavy-holes bands(HH) and $\psi_2 = |3/2, 1/2\rangle$, $\psi_3 = |3/2, -1/2\rangle$ light-holes bands(LH), $\hat{\mathcal{H}}_{sv}$ is the Hamiltonian for Γ_7, two-fold states, $\psi_5 = |1/2, 1/2\rangle$, $\psi_6 = |1/2, -1/2\rangle$ split-off bands and $\hat{\mathcal{H}}_{v,sv}$ describes the interaction between the top valence-bands with split-off bands. The strength of the spin-orbit interaction is determined by the splitting parameter(split-off band gap) present on the diagonal of $\mathcal{H}_{sv}$. The $\hat{H}_{Kane}$ Hamiltonian in the paper [59] is called $\vec{k} \cdot \vec{p}$ matrix. This Hamiltonian allows to compute the basic energy bands structures and to calculate the effective masses of the holes in the vicinity of the Γ-point.

$$\hat{H}_{Kane} = -E_0 \begin{pmatrix} P+Q & L & M & 0 & iL/\sqrt{2} & -i\sqrt{2}M \\ L^* & P-Q & 0 & M & -i\sqrt{2}Q & i\sqrt{3/2}L \\ M^* & 0 & P-Q & -L & -i\sqrt{3/2}L^* & -i\sqrt{2}Q \\ 0 & M^* & -L^* & P+Q & -i\sqrt{2}M^* & -iL^*/\sqrt{2} \\ -iL^*/\sqrt{2} & i\sqrt{2}Q & i\sqrt{3/2}L & i\sqrt{2}M & P+\Delta & 0 \\ i\sqrt{2}M^* & -i\sqrt{3/2}L^* & i\sqrt{2}Q & iL/\sqrt{2} & 0 & P+\Delta \end{pmatrix} \tag{3.11}$$

where $E_0 = \frac{\hbar^2}{2m_0} \approx 3.81\text{eV Å}^2$, m_0 is the free electron mass, and

$$P = \gamma_1(k_x^2 + k_y^2 + k_z^2),$$
$$Q = \gamma_2(k_x^2 + k_y^2 - 2k_z^2),$$
$$L = -2\sqrt{3}\text{i}\gamma_3(k_x - \text{i}k_y)k_z,$$
$$M = \sqrt{3}\left[\gamma_2(k_x^2 - k_y^2) - 2\text{i}\gamma_3 k_x k_y\right],$$

(3.12)

with the Luttinger parameters $\gamma_1 = 6.85$, $\gamma_2 = 2.1$, $\gamma_3 = 2.9$ and $\Delta = \Delta_{so}/E_0$, $\Delta_{so} = 0.34eV$ is the split-off spin-orbit band gap shown on the Fig. 3.2. The spin-orbit gap Δ_{so} indicates the Pauli spin-orbit interaction (see section 3.1) due to the strong Coulomb potential in atomic core and can be theoretically estimated [47] as

$$\Delta_{so} = \frac{1}{2}\left(1 - f_i\right)\Delta_{Ga} + \frac{1}{2}\left(1 + f_i\right)\Delta_{As},$$

(3.13)

where $f_i = 0.31$ is the semiconductor ionicity [64], $\Delta_{Ga} = 0.18\text{eV}$ and $\Delta_{As} = 0.43\text{eV}$. The coefficients used in our computations are taken from the paper of Dietl et. al. [59]. The
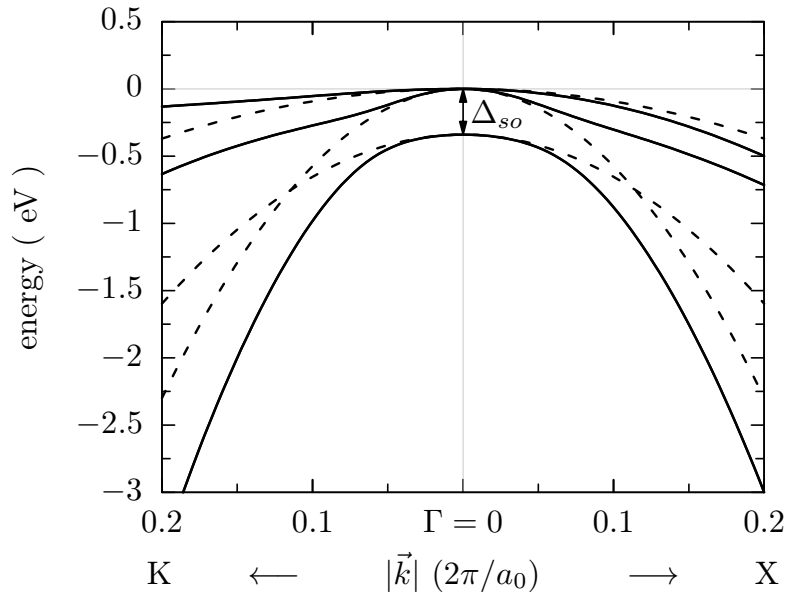
Figure 3.2: The electronic band structure for GaAs obtained by solving the eigenvalue problem of the six-bands Kane model is shown as the solid lines. The dashed lines correspond to bands obtained from the spherical effective mass approximation. The x-axis is scaled to represent the distance from Γ-point.

Hamiltonian 3.11 is written in Bir-Pikus [59, 60] basis

$$\phi_1 = \frac{1}{\sqrt{2}} \left(X + iY \right) \alpha,$$

$$\phi_2 = \frac{i}{\sqrt{6}} \left[\left(X + iY \right) \beta - 2Z\alpha \right],$$

$$\phi_3 = \frac{1}{\sqrt{6}} \left[\left(X - iY \right) \beta + 2Z\beta \right],$$

$$\phi_4 = \frac{i}{\sqrt{2}} \left(X - iY \right) \beta,$$

$$\phi_5 = \frac{1}{\sqrt{3}} \left[\left(X + iY \right) \beta + Z\alpha \right],$$

$$\phi_6 = \frac{i}{\sqrt{3}} \left[- \left(X - iY \right) \alpha + Z\beta \right],$$

(3.14)

where $\alpha^T = (1,0)$, $\beta^T = (0,1)$ and the superpositions of X, Y, Z can be expressed in term of the spherical harmonic Y_l^m with angular momentum $l = 1$. Solving the characteristic equation $\det \left(H(\vec{k}) - I\lambda \right) = 0$ for different wave-vector $\vec{k}$ the non-parabolic band structure is obtained and presented in Fig. 3.2. Fitting with parabolic relation in close vicinity of the Γ-point towards the X-direction allows to compute the effective mass for holes in GaAs, with $m_{HH} = 0.51m_0$, $m_{LH} = 0.082m_0$, $m_{SO} = 0.15m_0$, (taken from [65]). As can be seen from Fig. 3.2 the non-parabolic and anisotropic character of the band structure requires the introduction of effective masses for all bands depending on the crystal orientation. The disproportion of Luttinger parameters $\gamma_2 \neq \gamma_3$ characterize the anisotropy strength of valence bands. In the next sections, the term μ chemical potential appears quite often in the sense of energy above which all states in the valence bands are filled with holes, or it is named as an isoenergy when this energy surface is discussed.

Matrix form of orbital angular momentum operators

Let us define the general form of the orbital angular momentum operators in spherical coordinates

$$L_\alpha = \int\limits_0^\pi \sin(\theta) \int\limits_0^{2\pi} \phi_i^* \cdot L'_\alpha \cdot \phi_j \, d\varphi \, d\theta,$$

(3.15)

where L'_α reads [66]

$$L'_x = i\hbar \left(\sin(\varphi) \frac{\partial}{\partial \theta} + \cot(\theta) \cos(\varphi) \frac{\partial}{\partial \varphi} \right),$$

$$L'_y = i\hbar \left(-\cos(\varphi) \frac{\partial}{\partial \theta} + \cot(\theta) \sin(\varphi) \frac{\partial}{\partial \varphi} \right), \tag{3.16}$$

$$L'_z = -i\hbar \frac{\partial}{\partial \varphi}.$$

Thus the x-component of the orbital angular momentum operator in the matrix form is

$$L_x = \hbar \begin{pmatrix} 0 & \frac{i}{\sqrt{3}} & 0 & 0 & -\frac{1}{\sqrt{6}} & 0 \\ -\frac{i}{\sqrt{3}} & 0 & \frac{2}{3}i & 0 & 0 & \frac{1}{3\sqrt{2}} \\ 0 & -\frac{2}{3}i & 0 & \frac{i}{\sqrt{3}} & -\frac{1}{3\sqrt{2}} & 0 \\ 0 & 0 & -\frac{i}{\sqrt{3}} & 0 & 0 & \frac{1}{\sqrt{6}} \\ -\frac{1}{\sqrt{6}} & 0 & -\frac{1}{3\sqrt{2}} & 0 & 0 & -\frac{2}{3}i \\ 0 & \frac{1}{3\sqrt{2}} & 0 & \frac{1}{\sqrt{6}} & \frac{2}{3}i & 0 \end{pmatrix}, \tag{3.17}$$

then the y-component of the operator is

$$L_y = \hbar \begin{pmatrix} 0 & \frac{1}{\sqrt{3}} & 0 & 0 & \frac{i}{\sqrt{6}} & 0 \\ \frac{1}{\sqrt{3}} & 0 & \frac{2}{3} & 0 & 0 & -\frac{i}{3\sqrt{2}} \\ 0 & \frac{2}{3} & 0 & \frac{1}{\sqrt{3}} & -\frac{i}{3\sqrt{2}} & 0 \\ 0 & 0 & \frac{1}{\sqrt{3}} & 0 & 0 & \frac{i}{\sqrt{6}} \\ -\frac{i}{\sqrt{6}} & 0 & \frac{i}{3\sqrt{2}} & 0 & 0 & -\frac{2}{3} \\ 0 & \frac{i}{3\sqrt{2}} & 0 & -\frac{i}{\sqrt{6}} & -\frac{2}{3} & 0 \end{pmatrix}, \tag{3.18}$$

and the z-component is

$$
L_z = \hbar
\begin{pmatrix}
1 & 0 & 0 & 0 & 0 & 0 \\
0 & \frac{1}{3} & 0 & 0 & -\frac{\sqrt{2}}{3}i & 0 \\
0 & 0 & -\frac{1}{3} & 0 & 0 & \frac{\sqrt{2}}{3}i \\
0 & 0 & 0 & -1 & 0 & 0 \\
0 & \frac{\sqrt{2}}{3}i & 0 & 0 & \frac{2}{3} & 0 \\
0 & 0 & -\frac{\sqrt{2}}{3}i & 0 & 0 & -\frac{2}{3}
\end{pmatrix} .
\tag{3.19}
$$

The matrix representation of the orbital angular momentum operators in the basis of the Hamiltonian is helpful in considering different spin-orbit interaction terms.

Fermi surface/energy, isoenergy

At absolute zero temperature, the Fermi energy is the highest occupied state[38]. In the following sections from the calculation at $T = 0K$ depending on the chemical potential different isoenergies are analyzed.
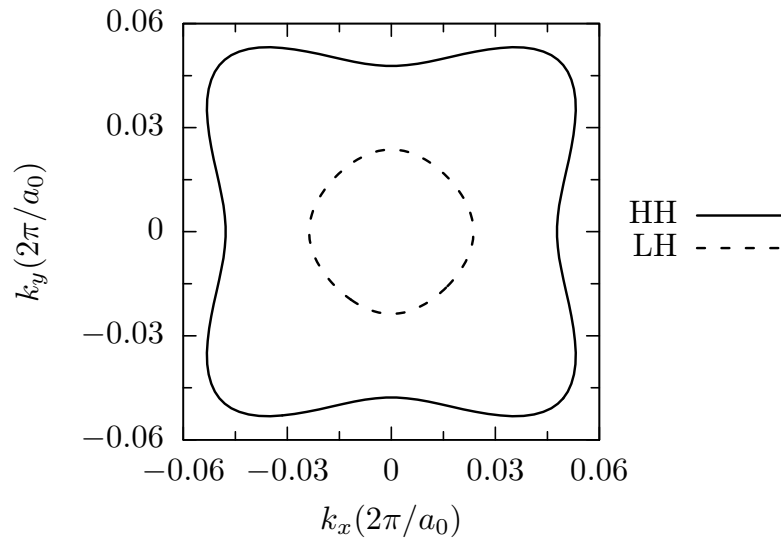

Figure 3.3: Isoenergy surface for chemical potential $\mu = -28.5$meV, where $\vec{k}$ was scaled with $2\pi/a_0$ factor and $a_0 = 5.65$ is the GaAs lattice constant.

The isoenergy surface for two-fold bands of heavy holes and two-fold bands of light-holes at $\mu = -28.5$meV are shown in Fig. 3.3. Since the local effective mass for HH, is bigger than for LH, the outer isoenergy surface is for HH and the inner surface is for LH. Due to $\mu > -\Delta_{so}$ the SO bands are entirely filled with electrons, and their surface is not present at this chemical potential. It is possible to compute the hole concentrations and the total energy of the system from such surfaces and volumes in the three-dimensional case.

Hole concentration

The hole concentration in a semiconductor depends on various internal as well as external factors. Mainly, the chemical potential has a direct influence on the hole concentration. On the other side, the dependency of the energy bands on strain and magnetization provides a tool to study a wide range of different types of anisotropies. The hole concentration contribution follows from an integration over the first Brillouin zone(1BZ) [67]

$$p = \frac{1}{(2\pi)^3} \sum_n \int\limits_{1BZ} d\vec{k}\, \theta\left(\varepsilon_{n\vec{k}} - \mu\right), \qquad (3.20)$$

where $\theta(x)$ is the Heaviside function and the integration domain depends on the lattice constant. The fully occupied bands with holes, for $a_0 = 5.65$Å give the maximum of the hole concentration $p_{\max} = 1.33 \times 10^{23}$ states/cm^3. The hole concentration for the chemical potential $\mu = -28.5$meV in GaAs is $p = 1.27 \times 10^{19}$cm^{-3}, see Fig. 3.3. The hole concentration for the shown two-dimensional layer is $p_{xy} = 7.54 \times 10^{12}$cm^{-2}. The density of states can be calculated by taking the derivative of hole concentration with respect to the chemical potential $\frac{dp}{d\mu}$.

Due to the specific boundaries of the integration domain, the different integration schemes could be used to approximate the hole concentration. Especially in 3-dimensional integration, the fast convergence of the algorithm plays a crucial role. At first prerequisite, computations are performed to reduce integration domain if possible. With this step for almost all methods, the simplest integration schemes are Monte Carlo and extended trapezoidal rule. The Monte Carlo method gives the rough estimation. However, it is not possible to use it for analyzing the influence of small perturbations, weak fields, and deformations. The extended trapezoidal rule gives much better results, but it is computationally demanding to handle multidimen-
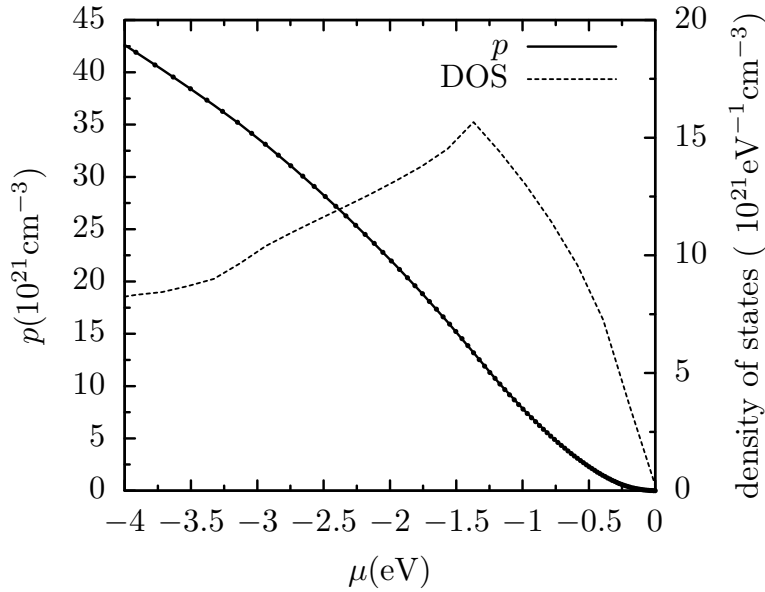
Figure 3.4: The hole concentration and corresponding density of states as a function of the chemical potential.

sional integrations. The grid of extended trapezoidal rule can be adaptively reduced, and this idea will be further used in developing better performing algorithm. If the uniform grid is used with this method, the convergence might be not reached due to round-off errors. In a case of spherical integration, an algorithm with the Fibonacci series [68] works very well for small hole concentrations where only the HH bands contribute. This algorithm has an advantage in point sampling in comparison to the standard spherical integration scheme. In general, polar and spherical integrations are suitable for smooth functions. In the next sections, many cases of sharp edges between the nearly crossing(anti-crossing) bands lead to slower convergence of such algorithms. Also, that is the reason why most of the numerical libraries for integration are not useful even in one-dimension, for instance, QUADPACK. Depending on the complexity of those edges it is sometimes possible to achieve sufficient precision with reasonable computation time. In mesh generating subroutine, little smoothing of the edges can be applied for obtaining a better quality mesh that does not omit parts of the edges. The final integration is taken over triangles in 2D integrations and can be done over tetrahedrons in 3D integration scheme. In the final step, the triangles can be additionally categorized depending on the groups to which belongs(inside of the volume, outside, and to

the edges). The procedure of mesh generation can be stopped after the ratio between the area of edge triangles is much smaller than the area of inside triangles. More technical details about the used weights are described in the appendix A.

Total energy

In general, the description of the system's total energy can be very complex. As it is presented in further sections, the analysis of the total energy variation on two constraints is considered. Firstly, a *constant hole concentration* which is a conventional constraint for bulk systems, the hole concentration could be determined by the amount of Mn dopants. Secondly, *constant chemical potential* which is more appropriate in thin layers.

The total energy of the hole system may be described as follows [67]

$$\mathcal{E} = \frac{1}{(2\pi)^3} \sum_n \int_{1BZ} d\vec{k} \, \varepsilon_{n\vec{k}} \, \theta \left(\varepsilon_{n\vec{k}} - \mu \right), \tag{3.21}$$

which with Eq. (3.20) allow to numerically determine the dependency on the hole concen-
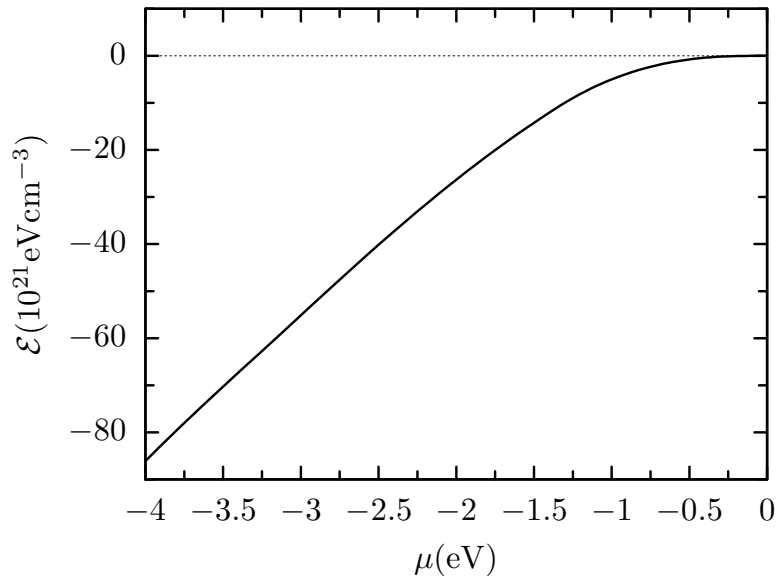
Figure 3.5: The total energy of the hole system as a function of chemical potential.

tration which requires solving a parametric integration to find the chemical potential μ for a given hole concentration p. In the integrand, an additional term can be included for the total energy of the electrons $\varepsilon_{n\vec{k}}$. In most considered cases this will lead only to a linear shift of
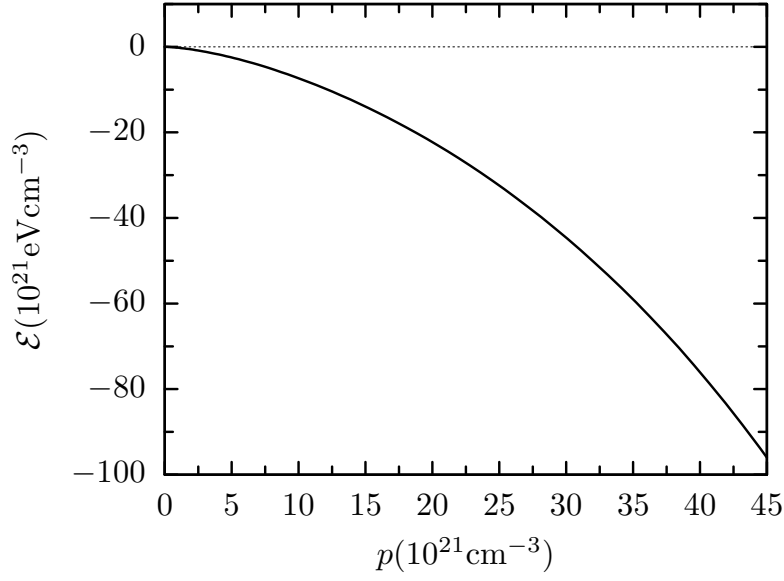
Figure 3.6: The total energy of the hole system as a function of hole concentration.

the results. The total energy of the system is

$$\mathcal{E} = -\frac{1}{(2\pi)^3} \sum_n \int\limits_{1BZ} d\vec{k}\, \varepsilon_{n\vec{k}} \left[1 - \theta\left(\varepsilon_{n\vec{k}} - \mu\right)\right].$$

(3.22)

From Eqs. (3.20, 3.21) the dependencies on chemical potential and the hole concentration are present in Figs. 3.5, 3.6. Since, all of the GaAs valence bands are negative $\left(\varepsilon_{n\vec{k}} < 0\right)$ using Eq. (3.21) the total energy of the hole system is always negative. In further sections, those results are used to describe the variation of the total energy $(\mathcal{E} - \mathcal{E}_0)$ for a better understanding of the influence of strain or magnetization on the properties of the system.

3.4 Strain-induced effects

The strain can be seen as a result of the interaction with a substrate on which semiconductor is placed, lattice mismatch, external forces or pressure, dislocations, cracks, vacancies, atoms displacements and others. Putting in a dopant is another way. In general, the strain term in the Hamiltonian can be derived using the mapping recipe for Luttinger-Kohn Hamiltonian $\rightarrow$

$\hat{H}_{Kane}$	P	Q	L	M	$\hat{H}_\varepsilon$	P_ε	Q_ε	L_ε	M_ε
γ_1	-				a_v	+			
γ_2		-		-	b		+		+
γ_3			+	+	d			-	-

Table 3.2: Check of signs in Luttinger-Kohn → Bir-Pikus strain Hamiltonian recipe.

Bir-Pikus type of strain Hamiltonian [69]

$$
\begin{cases}
-\frac{\hbar^2}{2m_0}\gamma_1 & \to \quad a_v, \\[2mm]
-\frac{\hbar^2}{2m_0}\gamma_2 & \to \quad \frac{b}{2}, \\[2mm]
-\frac{\hbar^2}{2m_0}\gamma_3 & \to \quad \frac{d}{2\sqrt{3}},
\end{cases}
\tag{3.23}
$$

where $a_v = 1.16\text{eV}$, $b = -1.7\text{eV}$, $d = -4.55\text{eV}$, are deformation potentials for GaAs [70] and k_x, k_y, k_z are replaced by the corresponding components of the strain tensor u

$$
u = \begin{pmatrix}
u_{xx} & u_{xy} & u_{xz} \\
\cdot & u_{yy} & u_{yz} \\
\cdot & \cdot & u_{zz}
\end{pmatrix}.
\tag{3.24}
$$

The final $\mathcal{H}_\varepsilon$ strain Hamiltonian with use of the signs Table 3.2, denotes[60]

$$
\hat{H}_\varepsilon = \begin{pmatrix}
P_\varepsilon + Q_\varepsilon & L_\varepsilon & M_\varepsilon & 0 & iL_\varepsilon/\sqrt{2} & -i\sqrt{2}M_\varepsilon \\
L_\varepsilon^* & P_\varepsilon - Q_\varepsilon & 0 & M_\varepsilon & -i\sqrt{2}Q_\varepsilon & i\sqrt{3/2}L_\varepsilon \\
M_\varepsilon^* & 0 & P_\varepsilon - Q_\varepsilon & -L_\varepsilon & -i\sqrt{3/2}L_\varepsilon^* & -i\sqrt{2}Q_\varepsilon \\
0 & M_\varepsilon^* & -L_\varepsilon^* & P_\varepsilon + Q_\varepsilon & -i\sqrt{2}M_\varepsilon^* & -iL_\varepsilon^*/\sqrt{2} \\
-iL_\varepsilon^*/\sqrt{2} & i\sqrt{2}Q_\varepsilon & i\sqrt{3/2}L_\varepsilon & i\sqrt{2}M_\varepsilon & P_\varepsilon & 0 \\
i\sqrt{2}M_\varepsilon^* & -i\sqrt{3/2}L_\varepsilon^* & i\sqrt{2}Q_\varepsilon & iL_\varepsilon/\sqrt{2} & 0 & P_\varepsilon
\end{pmatrix},
\tag{3.25}
$$

where the corresponding parameters are

$$P_\varepsilon = a_v(u_{xx} + u_{yy} + u_{zz}), \tag{3.26}$$

$$Q_\varepsilon = \frac{b}{2}(u_{xx} + u_{yy} - 2u_{zz}), \tag{3.27}$$

$$L_\varepsilon = -\mathrm{i}d(u_{xz} - \mathrm{i}u_{yz}), \tag{3.28}$$

$$M_\varepsilon = \frac{\sqrt{3}}{2}b(u_{xx} - u_{yy}) - \mathrm{i}du_{xy}. \tag{3.29}$$

Due to terms on diagonal of the Hamiltonian (3.25) we can easily see that the strain will lift the degeneration of the states of the heavy holes and the light holes bands.

Band structure

Any type of uni/bi-axial strain decreases the band gap of a semiconductor between the lowest conduction and the top valence band. The sign indicates a compressive and a tensile type of strain, see Figs. 3.7, 3.8. In the case of a tensile type of strain $(u_{xx} > 0)$ the two-folded split-
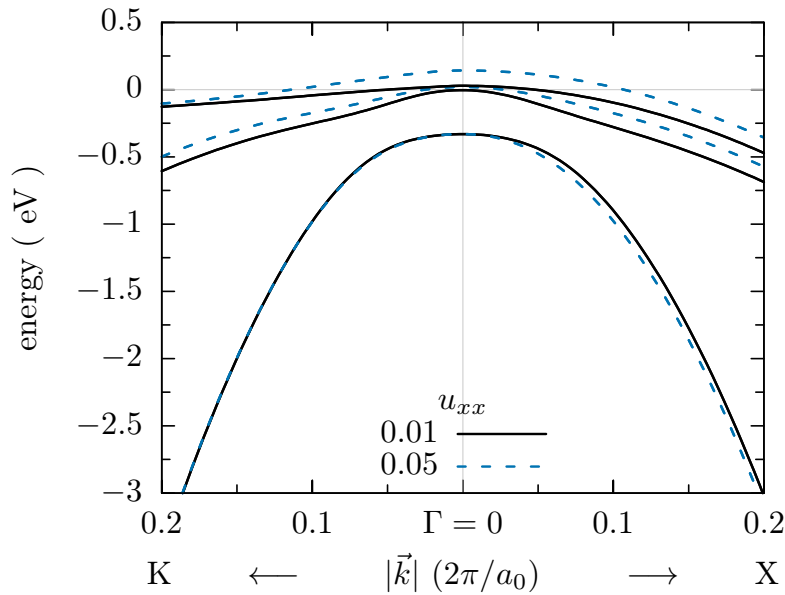
Figure 3.7: The influence of strain on the energy dispersion with $u_{xx} = 0.01$ and $u_{xx} = 0.05$ and the deformation potentials for GaAs.

off bands are the least affected. The other four bands, except a shift towards the conduction bands, are essentially changed in the vicinity of Γ-point.   Due to the compressive type of strain $(u_{xx} < 0)$ the top valence bands are not only split into two-folded heavy-hole and light-
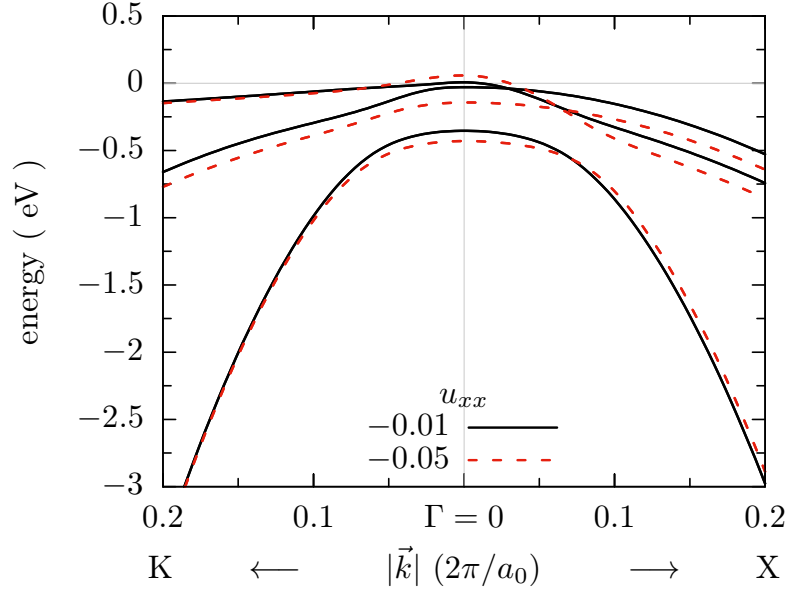
Figure 3.8: The influence of strain on the energy dispersion with $u_{xx} = -0.01$ and $u_{xx} = -0.05$ and the deformation potentials for GaAs.

hole bands, but also their crossing can occur depending on the crystallographic orientation. In Fig. 3.8, the degeneracy of the bands appears close to $k_x = 0.03\frac{2\pi}{a_0}$ and $k_x = 0.06\frac{2\pi}{a_0}$ depending on the strength of the strain. This indicates that the degeneracy of the top valence bands is displaced from the Γ-point due to the compressive uni-axial strain while a tensile deformation lifts the degeneracy.

This discrepancy is directly connected to the asymmetric character of the top valence bands splitting as a function of the strain strength, Fig. 3.9. Biaxial strain leads to symmetric splitting at the Γ-point for compressive or tensile deformation. For a weak strain, the split-off gap Δ_{so} can be decreased. Due to symmetry, the u_{xx}, u_{yy} and u_{zz} types of strain are equivalent and they have the same influence on the Γ-point presented in Fig. 3.9. Similarly, the Fig. 3.10 shows an influence of corresponding equivalent u_{xy}, u_{xz} and u_{yz} types of strain. Section 3.5 shows the magnetic anisotropy depends on applied deformation.
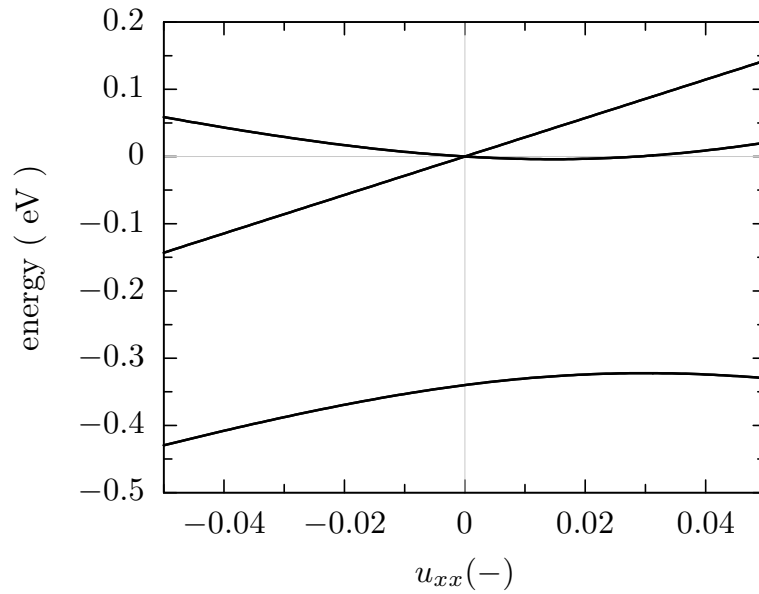
Figure 3.9: Top valence bands splitting with uni-axial strain at Γ-point.
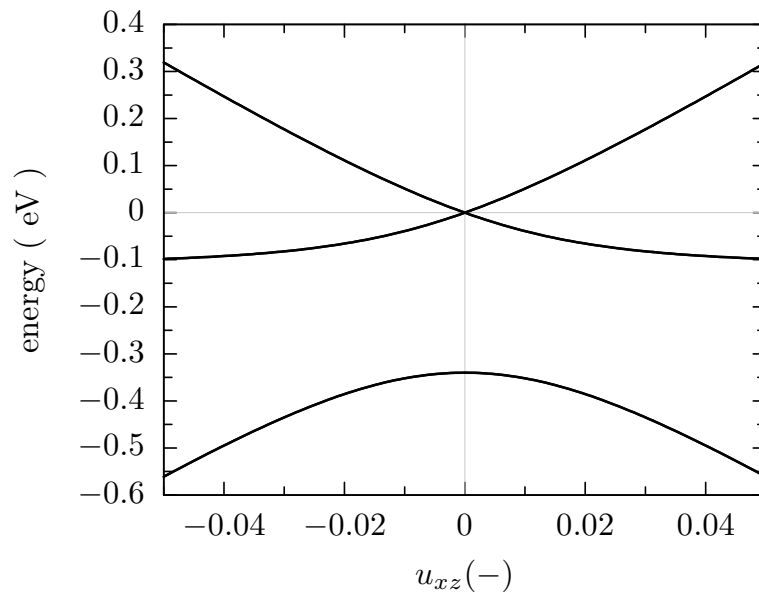
Figure 3.10: Top valence bands splitting with bi-axial strain at Γ-point.

Isoenergy surface

In Fig. 3.11, the uni-axial strain u_{xx} stretches the isoenergy surface along the x-axis and squeezes in all the other directions increasing the anisotropy of the band structure and the hole concentration with respect to the unstrained system (for $u_{xx} = 0.01$ at $\mu = -28.5$meV,

$p = 2.31 \times 10^{19}\text{cm}^{-3}$ and $p_{xy} = 1.13 \times 10^{13}\text{cm}^{-3}$). Within this model, it is possible to include
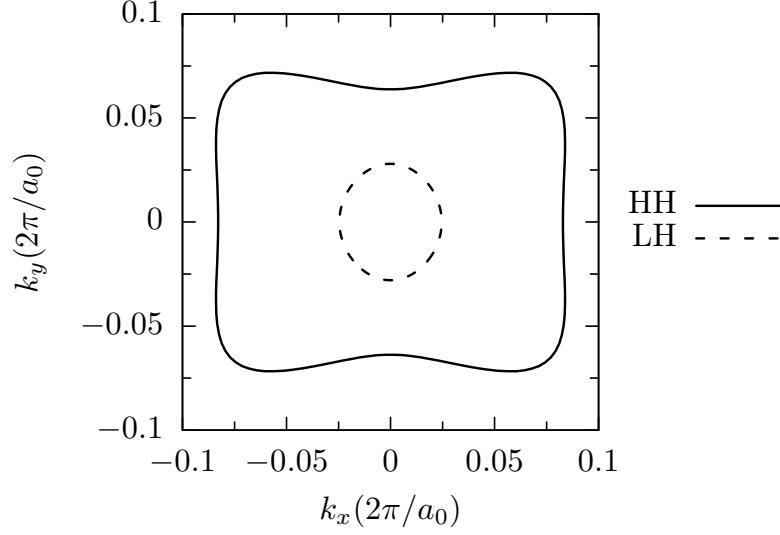
Figure 3.11: The uni-axial strain influence on the isoenergy surface at $\mu = -28.5\text{meV}$ with a tensile strain $u_{xx} = 0.02$ will result in hole concentration $p = 3.84 \times 10^{19}\text{cm}^{-3}$ and $p_{xy} = 1.55 \times 10^{13}\text{cm}^{-3}$.

any small deformation effect related to linear elasticity. Realistically, to include the effect of strain induced by a lattice mismatch with the substrate material or small distortion, the strain with the three non-zero tensor values are often in use

$$u_{xx} = u_{yy} = \Delta a / a_0, \tag{3.30}$$

where Δa is the change in the lattice constant due to the applied strain and $u_{zz} = -2u_{xx}c_{12}/c_{11}$, where $c_{12}/c_{11} = 0.453$ is the ratio of the elastic moduli [71]. With these relations assuming 2% decrease in the lattice constant, $u_{xx} = u_{yy} = -0.02$ and $u_{zz} = 0.018$ in strained GaAs semiconductor, the top valence band is shifted by 39meV towards the conduction bands.

Total energy

Due to strain, the hole concentration is increased for a fixed chemical potential. In Fig. 3.12, as a result of strained material non-zero total energy appear for the chemical potential $\mu = 0$. Because the top valence bands are not at $\mu = 0\text{eV}$, the total energy can change the sign. It is related to the choice which was made for the integration constant that shifts the results.
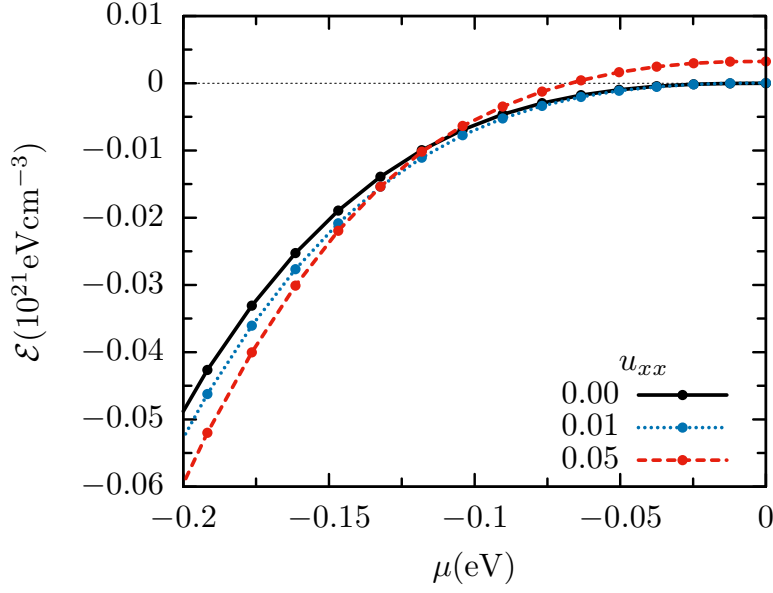
Figure 3.12: The influence of the uni-axial strain on the total energy as a function of the chemical potential.

The total energy is zero for fully occupied valence bands by electrons. Meaning, there are no allowed states for holes above the chemical potential corresponding to the energy level of the top valence band at the Γ-point. In the latter case for chemical potential about $\mu \sim -70\text{meV}$ with $u_{xx} = 0.05$, the total energy is equal to zero, while the hole concentration remains non-zero. It is clear that the hole concentration cannot be negative. The only possibility of the change of the sign can happen for the energy level when the top valence band has an energy level above zero $\varepsilon_{n\vec{k}} > 0$. This can be included by $\mu_{\Gamma}\theta\left(\varepsilon_{n\vec{k}} - \mu\right)$ term in Eq. (3.21), where μ_{Γ} is the highest occupied state by the hole at the Γ-point. Note, for different strengths of the deformation potential at a fixed chemical potential the hole concentration is not equal. In Fig. 3.13 is shown that the non-trivial hole concentration for which the total energy is zero is $p = 1.8 \times 10^{20}\text{cm}^{-3}$ for a uni-axial strain $u_{xx} = 0.05$. Finally, from this figure it can be understood, that in the case of bulk systems the magnitude of the total energy is always smaller for uni-axially u_{xx} strained systems. However, another possibility exists for thin layers where the thickness is much smaller for one of the dimension. In such systems, the constraint on the constant chemical potential is more important.
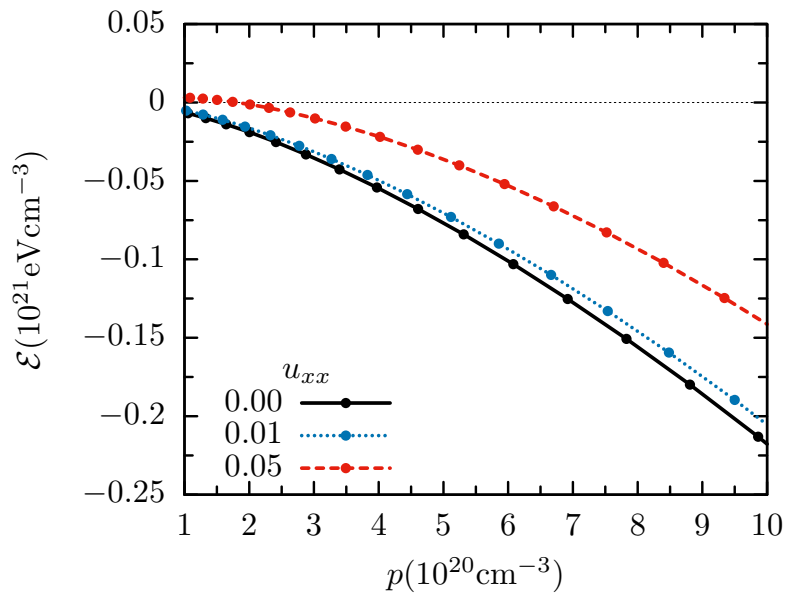
Figure 3.13: The total energy dependency as a function of hole concentration with uni-axial strain.

3.5 Magnetization anisotropy

The semiconductor GaAs crystallizes in (2x fcc, Fig. 3.14) zinc-blende structures[2] which lacks inversion center and does not demonstrate any magnetic properties. The magnetic properties
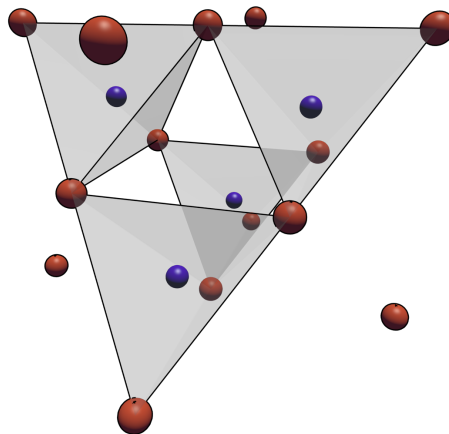
Figure 3.14: Schematic representation of the double fcc elementary cell without an inversion center.

of $Ga_{1-x}Mn_xAs$ dilute magnetic semiconductor are acquired from Mn^{2+} ion with the localized

---

[2]Space group (216), Herman-Mauguin (F-43m), Hall (F -4 2 3), Schoenflies (T_d^2)

spin $S = \frac{5}{2}$ and a magnetic moment of $5\mu_B$ introducing a hole by attracting an electron from the GaAs compound [72]. Their ferromagnetic ordering is mediated by free or nearly free holes in the valence bands[8, 59]. With increasing the number of Mn ions, the magnetization can reach a maximum and then if the concentration is too high the magnetization decreases in an average. Likewise, many deformation mechanisms can have the substantial influence on the magnetic anisotropy [73] as inferred by including strain tensor from section 3.4.

To describe correctly the complex structure of top valence bands of semiconductor the model should be extended by a term describing band splitting with respect to spin. In this section, a contribution from the hole-mediated p-d exchange coupling between the Mn ions treated within the virtual-crystal and the molecular-field approximations[8] is considered and further referred to as spatially uniform magnetization

$$\hat{H}_{pd} = \frac{\beta \vec{s} \cdot \vec{M}}{g\mu_B}, \tag{3.31}$$

where the magnetization axis $\vec{M}$ can be oriented in any direction related to the average of the total net magnetization. The Hamiltonian written in Bir-Pikus basis Eq. (3.14) has the following form[59]

$$\hat{H}_m = B_G \begin{pmatrix} 3n_z & i\sqrt{3}n_- & 0 & 0 & \sqrt{6}n_- & 0 \\ -i\sqrt{3}n_+ & n_z & 2in_- & 0 & i2\sqrt{2}n_z & -\sqrt{2}n_- \\ 0 & -2in_+ & -n_z & i\sqrt{3}n_- & \sqrt{2}n_+ & -i2\sqrt{2}n_z \\ 0 & 0 & -i\sqrt{3}n_+ & -3n_z & 0 & -\sqrt{6}n_+ \\ \sqrt{6}n_+ & -i2\sqrt{2}n_z & \sqrt{2}n_- & 0 & -n_z & in_- \\ 0 & -\sqrt{2}n_+ & i2\sqrt{2}n_z & -\sqrt{6}n_- & -in_+ & n_z \end{pmatrix}, \tag{3.32}$$

where $B_G = \frac{\beta N_0 M_0}{6g\mu_B}$ is the spin splitting parameter, $g = 2$ and $\beta N_0 = (-1.2 \pm 0.2)$eV for GaAs, $\mu_B = \frac{e\hbar}{2m_0}$ is the Bohr magneton

$$n_z = \frac{M_z}{M_0}, \quad n_\pm = \frac{M_x \pm iM_y}{M_0}, \tag{3.33}$$

$\vec{n}$ is the unit vector of the magnetization direction. GaAs with Mn is preferably ferromagnetic. The holes get polarized in the close vicinity of the Mn atom when they hop to neighboring

Mn atom they exert a small spin torque, and collective excitation can assist in changes of the polarization of the Mn localized spins.

Matrix form of spin operators

Let us first consider the spin operators for the holes with the Hamiltonian written in the Bir-Pikus basis (3.14). The general form of the spin operators in spherical coordinates can be written in the following form

$$S_\alpha = \int\limits_0^\pi \sin(\theta) \int\limits_0^{2\pi} \phi_i^* \cdot \sigma_\alpha \cdot \phi_j \; d\varphi \; d\theta, \tag{3.34}$$

where $\alpha = \{x, y, z\}$ is the spin component, the indices $i, j = 1..N$ and σ_α denotes the Pauli matrices. The x-component of the spin operator in matrix form reads

$$S_x = \begin{pmatrix} 0 & \frac{i}{\sqrt{3}} & 0 & 0 & \sqrt{\frac{2}{3}} & 0 \\ -\frac{i}{\sqrt{3}} & 0 & \frac{2}{3}i & 0 & 0 & -\frac{\sqrt{2}}{3} \\ 0 & -\frac{2}{3}i & 0 & \frac{i}{\sqrt{3}} & \frac{\sqrt{2}}{3} & 0 \\ 0 & 0 & -\frac{i}{\sqrt{3}} & 0 & 0 & -\sqrt{\frac{2}{3}} \\ \sqrt{\frac{2}{3}} & 0 & \frac{\sqrt{2}}{3} & 0 & 0 & \frac{i}{3} \\ 0 & -\frac{\sqrt{2}}{3} & 0 & -\sqrt{\frac{2}{3}} & -\frac{i}{3} & 0 \end{pmatrix}, \tag{3.35}$$

then y-component of the spin-operator

$$S_y = \begin{pmatrix} 0 & \frac{1}{\sqrt{3}} & 0 & 0 & -\sqrt{\frac{2}{3}}i & 0 \\ \frac{1}{\sqrt{3}} & 0 & \frac{2}{3} & 0 & 0 & \frac{\sqrt{2}}{3}i \\ 0 & \frac{2}{3} & 0 & \frac{1}{\sqrt{3}} & \frac{\sqrt{2}}{3}i & 0 \\ 0 & 0 & \frac{1}{\sqrt{3}} & 0 & 0 & -\sqrt{\frac{2}{3}}i \\ \sqrt{\frac{2}{3}}i & 0 & -\frac{\sqrt{2}}{3}i & 0 & 0 & \frac{1}{3} \\ 0 & -\frac{\sqrt{2}}{3}i & 0 & \sqrt{\frac{2}{3}}i & \frac{1}{3} & 0 \end{pmatrix}, \tag{3.36}$$

and similarly the z-component of the spin-operator

$$
S_z = \begin{pmatrix}
1 & 0 & 0 & 0 & 0 & 0 \\
0 & \frac{1}{3} & 0 & 0 & \frac{2\sqrt{2}}{3}i & 0 \\
0 & 0 & -\frac{1}{3} & 0 & 0 & -\frac{2\sqrt{2}}{3}i \\
0 & 0 & 0 & -1 & 0 & 0 \\
0 & -\frac{2\sqrt{2}}{3}i & 0 & 0 & -\frac{1}{3} & 0 \\
0 & 0 & \frac{2\sqrt{2}}{3}i & 0 & 0 & \frac{1}{3}
\end{pmatrix}.
\tag{3.37}
$$

This representation is further used in the analysis of the spin-polarization.

Mean $\langle S \rangle$

The spin-polarized current of free charges can drive the magnetic dynamics. Therefore, it is of interest to control a polarization direction of the current. The hole spin projection $\langle S_z \rangle$ when the magnetization of the localized spins is along the x-axis is shown on Figs. 3.15, 3.16. For this calculation very small magnetization B_G was applied to split the degenerated
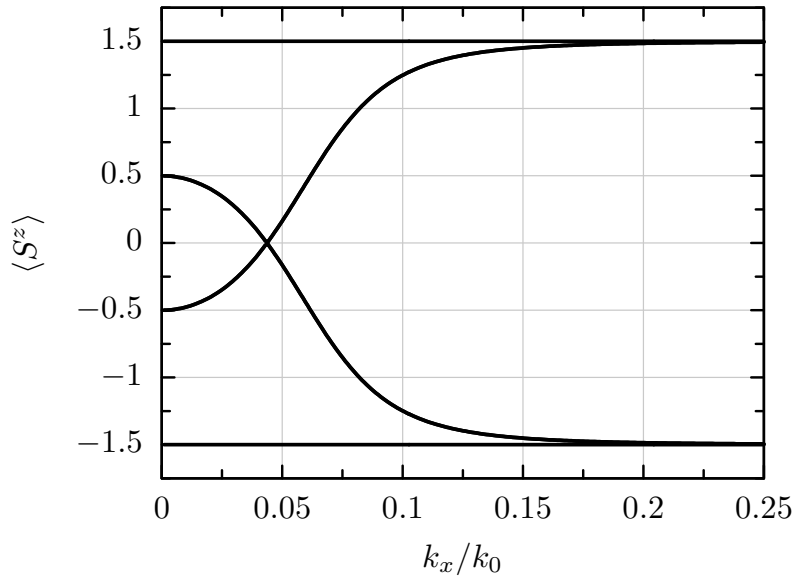
Figure 3.15: The z-component of the hole spin polarization

eigenstates of the Hamiltonian. That is of particular importance in the close vicinity of the

Γ-point. The non-zero net magnetization leads to unfolding all the eigenstates, Fig. 3.16. As
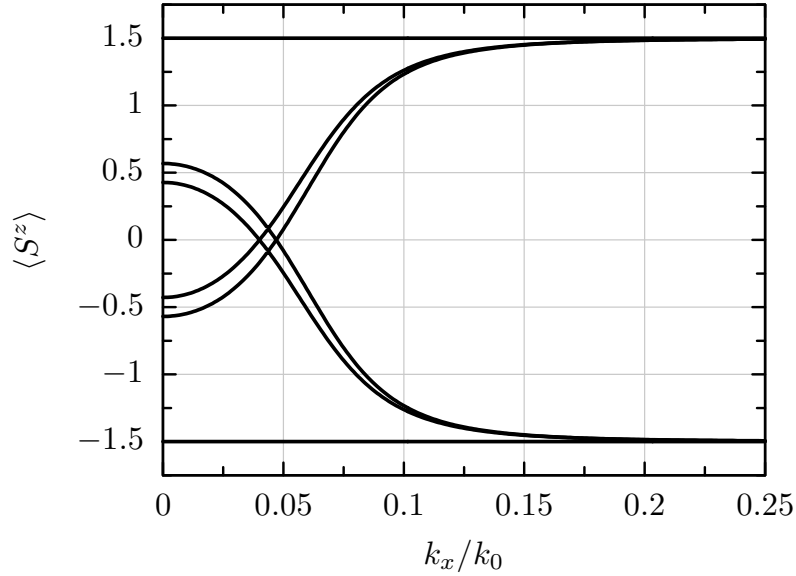
Figure 3.16: The z-component of the hole spin polarization with magnetization $B_G = 3$meV.

a result of the strong inter-subband coupling, any changes of the electronic band structure has an influence on the spin-polarization of holes..

Band structure

The magnetization leads to splitting all of the top valence bands at Γ-point. In comparison to an uni-axial strain u_{xx}, Fig. 3.7 the magnetization affects the eigenstates differently with opposite spins while the strain makes no such distinction. As apparent from Fig. 3.17 there is no clear distinction between the heavy hole and light hole bands. In the case of a magnetization in x-axis, for X $\to \Gamma \to$ K path the top two bands belongs to heavy holes and they interchange the ordering with light-holes through mixed-states in the vicinity of Γ-point to first and fourth top bands. Since the ordering might be changed in further part of the thesis referring to heavy holes is not meant by eigenstate but by the top two eigenvalues. As follows, Fig. 3.18 demonstrates the influence of the magnetization on the top valence bands at Γ-point, where for large B_G a linear dependency is found. The decrease of the energy band gaps between the valence bands and the conduction bands as well as the Δ_{so} split-off band gap is also significant for the transport properties of the semiconductor. In the absence
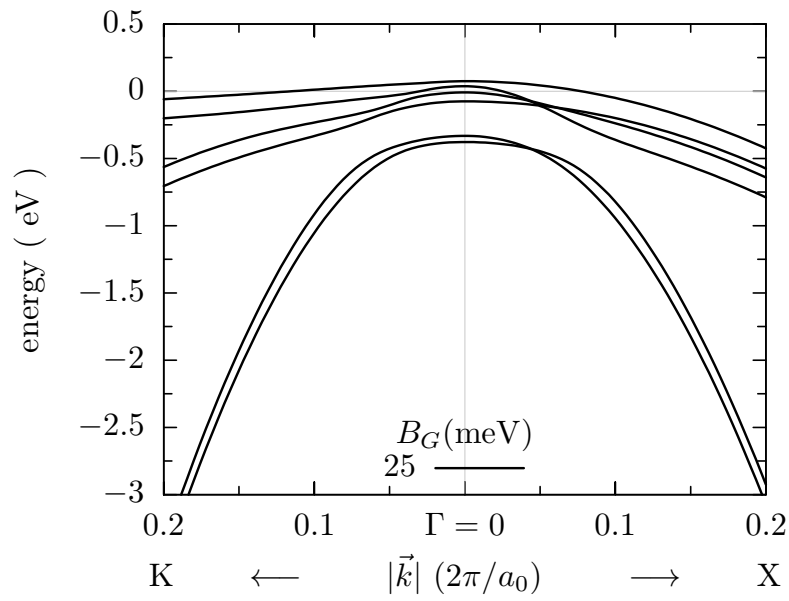
Figure 3.17: Splitting of the electronic band structure with non-zero magnetization field $B_G = 25$meV along x-axis.

of the strain, all of the possible magnetization directions are equivalent for a bulk system, especially when we consider the hole concentration or the energy of the system. However, as a consequence of strong impact of environment and its attributes on the magnetization, the material reveals many anisotropies and therefore an easy magnetization axis.
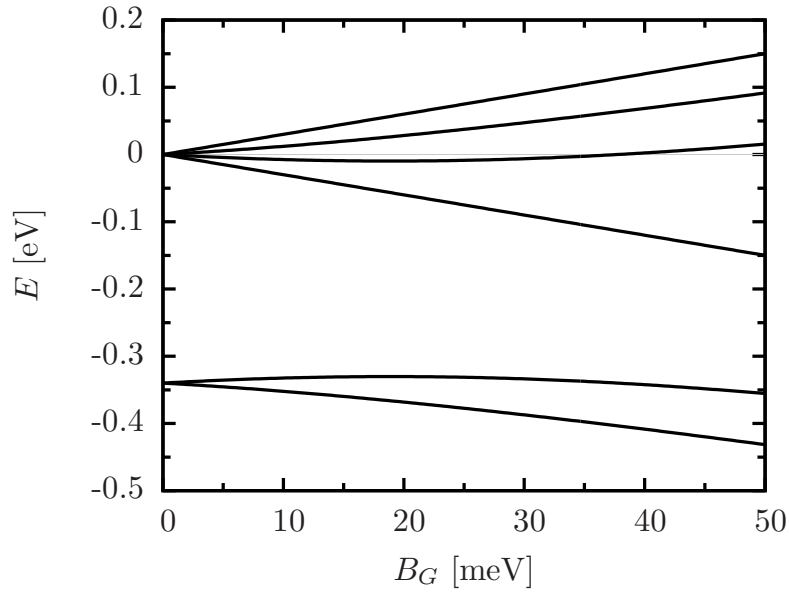
Figure 3.18: Top valence bands splitting at the Γ-point as a function of the magnetization field.

Fermi energy

The magnetization has a substantial influence on the band structure leading to a splitting of all degenerated eigenstates. Fig. 3.19 presents the isosurfaces with contributions of only three non-degenerate top valence bands, which is different to Figs. 3.3, 3.11 where at the same chemical potential two-folded bands were present. Even with contributions from three bands only, the hole concentration is increased with respect to the undoped system. In this particular case it is $p = 4.25 \times 10^{19}$cm^{-3} and $p_{xy} = 1.48 \times 10^{13}$cm^{-3} at $k_z = 0$ where the orientation of the magnetization is along x-axis.

Density of states

The hole concentration is increased together with the concentration of Mn dopants. However, the magnetization parameter B_G has to be unrealistically high, in order to observe relevant changes, but the influence of the magnetization is well visible in the density of states, see Fig. 3.20. In ternary compound of Ga$_x$Mn$_{1-x}$As with elements concentration $x \sim 0.98$ the relevant region for the total hole concentration is about $p = 10^{20}$cm^{-3}. Here means that we need a smaller chemical potential for the same hole concentration as in the system without
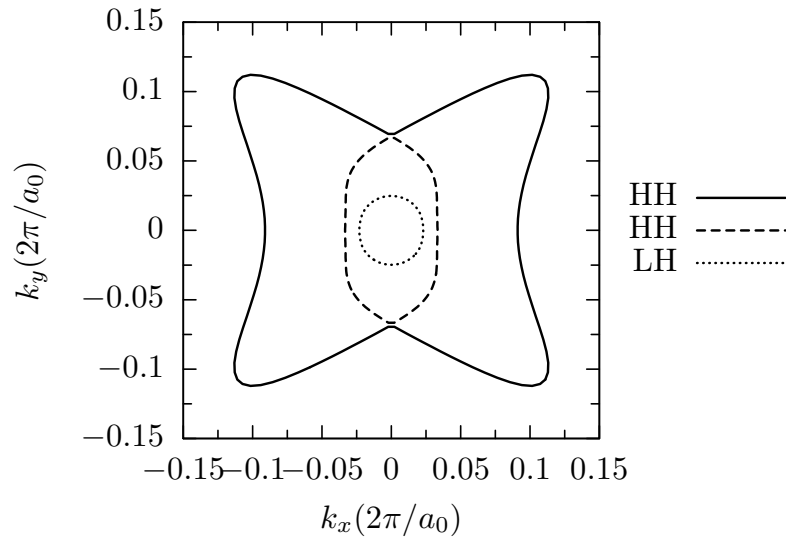
Figure 3.19: Isoenergy surface for chemical potential $\mu = -28.5$meV with spin splitting parameter $B_G = 25$meV.

magnetization. The applied cut-off at the boundary edges is pronounced as the peak in the density of states. The most attractive region for application is when the chemical potential μ is similar to the split-off Δ_{so} band gap. The main advantage of using the Kane model is now pronounced. The biggest changes are expected to be for a small hole concentration and in the close vicinity to the Γ-point, where the four-bands model is useful. Within the six-bands model, larger hole concentration can be achieved properly, what also allows to study in more details the complexity of the top valence bands.
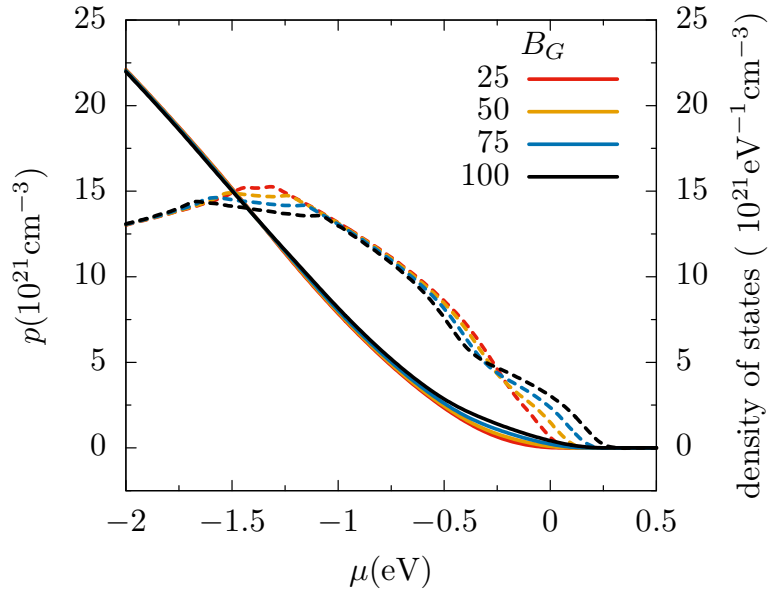
Figure 3.20: Hole concentration (solid lines) and the density of states(dashed lines) as a function of the chemical potential with a non-zero magnetization.

Variation of total energy

The strain can affect the anisotropy, and therefore, it has an influence on the easy magnetization axis. When the uni-axial strain is perpendicular to the magnetization plane, the
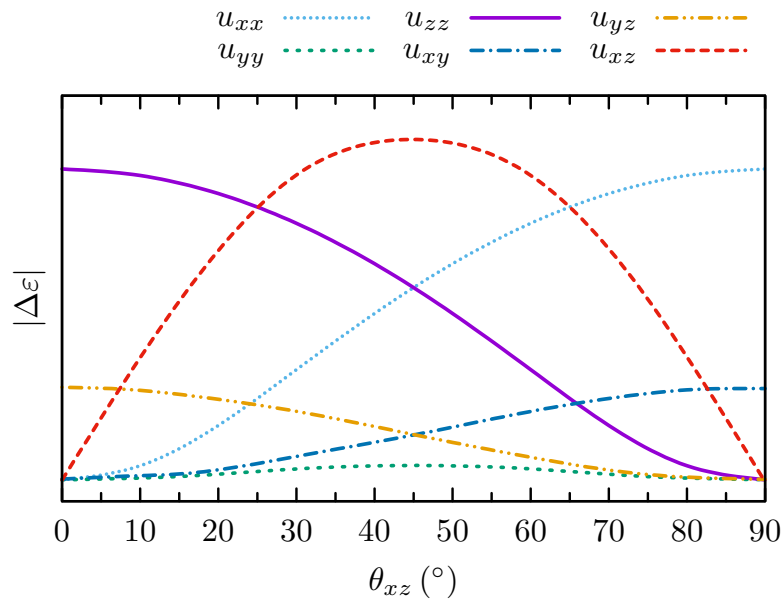
Figure 3.21: Schematic effect of the strain on the variation of the energy for different orientation of the magnetization θ_{xz}, where $\theta_{xz} = 0$ means $\vec{n}$ along z-axis.
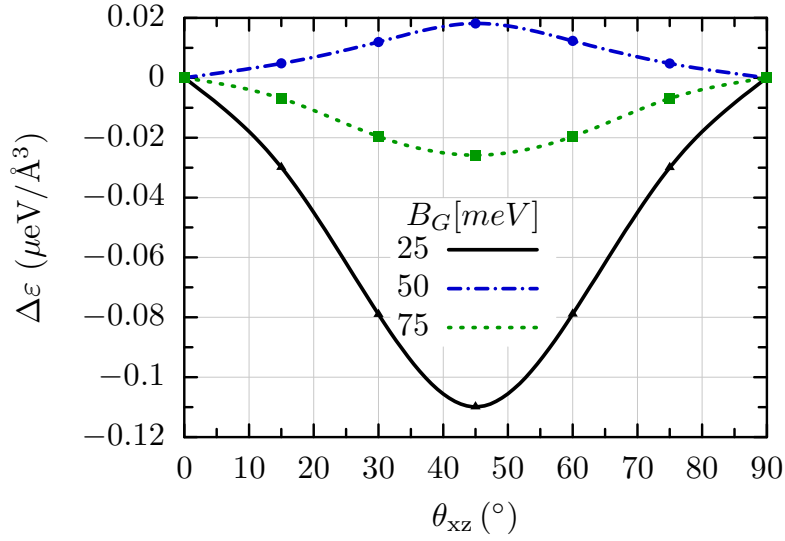
Figure 3.22: The variation of the total energy with constraint on the chemical potential for different magnetization strength B_G.
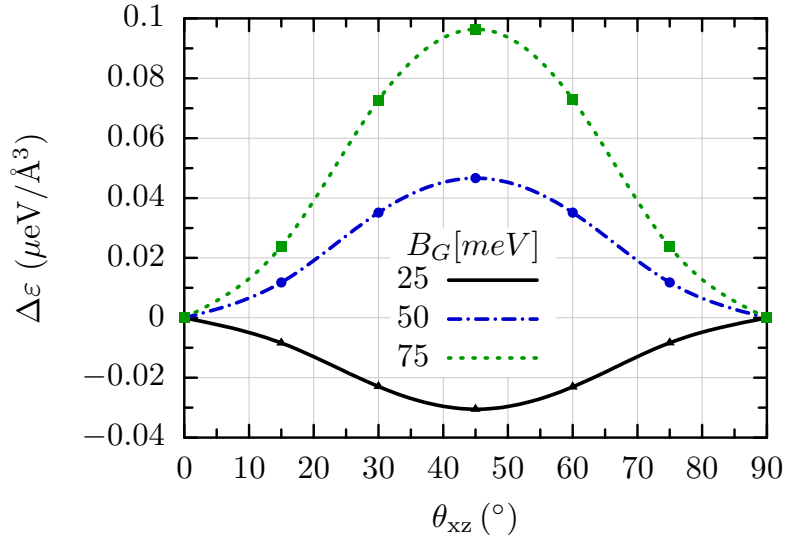
Figure 3.23: The variation of the total energy with constraint on hole concentration $p = 10^{20}$cm^{-3} for different magnetization strength B_G.

variation in the total energy weakly depends on the magnetization direction θ, see Fig. 3.21. However, when the magnetization changes from perpendicular to the parallel orientation with respect to the applied strain, the total energy may change its magnitude and sign. The condition, when the total energy decreases or increases, depends on the hole concentration and the chemical potential. Conventionally, in the bulk system, the typical constraint is made,
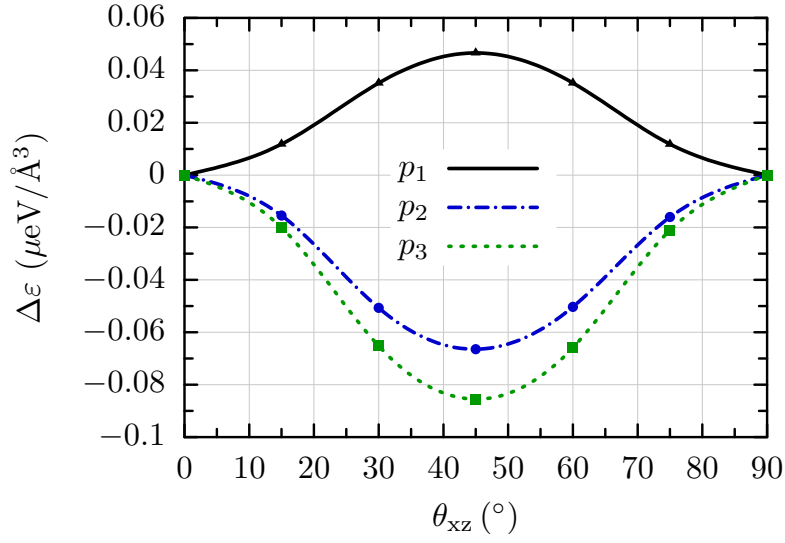
Figure 3.24: The variation of the total energy with constraint on the hole concentration $p_1 = 1.0{\times}10^{20}$ cm^{-3}, $p_2 = 2.0{\times}10^{20}$ cm^{-3}, $p_3 = 3.0{\times}10^{20}$ cm^{-3} for the value of magnetization $B_G = 50$meV with an orientation of the magnetization changing in the xz-plane.

that the hole concentration is fixed when the system is slightly perturbed. In a thin layer the better constraint seems to be fixed the chemical potential. Figs. 3.22, 3.23, 3.24 show that those two different scenarios lead to varying magnitude of the magnetic anisotropy and possibly change in the sign.

3.6   Rashba spin-orbit coupling in the z-axis quantized model

The Rashba spin-orbit coupling is important in a case of thin layers. Therefore, the z-component of the wavevector is quantized with $k_z = \pi/L$, where L is the thickness of the layer. This allows modeling the two-dimensional GaMnAs magnetic semiconductor. In the

basis (3.14) the Rashba Hamiltonian (3.5) for the top valence bands has the following form

$$
\hat{H}_R = \alpha_{so}
\begin{pmatrix}
1 & 0 & 0 & 0 & 0 & 0 \\
0 & -\frac{1}{3} & 0 & 0 & i\frac{\sqrt{2}}{3} & 0 \\
0 & 0 & -\frac{1}{3} & 0 & 0 & i\frac{\sqrt{2}}{3} \\
0 & 0 & 0 & 1 & 0 & 0 \\
0 & -i\frac{\sqrt{2}}{3} & 0 & 0 & -\frac{2}{3} & 0 \\
0 & 0 & -i\frac{\sqrt{2}}{3} & 0 & 0 & -\frac{2}{3}
\end{pmatrix},
\tag{3.38}
$$

where α_{so} is the coupling strength.   Using the spin operators Eqs.(3.35, 3.36, 3.37) allow
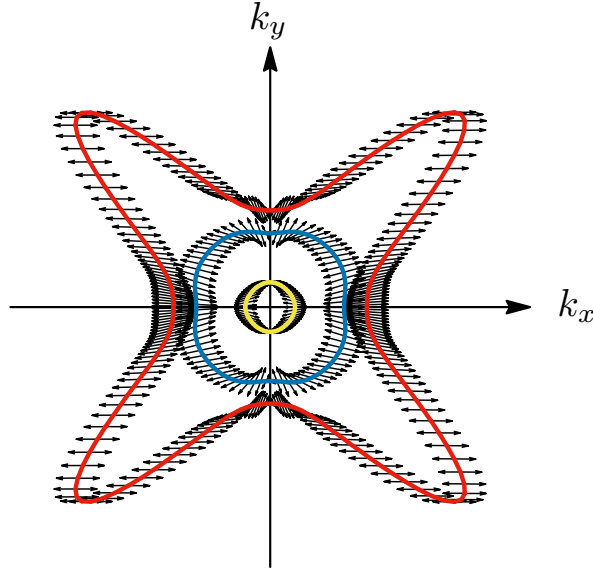
Figure 3.25: Schematic spin-polarization in the xy-plane at the isoenergy $\mu = -0.5$eV and $k_z = \pi/10$nm. The magnetization parameter is $B_G = 0.1$ meV, with its orientation $\vec{M} \parallel \hat{x}$.

to present the spin projection of holes for the given eigenstate. Let us first consider the case without the Rashba spin-orbit coupling $\alpha_{so} = 0$, see Fig. 3.25. For a better understanding, the small value of the magnetization was selected to split two-folded bands, that can be easily distinguished numerically. Also, the magnetization is small enough to omit the splitting on the schematic figure of the spin polarization in the xy-plane. Because, the net magnetization is selected along the x-axis, the majority of the spin projections has the largest x-component of the spin average. The expectation value of the spin in the vicinity of the $k_x = 0$ varies the
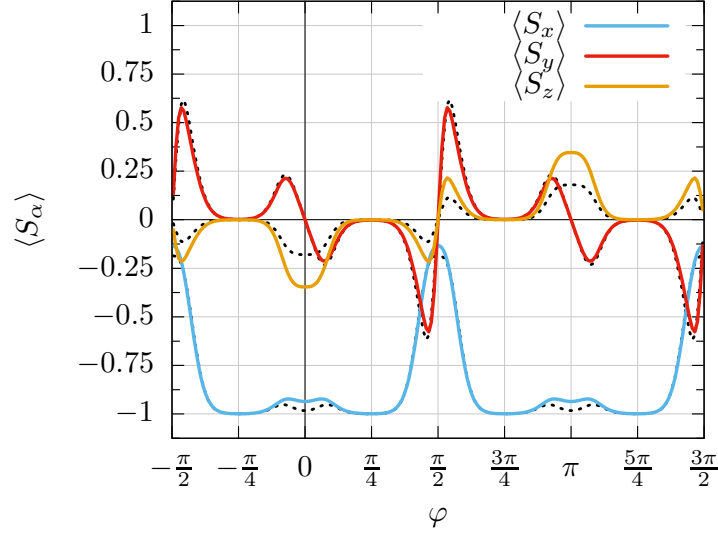
Figure 3.26: The components of the spin-polarizations in the heavy-hole band as a function of the $k_x - k_y$ plane angle φ, (see Fig. 3.25). The dotted and the solid lines are without and with the Rashba coupling $\alpha_{so} = 0.1$ eV m, respectively.

strongest. Therefore, the respective components of the spin-polarizations for each isoenergies of heavy holes band, light holes band and split-off spin-orbit band are present on Figs. 3.26, 3.27, 3.28. In fact, the figures show only three out of six nearly degenerated averaged spin polarization components, where the other have the opposite sign.

The Rashba spin-orbit coupling decreases the y-component and increases the z-component of the spin polarization that is out of the xy-plane. Also, it has the largest impact on the spin vectors of the split-off bands. The Rashba spin-orbit coupling removes the degeneracy of the four-folded heavy/light holes bands at Γ-point leaving the two-folded heavy holes and two-folded light holes bands. Finally, it shows that this component of the spin-orbit coupling can moderate the magnitude and the polarization of the effective spin. That is a true statement for all kind of spin-orbit interactions, where for their possibility of control is one of the demanded feature critical in spin-orbit based phenomena.
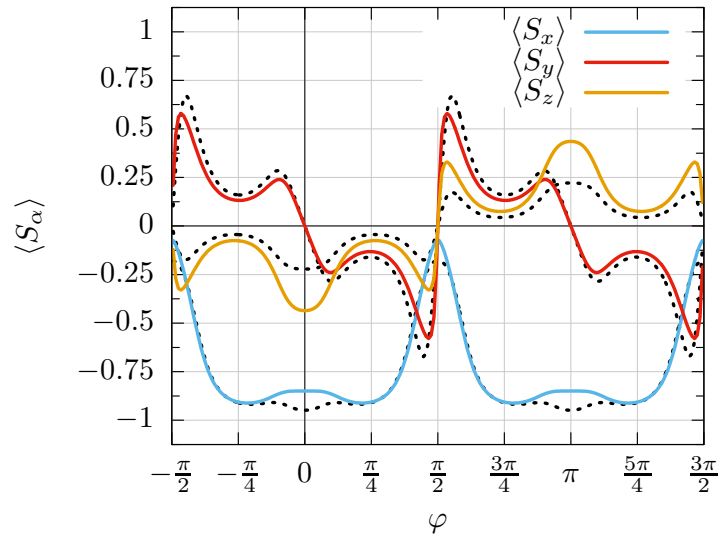
Figure 3.27: The components of the spin-polarizations in the light-hole band as a function of the angle φ. The dotted or the solid lines are results without or with the Rashba coupling $\alpha_{so} = 0.1$ eV m, respectively.
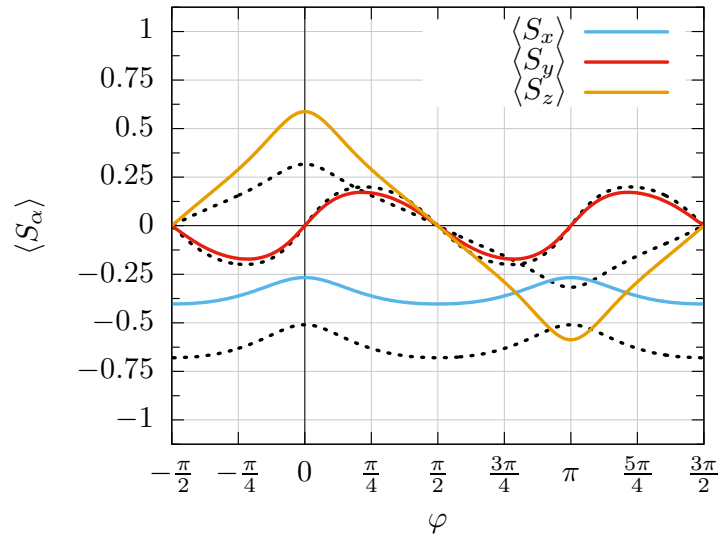
Figure 3.28: The components of the spin-polarizations in the split-off band as a function of the angle φ. The dotted or the solid lines are results without or with the Rashba coupling $\alpha_{so} = 0.1$ eV m, respectively.

Summary

The pseudopotential framework was used as the reference of the bulk GaAs band structure calculation. By using the Kane model, a detailed analysis of the properties of the electronic structure with spin-orbit coupling was performed in close vicinity to Γ-point. The hole concentration and the total energy of the system were calculated. The influence of the uniform magnetization in a system doped with Mn and the effect of strain on the band structure properties were studied. The two constraints that are appropriate in bulk and thin layers were discussed. Schematic representation of strain influence on magnetization anisotropy was shown. In the quantized model, an effect of the Rashba spin-orbit coupling on components of the spin-polarizations at constant isoenergy was presented.

Conclusions

The magnetic dynamics of the localized spins and conductance surface-states spin current were analyzed. We concluded the controlling mechanism could be done via electric fields, strain, through proximity effect of the substrate or interface with a magnetic layer instead of the conventional way of using magnetic fields.

Within a ferromagnetic and non-collinear one-dimensional spin chains, the magnetic dynamics were studied. The quantum state transfer strongly depends on the effective exchange couplings, whereas an external electric field moderates the specific time required to accomplish the communication protocol. It was shown that a strong site-dependent magnetic field disorder leads to many-body localization phase also in a spin-frustrated chain. The method for estimating a critical disorder of the phase-transition was developed.

The properties of the magnetic layer have an influence on the substrate electronic structure. The other way around, a substrate with some magnetic properties, which might depend on the concentration of impurities, has an influence on deposited layer. On the top of that, a strain affects an intrinsic magnetization anisotropy of a substrate and its electronic structure.

An influence of the Rashba spin-orbit coupling on the spin-polarization in semiconductor thin layer was investigated. It was shown that it could have the substantial influence on the magnitude and spin orientation of holes.

In future, we might look at the quantum state transfer and many-body localization in two-dimensional clusters or small molecules. We would like to address spin-conversion phenomena [74] further. We would like to have a look at the transport properties of the interfaces

with dilute magnetic semiconductors towards mechanisms of highly packing density of the information in smaller devices.

List of publications related to the dissertation

1. S. Stagraczyński, C. Jasiukiewicz, V. K. Dugaev, J. Berakdar, *Strain designed magnetic properties of III-V magnetic semiconductors*, Acta Phys. Polonica A **128**, 219 (2015), http://doi.org/10.12693/APhysPolA.128.219

2. C. Jasiukiewicz, S. Stagraczyński, D. Lehmann, V. K. Dugaev, J. Berakdar, *Influence of acoustic phonos on the magnetic anisotropy in GaMnAs magnetic semiconductors*, Acta Phys. Polonica A **128**, 179 (2015), http://doi.org/10.12693/APhysPolA.128.179

3. S. Stagraczyński, C. Jasiukiewicz, V. K. Dugaev, J. Berakdar, *Magnetic anisotropy control in $Ga_{1-x}Mn_xAs$ magnetic semiconductors*, J. Magn. Magn. Mater. **411**, 79 (2016), http://doi.org/10.1016/j.jmmm.2016.03.052

4. S. Stagraczyński, L. Chotorlishvili, V. K. Dugaev, C.-L. Jia, A. Ernst, A. Komnik, J. Berakdar, *Topological insulator in a helicodial magnetization field*, Phys. Rev. B **94**, 174436 (2016), http://doi.org/10.1103/PhysRevB.94.174436

5. L. Chotorlishvili, M. Azimi, S. Stagraczyński, Z. Toklikishvili, M. Schüler, J. Berakdar, *Superadiabatic quantum heat engine with a multiferroic working medium*, Phys. Rev. E **94**, 032116 (2016), http://doi.org/10.1103/PhysRevE.94.032116

6. Z. Toklikishvili, L. Chotorlishvili, S. K. Mishra, S. Stagraczyński, M. Schüler, A. R. P. Rau, J. Berakdar, *Entanglement dynamics of two nitrogen vacancy centers coupled by a*

81

nanomechanical resonator, J. Phys. B: At. Mol. Opt. Phys. **50**, 055007 (2017), http://doi.org/10.1088/1361-6455/aa5a69

7. L. Chotorlishvili, M. Azimi, S. Stagraczyński, J. Berakdar, *Quantum heat engines with multiferroic working substance*, arXiv:1703.00855, Lecture Notes of the 12th International School on Theoretical Physics, submitted to World Scientific (2017)

8. S. Stagraczyński, L. Chotorlishvili, M. Schüler, M. Mierzejewski, M. Heyl, J. Berakdar, *Many-body localization phase in a spin-driven chiral multiferroic chain*, submitted to Phys. Rev. Lett. (2017)

9. S. Stagraczyński, J. Berakdar, V. K. Dugaev, *Effect of Rashba spin-orbit coupling on the spin polarization of holes in two- dimensional GaMnAs magnetic semiconductors*, to be published in Acta Phys. Polonica A (2017)

Bibliography

[1] *Nobel lectures, physics, 2006-2010*, World Scientific (2014), ISBN 978-981-4612-67-8.

[2] D. Pesin, A. H. MacDonald, *Spintronics and pseudospintronics in graphene and topological insulators*, Nat Mater **11**, 409 (2012), http://doi.org/10.1038/nmat3305

[3] I. Žutić, J Fabian, and S. D. Sarma, *Spintronics: Fundamentals and applications*, Rev. Mod. Phys. **76**, 323 (2004), http://doi.org/10.1103/RevModPhys.76.323

[4] J. Schliemann, *Colloquium: Persistent spin textures in semiconductor nanostructures*, Rev. Mod. Phys. **89**, 011001 (2017), http://doi.org/10.1103/RevModPhys.89.011001

[5] A. Brataas, A. D. Kent, H. Ohno, *Current-induced torques in magnetic materials*, Nat Mater **11**, 372 (2012), http://doi.org/10.1038/nmat3311

[6] S. Bose, *Quantum Communication through an Unmodulated Spin Chain*, Phys. Rev. B, **91**, 20 (2003), http://doi.org/10.1103/PhysRevLett.91.207901

[7] M. Z. Hasan, C. L. Kane, ***Colloquium:*** *Topological insulators*, Rev. Mod. Phys. **82**, 3045 (2010), http://doi.org/10.1103/RevModPhys.82.3045

[8] T. Dietl, H. Ohno, *Dilute ferromagnetic semiconductors: Physics and spintronic structures*, Rev. Mod. Phys., **86**, 187 (2014), http://doi.org/10.1103/RevModPhys.86.187

[9] A. Manchon, H. C. Koo, J. Nitta, S. M. Frolov, R. A. Duine, *New perspectives for Rashba spin–orbit coupling*, Nature Materials **14**, 871 (2015), http://doi.org/10.1038/nmat4360

[10] H. Katsura, N. Nagaosa, A. V. Balatsky, *Spin Current and Magnetoelectric Effect in Noncollinear Magnets*, Phys. Rev. Lett. **95**, 057205 (2005), http://doi.org/10.1103/PhysRevLett.95.057205

[11] P. Bruno, V. K. Dugaev, *Equilibrium spin currents and the magnetoelectric effect in magnetic nanostructures*, Phys. Rev. B **72**, 241302(R) (2005), http://doi.org/10.1103/PhysRevB.72.241302

[12] M. Azimi, L. Chotorlishvili, S. K. Mishra, S. Greschner, T. Vekua, J. Berakdar, *Helical multiferroics for electric field controlled quantum information processing*, Phys. Rev. B, **89** 024424 (2014), http://doi.org/10.1103/PhysRevB.89.024424

[13] R. Nandkishore, D. A. Huse, *Many-Body Localization and Thermalization in Quantum Statistical Mechanics*, Annu. Rev. Condens. Matter Phys. **6**, 15 (2015), http://doi.org/10.1146/annurev-conmatphys-031214-014726

[14] D. J. Luitz, N. Laflorience, F. Alet, *Many-body localization edge in the random-field Heisenberg chain*, Phys. Rev. B, **91**, 081103(R) (2015), http://doi.org/10.1103/PhysRevB.91.081103

[15] X.-L. Qi, S.-C. Zhang, *Topological insulators and superconductors*, Rev. Mod. Phys., **83**, 1057 (2011), http://doi.org/10.1103/RevModPhys.83.1057

[16] N. Nagaosa, J. Sinova, S. Onoda, A. H. MacDonald, N. P. Ong, *Anomalous Hall effect*, Rev. Mod. Phys. **82**, 1539 (2010), http://doi.org/10.1103/RevModPhys.82.1539

[17] A. Crepieux, P. Bruno, *Theory of the anomalous Hall effect from the Kubo formula and the Dirac equation*, Phys. Rev. B **64**, 014416 (2001), http://doi.org/10.1103/PhysRevB.64.014416

[18] T. Jungwirth, J. Sinova, J. Mašek, J. Kučera, A. H. MacDonald, *Theory of ferromagnetic (III,Mn)V semiconductors*, Rev. Mod. Phys. **78**, 809 (2006), http://doi.org/10.1103/RevModPhys.78.809

[19] T. Jungwirth, J. Wunderlich, V. Novák, K. Olejník, B. L. Gallagher, R. P. Campion, K. W. Edmonds, and A. W. Rushforth, A. J. Ferguson, P. Němec *Spin-dependent phenomena and device concepts explored in (Ga,Mn)As*, Rev. Mod. Phys. **86**, 855 (2014), http://doi.org/10.1103/RevModPhys.86.855

[20] J. M. D. Coey, *Magnetism and magnetic materials*, Cambridge (2010), ISBN 978-0-521-81614-4

[21] G. D. Mahan, *Many-particle physics*, Plenum Press (1990), ISBN 978-0-306-43423-5

[22] I. Dzyaloshinsky, *A thermodynamic theory of "weak" ferromagnetism of antiferromagnetics*, J. Phys. Chem. Solids **4**, 241 (1958), http://doi.org/10.1016/0022-3697(58)90076-3

[23] T. Moriya, *Anisotropic Superexchange Interaction and Weak Ferromagnetism*, Phys. Rev. **120**, 1 (1960)

[24] M. J. Donahue, D. G. Porter, *OOMMF User's Guide, Version 1.0*, Interagency Report NIS-TIR, 6376 (1999), http://math.nist.gov/oommf/

[25] A. Vansteenkiste, J. Leliaert, M. Dvornik, M. Helsen, F. Garcia-Sanchez, B. V. Waeyenberge, *The design and verification of mumax3*, AIP Advances **4**, 107133 (2014), http://doi.org/10.1063/1.4899186

[26] V. F. Nesterenko, *Dynamics of Heterogeneous Materials*, Springer-Verlag, New York, (2001).

[27] S. Sen, J. Hong, J. Bang, E. Avalos, R. Doney, *Solitary waves in the granular chain*, Phys. Rep. **462**, 21 (2008), http://doi.org/10.1016/j.physrep.2007.10.007

[28] S. Hutzler, G. Delaney, D. Weaire, F. MacLeod, *Rocking Netwon's cradle*, Am. J. Phys. **72**, 12 (2004), http://doi.org/10.1119/1.1783898

[29] F. A. L. Mauguière, P. Collins, G. S. Ezra, S. Wiggins. *Bond breaking in a Morse chain under tension: Fragmentation patterns, higher index saddles, and bond healing*. J. Chem. Phys. **138**, 134118 (2013), http://doi.org/10.1063/1.4798641

[30] J. N. Stember, G. S. Ezra, *Framgnetation kinetics of a Morse oscillator chain under tension*, J. Chem. Phys. **337**, 11 (2007), http://doi.org/10.1016/j.chemphys.2007.06.019

[31] D. Corradinig, F.-X. Coudert, R. Vuilleumier, *Carbon dioxide transport in molten calcium carbonate occurs through an oxo-Grotthuss mechanism via a pyrocarbonate anion*, Nature Chemistry **8**, 454-460 (2016), http://doi.org/10.1038/nchem.2450

[32] Nakamura, et. al. *"Newton's cradle" proton relay with amide–imidic acid tautomerization in inverting cellulase visualized by neutron crystallography*. Sci. Adv. 1500263 (2015).

[33] J. Simoni, M. Stamenova, S. Sanvito, *Ultrafast demagnetizing fields from first principles*, Phys. Rev. B **95**, 024412 (2017), http://doi.org/10.1103/PhysRevB.95.024412

[34] Y. Y. Atas, E. Bogomolny, O. Giraud, G. Roux, *Distribution of the Ratio of Consecutive Level Spacings in Random Matrix Ensembles*, Phys. Rev. Lett. **110**, 084101 (2013), http://doi.org/10.1103/PhysRevLett.110.084101

[35] I. Affleck, M. Oshikawa, *Field-induced gap in Cu benzoate and other $S = \frac{1}{2}$ antiferromagnetic chains*, Phys. Rev. B **60**, 1038 (1999), http://doi.org/10.1103/PhysRevB.60.1038

[36] S. Murakami, N. Nagaosa, S-C. Zhang, *Spin-Hall insulator*, Phys. Rev. Lett. **93**, 156804 (2007), http://doi.org/10.1103/PhysRevLett.93.156804

[37] R. Dias, I. F. Silvera, *Observation of the Wigner-Huntington transition to metallic hydrogen*, Science **355**, 715 (2017), http://doi.org/10.1126/science.aal1579

[38] A. P. Sutton, *Electronic structure of materials*, Oxford Science Publications (1993), ISBN 0-19-851755-6

[39] P. A. M. Dirac, *The Quantum Theory of the Electron*, Proc. R. Soc. Lond. A, **117**, 778 (1928), http://doi.org/10.1098/rspa.1928.0023

[40] R. Žitko, *Quantum impurity on the surface of a topological insulator*, Phys. Rev. B **81**, 241414(R) (2010), http://doi.org/10.1103/PhysRevB.81.241414

[41] Q. Liu, C.-X. Liu, C. Xu, X.-L. Qi, S.-C.Zhang, *Magnetic Impurities on the Surface of Topological Insulator*, Phys. Rev. Lett. **102**, 156603 (2009), http://doi.org/10.1103/PhysRevLett.102.156603

[42] C. Jia, J. Berakdar, *Dynamical magnetoelectric effects induced by the Dzyaloshinskii-Moriya interaction in multiferroics* Eur. Phys. Lett. **85**, 57004 (2009), http://doi.org/10.1209/0295-5075/85/57004

[43] A. Yu. Silov, P. A. Blajnov, J. H. Wolter, R. Hey, K. H. Ploog, N. S. Averkiev, *Current-induced spin polarization at a single heterojunction*, Appl. Phys. Lett. **85**, 5929 (2004), http://doi.org/10.1063/1.1833565

[44] S. Takahashi, E. Saitoh, S. Maekawa, *Spin current through a normal-metal/insulating-ferromagnet junction*, Journal of Physics: Conference Series **200**, 062030 (2010) http://doi.org/10.1088/1742-6596/200/6/062030

[45] R. Ramos, T. Kikkawa, M. H. Aguirre, I. Lucas, A. Anadón, T. Oyake, K. Uchida, H. Adachi, J. Shiomi, P. A. Algarabel, L. Morellón, S. Maekawa, E. Saitoh, M. R. Ibarra, *Observation of huge thermal spin currents in magnetic multilayers*, Phys. Rev. B **92**, 220407 (2015), http://doi.org/10.1103/PhysRevB.92.220407

[46] T. Jungwirth, *Antiferromagnetic spintronics*, 79th Annual Metting of the DPG and DPG-Frühjahrstagung of the Condensed Matter Section (2015),

[47] R. Winkler, *Spin-Orbit Coupling Effects in Two-Dimensional Electron and Hole Systems*, ISBN 978-3-540-01187-3 (2003).

[48] M. W. Wu, J. H. Jiang, M. Q. Weng, *Spin dynamics in semiconductors*, Phys. Rep. **493**, (2010), http://doi.org/10.1016/j.physrep.2010.04.002

[49] G. Dresselhaus, *Spin-Orbit Coupling Effects in Zinc Blende Structures*, Phys. Rev. **100**, 580 (1955), http://doi.org/10.1103/PhysRev.100.580

[50] Yu. A. Bychkov, E. I. Rashba, *Properties of a 2D electron gas with lifted spectral degeneracy*, JETP Lett. **39**, 2 (1984)

[51] E. I. Rashba, *Graphene with structure-induced spin-orbit coupling: Spin-polarized states, spin zero modes, and quantum Hall effect*, Phys. Rev. B **79**, 161409(R) (2009), http://doi.org/10.1103/PhysRevB.79.161409

[52] M. M. Glazov, E. Ya. Sherman, V. K. Dugaev, *Two-dimensional electron gas with spin-orbit coupling disorder*, Physica E, **42**, 2157 (2010), http://doi.org/10.1016/j.physe.2010.04.021

[53] J. C. Slater, G. F. Koster, *Simplified LCAO Method for the Periodic Potential Problem*, Phys. Rev. **94**, 1498 (1954), http://doi.org/10.1103/PhysRev.94.1498

[54] J. C. Phillips, *Energy-band interpolation scheme based od a pseudopotential*, Phys. Rev. **112**, 3 (1958)

[55] J. C. Phillips, L. Kleinman, *New method for calculation wave functions in crystals and molecules*, Phys. Rev. **116**, 2 (1959)

[56] L. Kleinman, J. C. Phillips, *Crystal potential and energy bands of semiconductors. III. self-consistent calculations for silicon*, Phys. Rev. **118**, 2 (1959)

[57] A. J. Danner, *An introduction to the empirical pseudopotential method*, https://www.ece.nus.edu.sg/stfpage/eleadj/pseudopotential.htm

[58] M. L. Cohen, T. K. Bergstresser, *Band Structures and Pseudopotential Form Factors for Fourteen Semiconductors of the Diamond and Zinc-blende Structures*, Phys. Rev. **141**, 789 (1966). http://doi.org/10.1103/PhysRev.141.789

[59] T. Dietl, H. Ohno, F. Matsukura, *Hole-mediated ferromagnetism in tetrahedrally coordinated semiconductors*, Phys. Rev. B, **63**, 195205 (2001), http://doi.org/10.1103/PhysRevB.63.195205

[60] G. L. Bir, G. E. Pikus, *Symmetry and Strain-induced Effects in Semiconductors*, Wiley (1974)

[61] L. C. L. Y. Voon, M. Willatzen, *The k·p method: electronic properties of semiconductors*, Springer (2009), ISBN 978-3-540-92871-3, http://doi.org/10.1007/978-3-540-928720-0

[62] P. Y. Yu, M. Cardona, *Fundamentals of semiconductors. Physics and materials properties*, Springer (2010), ISBN 978-3-642-00710-1

[63] J. M. Luttinger, W. Kohn, *Motion of electrons and holes in perturbed periodic fields*, Phys. Rev. **97**, 4 (1955)

[64] N. E. Christensen, S. Satpathy, Z. Pawlowska, *Bonding and ionicity in semiconductors*, Phys. Rev. B, **36**, 2 (1987)

[65] http://www.ioffe.ru/SVA/NSM/Semicond/GaAs

[66] A. R. Edmonds, *Angular momentum in quantum mechanics*, Princeton Univ. Press (1996), ISBN 9780691025896

[67] R. Winkler, *A note on analytic quadratic Brillouin zone integration*, J. Phys.: Condens. Matter **5**, 2321 (1993)

[68] J. H. Hannay, J. F. Nye, *Fibonacci numerical integration on a sphere*, J. Phys. A: Math. Gen. **37**, 11591 (2004), http://doi.org/10.1088/0305-4470/37/48/005 .

[69] S. L. Chuang, C. S. Chang, *k·p method for strained wurtzite semiconductors*, Phys. Rev. B **54**, 4 (1996), http://doi.org/10.1103/PhysRevB.54.2491

[70] S. L. Chuang, S. H. Park, J. Minch, T. Keating, *Strained zinc-blende and wurtzite quantum-well lasers: theory and comparsion with experiment*, in V. Stefan, N. G. Basov, *Semiconductor science and technology*, **1**, 35, ISBN 1-889545-11-2

[71] A. Werpachowska, T. Dietl, *Effect of inversion asymmetry on the intrinsic anomalous Hall effect in ferromagnetic (Ga, Mn)As*, Phys. Rev. B, **81**, 155205 (2010), http://doi.org/10.1103/PhysRevB.81.155205

[72] H. Ohldag, V. Solinus, F. U. Hillebrecht, J. B. Goedkoop, M. Finazzi, F. Matsukura, H. Ohno, *Magnetic moment of Mn in the ferromagnetic semiconductor (Ga$_{0.98}$Mn$_{0.02}$As)*, Appl. Phys. Lett. **76**, 2928 (2000), http://doi.org/10.1063/1.126519

[73] W. Stefanowicz, C. Śliwa, P. Aleshkevych, T. Dietl, M. Döppe, U. Wurstbauer, W. Wegscheider, D. Weiss, M. Sawicki, *Magnetic anisotropy of epitaxial (Ga,Mn)As on (113)A GaAs*, Phys. Rev. B **81**, 155203 (2010), http://doi.org/10.1103/PhysRevB.81.155203

[74] S. Karube, K. Kondou, Y. Otani, *Experimental observation of spin-to-charge current conversion at non-magnetic metal/Bi$_2$O$_3$ interfaces*, Appl. Phys. Exp. **9**, 033001 (2016), http://doi.org/10.7567/APEX.9.033001

[75] R. Cools, A. Haegemans, ACM Transactions on Mathematical Software, Vol. 29(3) pp. 287-296. 2003. http://doi.org/10.1145/838250.838253 .

[76] R. Cools, *An encyclopedia of cubature formulas*, J. Complex. **19**, 3 (2003), http://doi.org/10.1016/S0885-064X(03)00011-6 ,

[77] R. Cools, *Monomial cubature rules since "Stroud": a compilation — part 2*, J. Comput. Appl. Math. **112**, 21 (1999), http://doi.org/10.1016/S0377-0427(99)00229-0

[78] R. Cools, P. Rabinowitz, *Monomial cubature rules since "Stroud": a compilation*, J. Comput. Appl. Math. **48**, 3 (1993), http://doi.org/10.1016/0377-0427(93)90027-9

[79] G. Strang, G. Fix, *An analysis of the finite element method*, Wellesley-Cambridge (2008), ISBN 978-0-9802327-0-7

[80] The CGAL Project, *CGAL User and Reference Manual*, CGAL Editorial Board, 4.10 (2017), http://doc.cgal.org/4.10/Manual/packages.html

[81] http://viennafem.sourceforge.net/doc/quadrature_2triangle_8hpp_source.html

[82] https://people.sc.fsu.edu/~jburkardt/datasets/quadrature_rules_tri/quadrature_rules_tri.html

[83] D. M. Day, M. A. Taylor, *A new 11 point degree 6 cubature formula for the triangle*, Proc. Appl. Math. Mech. **7** 1022501 (2007), http://doi.org/10.1002/pamm.200700477

An adaptive mesh generation

for the two-dimensional integration scheme

Most of the calculations are done with the extensive use of **GNU Scientific Library**(GSL) for interpolation, optimized version of **Basic Linear Algebra Subprograms**(BLAS) and **Linear Algebra Package**(LAPACK). In the following chapter, one variation of the used integration algorithm will be introduced together with a possible $C++$ implementation. The set of requirements were helpful while choosing the relevant method

- splitting the integration domain to smaller pieces (simplices) forming an integration mesh

- integration over the created mesh of simplices

- easy extendibility

- reduced number of points evaluation (adaptive)

- processing of the vector integrands

- evaluation of an error estimation

In parallel computing, working with meshes is simple. The tasks can be easily distributed between different computing slaves either with OpenMPI or CUDA programming manners. However, working with a uniform mesh can be computationally demanding. In the two-
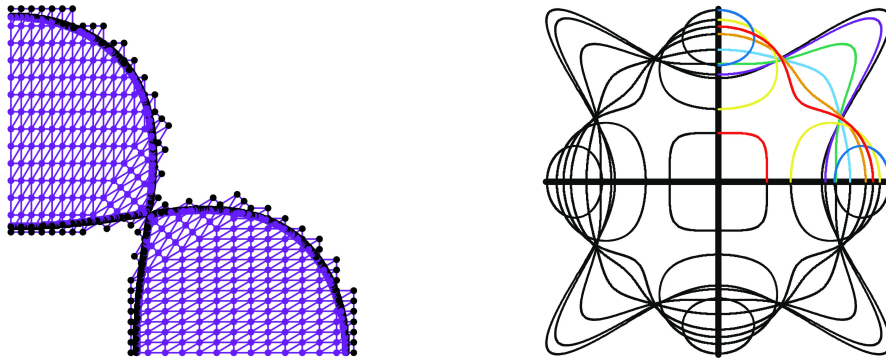
Figure A.1: The edge detection in k_z slices of the GaAs isoenergies.
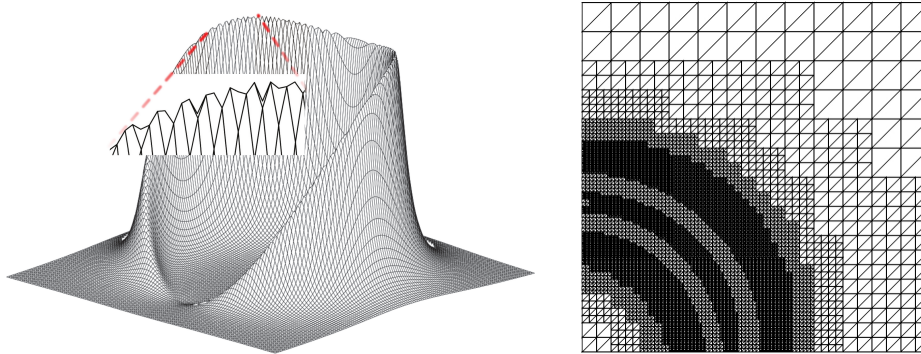
Figure A.2: The left figure presents the oscillations at the maximum edge with an uniform mesh and on the right figure an adaptive mesh.

dimensional integration scheme the simplices that are used in a mesh creation are mainly rectangles and triangles. In a few situations it might be better to keep the rectangles in the memory and split them to the triangles just before the integration. However, this technical detail is not of our concern. The first step is to generate a uniform or non-uniform(random) mesh. If the integrand function is smooth, it is possibly enough and the integration scheme can be performed making the mesh more dense. The comparison of the results allows to check the convergence. However, for non-continuous, sharp peaks and step functions the ideal case would be to split integration domain based on points of discontinuities(of the function or their derivatives). In the studied case, there are multiple edges that can cross or nearly cross each other Fig. A.1. On each of the simplices, the classification procedure is performed in order to group the pieces of mesh either to the edge or to the inside/outside classes. The finalizing condition for splitting procedure can be formulated differently, depending on the needs. In chapter 3 for computation of the hole concentrations and total

energies, the splitting was stopped if the summed area of edge simplicities was smaller than 1% of the summed area of filled simplicities.

As the discussed method will be three-points Gauss integration scheme for the triangle, however, more points rules will work exactly in the same way. Note that any triangle can be transformed to the unit triangle. Then the integration scheme(cubature) is reduced to the sum of the values of the function at specific given points with their weights

$$\int\limits_{\triangle} d\vec{k}\vec{f}(\vec{k}) = \sum_{i=1}^{n} w_i \vec{f_i}, \tag{A.1}$$

where n is the number of weights and depending on the set of points and weights the result is exact up to the different polynomial order. The function is evaluated for the set of points(abscissas) given in the tables A that contain few symmetric and the asymmetric rules. In this context, by the symmetric rule it is meant that the result does not depend on the clockwise or anti-clockwise order of triangle vertices. An extensive reference list of cubature rules can be found here [75, 76, 77, 78, 79].

The simplified listings of the C++ sources codes are shown here. It is convenient to split task to the two structures(functors) that are shown. The first structure *Integrand_Functor_Tri_f* is independent on the used finite element method rules. It computes the Jacobian of any triangle to the unit triangle and works as the mapping of the function with abscissas $\tilde{f}(\xi, \eta) \to f(x, y)$ in transformed triangle.

```cpp
struct Integrand_Functor_Tri_f : public Abstract{
    double J;
    Triangle t;
    Integrand_Functor_Tri_f(Triangle c) : t(c){
        J = fabs(
            (t.p[1].x-t.p[0].x)*(t.p[2].y-t.p[0].y)
           -(t.p[2].x-t.p[0].x)*(t.p[1].y-t.p[0].y)
        );
    }
    vector operator()(double xi, double eta){
        return (*f_ptr)(
```

```
              t.p[0].x + (t.p[1].x−t.p[0].x)∗xi + (t.p[2].x−t.p[0].x)∗eta,

              t.p[0].y + (t.p[1].y−t.p[0].y)∗xi + (t.p[2].y−t.p[0].y)∗eta
          );
      };
};
```

The second structure uses template for the specialization with a selected rule that as an argument accepts the *Triangle* structure (three points) and as an output returns an evaluated integration over the triangle.

```
template<double w[][3], int n>
struct FEM_triCubaf : public Abstract{
    int i;
    vector sum;
    vector operator()(Integrand_Functor_Tri_f tri){
        sum.zeros();
        for(i=0; i<n; i++){
            sum += tri(w[i][0], w[i][1])∗w[i][2];
        }
        return 0.5∗tri.J∗sum;
    }
};
```

It is recommendable to use this structure with low order rules at first while the adaptive splitting and classification of the simplices is performed. In two-dimensional integration with many sharp edges the following steps can be considered

1. Reduce the integration domain with respect to the symmetry and possible cutoffs. The more densely accepted an uniform mesh of simplices from first splittings, the faster convergence and more accurate results for less integrand function evaluation.

2. Further conditional blurred edges splitting. The classification and splitting can be performed for specified simplices e. g. in vicinity of edges. This step is optional, but

when working with the Heaviside function it can guarantee stability of the algorithm. Otherwise, if the initial uniform mesh from the step 1) is not dense enough, the edge simplices can possibly be skipped.

3. Strict edges splitting. In this step the extra one or two splittings can be performed only for the simplices that belong to the edge.

4. Finial integration. In this step, higher order cubature rules are used and the final classification is performed, and the procedure is finished if the stop condition is fulfilled, otherwise go back to point 2) or 3) for the additional edge splitting. The simplices that are not grouped with edges can be integrated with lower cubature order.

Fig. A.2 presents the uniform mesh and projection of the part of the adaptive mesh. The edge was defined as the local maxima of the integrand and when the integration function approachs the global minimum. The quality of the mesh can be improved by the Delaunay triangulation and especially by its constrained variation [80] with respect to the first Brillouin Zone.

Table A.1: The three-points Gauss rule(symmetric) exact up to first order.

ξ	η	weight
0	1/2	1/3
1/2	0	1/3
1/2	1/2	1/3

Table A.2: The seven-points rule [81, 82] exact up to fifth-order.

ξ	η	weight
0.79742698535308732240	0.10128650732345633880	0.12593918054482715260
0.10128650732345633880	0.79742698535308732240	0.12593918054482715260
0.10128650732345633880	0.10128650732345633880	0.12593918054482715260
0.059715871789769820459	0.47014206410511508977	0.13239415278850618074
0.47014206410511508977	0.059715871789769820459	0.13239415278850618074
0.47014206410511508977	0.47014206410511508977	0.13239415278850618074
0.33333333333333333333	0.33333333333333333333	0.22500000000000000000

Table A.3: The eleven-points rule [83] (asymmetric) exact up to sixth-order. Note, those weights requires an additional factor of 2 with respect to the other listed weights.

ξ	η	weight
0.05725498667747686	0.89549814678987949	0.01903403592647780
0.89536264002457910	0.06182822125032195	0.01918967765387641
0.68447574845651404	0.02334373849768273	0.02310022837228092
0.06874625591502953	0.06003027574726300	0.02673379472209950
0.61567620557583957	0.33346180834137717	0.04187791348287284
0.62794614119778946	0.15918918599215148	0.05082241651275853
0.06290913834186357	0.65529509370545247	0.05093076223068348
0.06837821192050991	0.30911768542826723	0.05571091583000085
0.28752945837439225	0.63642650917962018	0.05600472513147303
0.32878355641313461	0.07702400564246342	0.06239378571877916
0.31229040501364480	0.35234478644589950	0.09420174441869741

Acknowledgments

I would like to express my gratitude to my supervisor Prof. Jamal Berakdar for allowing my Ph.D. studies in his group and for teaching me to look broadly at the physics. Thank you for the opportunities to attend conferences, travel abroad for scientific discussions and also thank you for the possibility to use the excellent computational facilities. I would also like to express my gratitude to Prof. Vitalii Dugaev for supervising and countless discussions on research. I am sincerely grateful for the time my supervisors have devoted me and for all suggestions that helped me better understand my field of research.

I want to say many thanks to those with whom I could interact during my stay in Halle (Saale). Mainly, all current and former members of our research group. Especially to M. Schüler with whom I could talk about everything, not always related to the scientific topics. Also, special thanks to L. Chotorlishvili with whom I had many fascinating discussions. I would like to thanks, Y. Pavlyukh, A. Sukhov, S. R. Etesami, S. Mishra, M. Azimi, J. Wätzel, C. Granados, X.-G. Wang, A. Schäffer, D. Schulze, M. Brucker, B. Niedzielski, M. Kraus, for all discussions and seminars.

Also, I would like to thank our group visitors, Prof. M. Mierzejewski who sparked my fascination with many-body localization phenomena, A. Dyrdał, M. Heyl, M. Inglot and Prof. J. Fabian for their lectures and discussions on different scientific background. I would like to thank all the guests that came to the University. Especially, Prof. A. Fert, Prof. S. Parkin, Prof. Y. Otani whose colloquia were significantly close to my heart.

Last but not least, I want to thank my family for the support that they gave me.

Erklärung an Eides statt

Hiermit erkläre ich, dass ich meine Arbeit selbständig und ohne fremde Hilfe verfasst, andere als die von mir angegebenen Quellen und Hilfsmittel nicht benutzt und die den benutzten Werken wörtlich oder inhaltlich entnommenen Stellen als solche kenntlich gemacht habe.

Halle (Saale),

_____

Stefan Stagraczyński

Curriculum Vitae

Personal data

Names and surname:	Stefan Piotr Stagraczyński
Date of birth:	02.08.1987
Place of birth:	Kolbuszowa
Address:	Pekinger Str. 7, 06130 Halle (Saale)
Nationality:	Polish
Marital status:	married, one child
E-mail:	ststag@gmail.com

Education

2006-2010 - Rzeszów University of Technology, Poland,
in the field of: Engineering Physics,
with major in: Computer Physics in Engineering and Medicine.
Engineer thesis „Elastic parameters of cubic crystals",
with note „plus good".

2010-2012 - Rzeszów University of Technology, Poland
in the field of: Engineering Physics
with major in: Physics in Medicine and Engineering.
Master thesis „Modeling of electron structures for semiconductors systems',
with note „very good".

2013-   - Martin-Luther-Universität Halle-Wittenberg, Germany

Halle (Saale),

_____
Stefan Stagraczyński